Air Force Institute of Technology

AFIT Scholar

6-1998

Effects of Clutter Height Distribution on Adaptive Clutter Erasure Performance

Kelce Steven Wilson

Follow this and additional works at: https://scholar.afit.edu/etd

Part of the Signal Processing Commons

Recommended Citation

AFIT/DS/ENG/98-05

EFFECTS OF CLUTTER HEIGHT DISTRIBUTION ON

ADAPTIVE CLUTTER ERASURE PERFORMANCE

DISSERTATION
Kelce Steven Wilson
Captain, USAF

AFIT/DS/ENG/98-05

19980924 044

Approved for public release; distribution unlimited

The views expressed in this dissertation are those of the author and do not reflect the

official policy or position of the Department of Defense or the U.S. Government.

EFFECTS OF CLUTTER HEIGHT DISTRIBUTION ON

ADAPTIVE CLUTTER ERASURE PERFORMANCE

DISSERTATION

Presented to the Faculty of the School of Engineering

of the Air Force Institute of Technology

Air University in Partial Fulfillment of the

Requirements for the Degree of

Doctor of Philosophy

Kelce S. Wilson, B.S.E.E., M.S.E.E., M.B.A.

Captain, USAF

June 1998

AFIT/DS/ENG/98-05

EFFECTS OF CLUTTER HEIGHT DISTRIBUTION ON

ADAPTIVE CLUTTER ERASURE PERFORMANCE

Kelce S. Wilson, B.S.E.E., M.S.E.E., M.B.A.
Captain, USAF
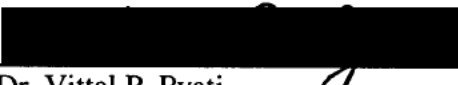
Approved:

Maj Michael A. Temple, PhD
Committee Chairman
Date 18 Aug 98

Maj Edward A. Pohl, PhD
Committee member
Date 18 Aug 98

Dr. Vittal P. Pyati
Committee member
Date 18 Aug 98

Maj Peter J. Collins, PhD
Committee member
Date 13 Aug 98

Dr. Thomas C. Hartrum
Dean's Representative
Date 18 Aug 98

Accepted:

Dr. Robert A. Calico, Jr.
Dean, Graduate School of Engineering

Acknowledgments

Table of Contents

List of Figures

vii

Abstract

A new real beam interferometric processing technique, called Adaptive Clutter Erasure (ACE), is investigated for applicability to ground clutter suppression in airborne radar systems. By analysis and simulation, the viability of the ACE concept as a next generation clutter suppression technique is demonstrated to achieve performance enhancements commensurate with currently implemented techniques. Research results indicate the ACE concept provides a reliably consistent 10 dB Signal-to-Clutter Ratio (SCR) advantage over the APG-63, an operational radar system used for baseline comparison. ACE system concept development and performance predictions are conducted in conformity with the physical and operational design parameters of the APG-63, namely the operating frequency band, typical tracking scenarios, aperture size and polarization, element spacing and weighting, and field pattern response. Performance degradations for the limited number of scenarios where ACE provides minimal or no advantage, i.e., scenarios including platform roll or large target depression angles, are "as expected" in the sense that simulation results are consistent with theoretically established principles.

In support of ACE concept validation, a novel multi-layer 3-D clutter model is developed by incorporating existing clutter reflectivity statistics and measured terrain elevation data. This new 3-D clutter model offers tremendous flexibility by accurately characterizing the relative altitude, slope, type, surface thickness, probabilistic reflectivity, and shadowing of terrain on a *pixel-by-pixel* basis. This is in sharp contrast to traditional 2-D

clutter modeling techniques which typically include deterministic backscatter characteristics and assume constant terrain characteristics within gated range cell regions, i.e., there are no terrain height variations within range cells. External to ACE concept validation, the 3-D clutter modeling approach provides the opportunity to improve terrain classification methodology and enhance radar calibration techniques.

A unique interpolation scheme is introduced to handle poorly behaved, under-sampled 3-D data such as commonly observed in measured terrain elevation values. The interpolation algorithm uses a modified cubic spline formulation and, for nearly all terrain conditions, accurately creates closely spaced interpolated results from sparse input data. Interpolation of Digital Terrain Elevation Data (DTED) by a factor of nine, i.e. calculating 285 million values at 30 meter intervals from a data set with 90 meter intervals in 2-D, produces a zero mean Gaussian error distribution with a standard deviation of two meters in elevation over rugged mountainous regions.

A probabilistic backscatter coefficient generator is introduced which produces realistic backscatter values for various terrain types at all incidence angles. The statistical properties of the generator output, i.e., the mean and standard deviation, match measured values to the number of significant figures reported. The frequency of occurrence of the generator output closely matches measured terrain data frequency of occurrence; a Chi-Square test fails to reject the generator method at a 0.05 level of significance, indicating confidence in the results. The generator accurately reflects expected scattering characteristics from the nine programmed terrain types over the full range of variability associated with real terrain.

EFFECTS OF CLUTTER HEIGHT DISTRIBUTION ON

ADAPTIVE CLUTTER ERASURE PERFORMANCE

1. Introduction

1.1 Traditional Clutter Suppression Techniques

Present air-to-air radars often exploit Doppler frequency shift to discriminate long range, moving airborne targets from stationary ground clutter [1]. Given the dynamics of typical air-to-air scenarios, airborne Doppler radar designs exploit relative motion characteristics, i.e., targets of interest travel with non-zero velocity relative to both the radar platform and ground. Using the geometry established in Fig 1, the relative velocity between an airborne target (scatterer) and radar platform is determined from Eq (1) where t denotes target, p denotes radar platform, θ_p is the angle between platform velocity vector, v_p, and relative velocity vector, v_r, and θ_t is the angle between target velocity vector, v_t, and relative velocity vector, v_r. For this convention, $v_t \cos(\theta_t)$ is positive for an approaching target. For a relative velocity given by Eq (1), radar returns exhibit an induced Doppler frequency shift as expressed by Eq (2).

$$v_r = v_t \cos \theta_t + v_p \cos \theta_p \tag{1}$$

$$f_d = \frac{2 v_r}{\lambda} \tag{2}$$
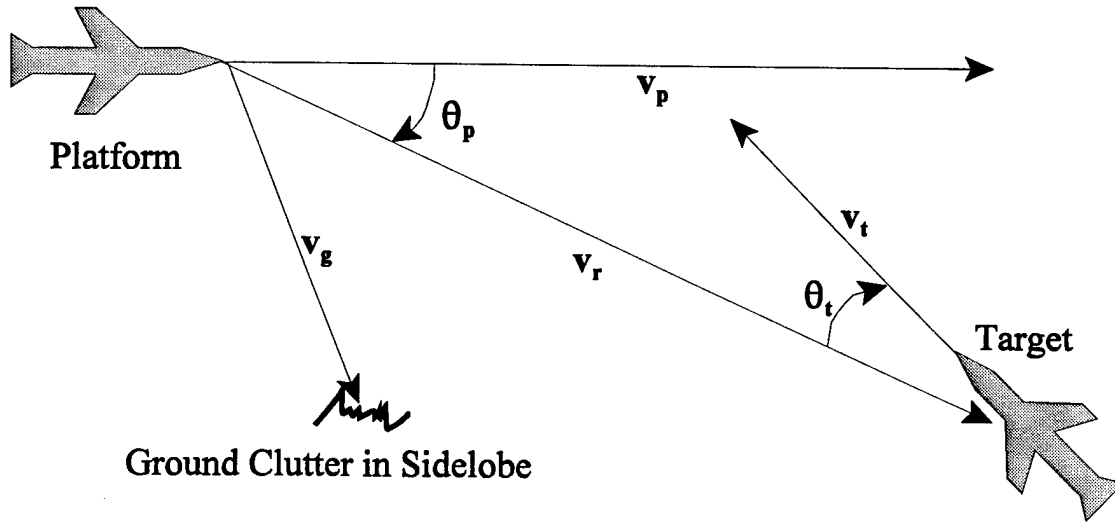
Figure 1: Doppler Detection Geometry
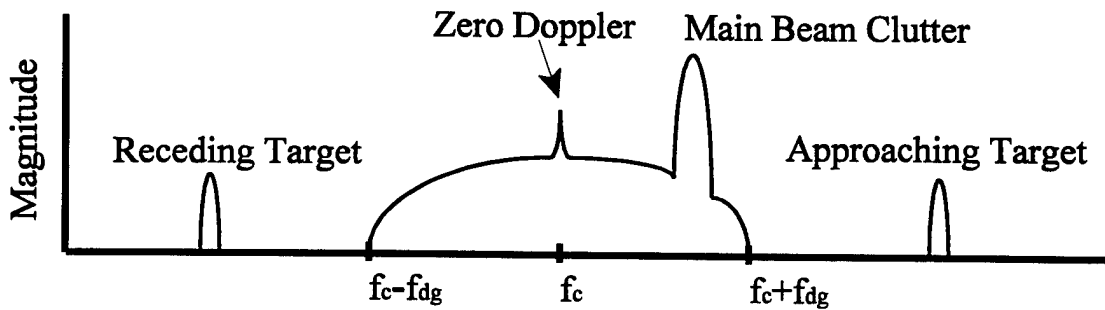
Figure 2: Doppler Spectrum with Ground Clutter and Targets

Since the ground is stationary relative to the radar platform, the shape of its Doppler frequency shift spectrum is determined solely by platform motion and antenna pattern characteristics. For straight and level flight, the range of possible θ_p values for ground reflection terms extends from 0 to $-\pi$. Under these conditions, the ground clutter Doppler spectrum is generated by a continuous collection of ground-based reflections over the full range of possible relative velocities, $-v_p$ to $+v_p$. The strength of a given frequency

component depends on platform velocity, v_p, ground reflectivity, and antenna pattern characteristics along v_r toward the ground. A typical airborne radar operating in a look-down mode receives returns (echos) with a frequency spectrum as illustrated in Fig 2. Here the return magnitudes are shown relative to f_c, the radar operating frequency, and f_{dg} is the maximum Doppler frequency induced from ground clutter. Doppler returns for an approaching and receding airborne target are also shown. From Fig 2 it is apparent how any airborne target with a relative velocity producing a Doppler frequency shift between $+f_{dg}$ and $-f_{dg}$ can be obscured in ground clutter returns. In fact, an airborne target flying a constant radius course relative to the radar platform, i.e., θ_r equal to $\pi/2$, induces a Doppler frequency shift identical to the ground clutter located directly below it, see Eq (1). Flying a constant radius course to exploit this behavior is a modern fighter tactic known as "beaming" or "notching," depending on whether the radar platform or target aircraft is performing the maneuver [2].

Range gating is often employed in conjunction with Doppler processing to enhance clutter suppression and improve target detection. A range gated receiver operating on a single pulse (range unambiguous mode) produces a change in the clutter return frequency spectrum, inducing frequency dependent attenuation consistent with the Fourier Transform of the shape of the range gate response in the time domain. The graphical representation and modified spectral response of a range gated Doppler system is shown in Figs 3 and 4, respectively. Although the clutter response has been attenuated relative to the ungated response of Fig 2, enough ground clutter energy remains within the range cell to mask legitimate targets.

3
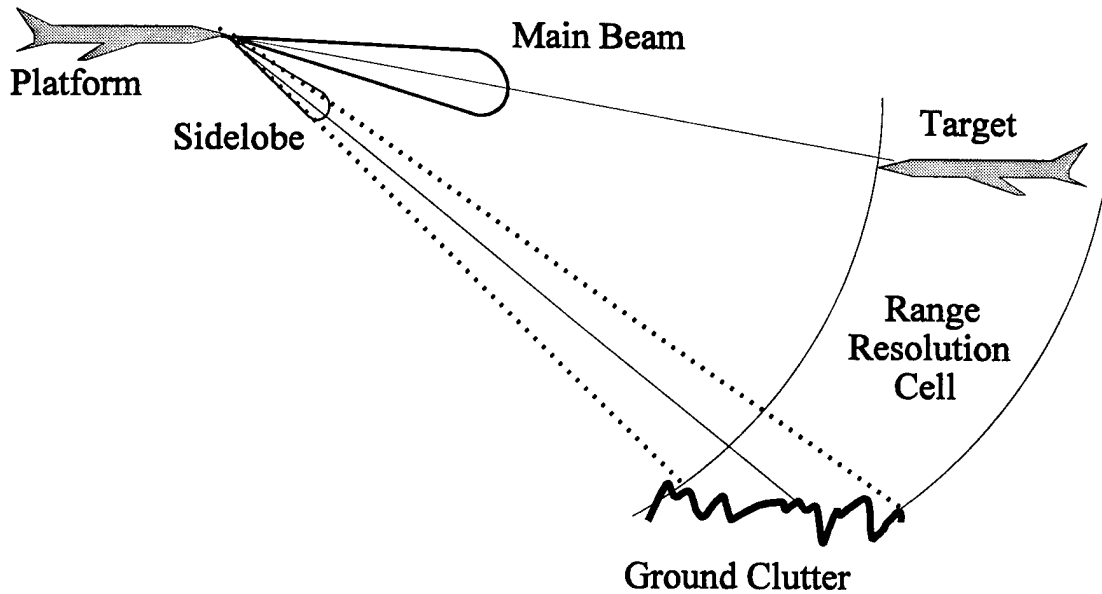
Figure 3: Range Gated Sidelobe Clutter
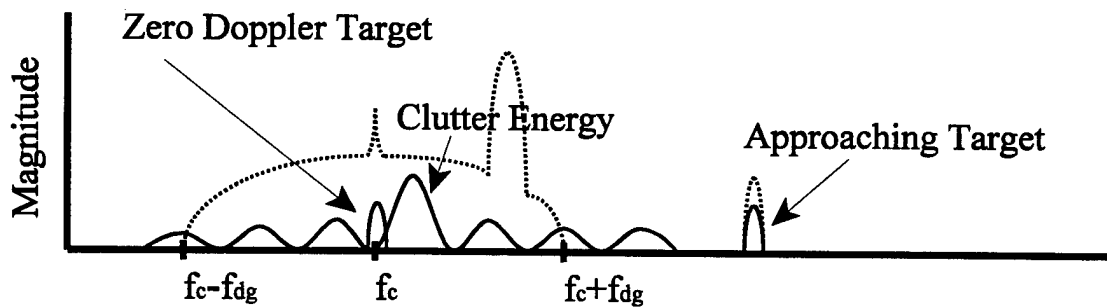
Figure 4: Range Gated Doppler Spectrum

1.2 Interferometric Clutter Suppression

Interferometric processing, or adaptive null steering, may be used independently or in conjunction with Doppler and range gating techniques to enhance target detection. Placing an antenna pattern null, either hardware or software generated, near the center of the ground clutter region of a given range cell, as illustrated in Fig 5, effectively attenuates the range

4

gated Doppler spectrum of Fig 4; the degree of attenuation is function of both null depth and width. Figure 6 shows the resultant Doppler spectrum obtained by combining range gating and interferometric nulling.
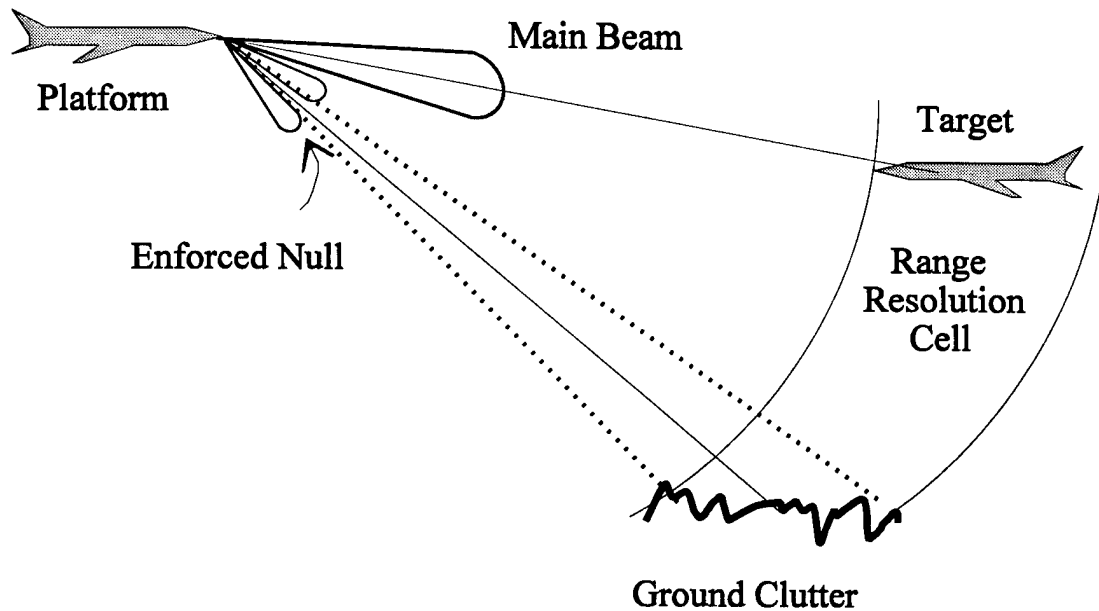
Figure 5: Sidelobe Clutter With Interferometry
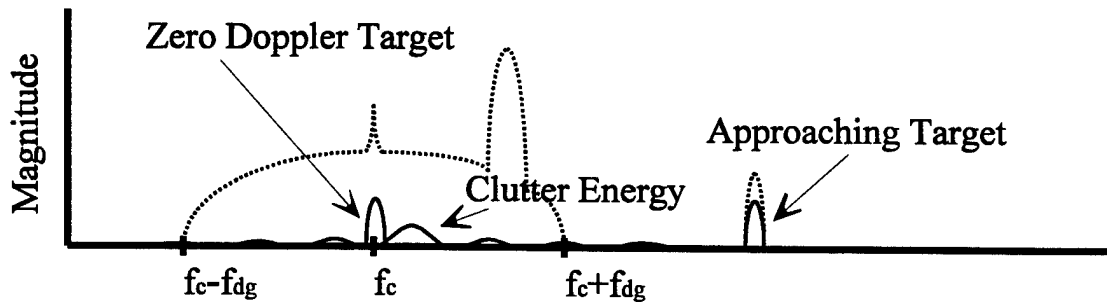
Figure 6: Range Gated Doppler Spectrum With Interferometry

The use of interferometry to enhance performance of airborne radar systems is not a new concept. Two existing techniques, Ground Moving Target Indicator (GMTI) and Interferometric Synthetic Aperture Radar (IFSAR), have successfully exploited

5

interferometry to enhance ground target detection. Air-to-ground radars employing Doppler detection techniques often fail to find moving ground targets because the frequency shift caused by such targets falls within the ground clutter spectrum. GMTI radars find slowly moving ground based targets by using horizontally displaced phase centers to cancel stationary clutter in a field of returns; ground targets which have moved between successive pulse groups survive the clutter erasure procedure. Radars such as the APG-73 use GMTI techniques and *near real-time* interferometry to detect targets [3]. One limitation of these systems is an inherent vulnerability to wind effects, i.e., random motion of objects caused by the wind induces a Doppler frequency shift consistent with slower moving ground targets and thus masks legitimate ground targets.

Airborne IFSAR ground mapping systems use platform motion and aperture phase center displacement to produce ground maps via interferometry, i.e., return signal phase difference estimates between coherent SAR maps are used to determine the vertical pixel height in a processed map. The signal phase differences result from differing path lengths between displaced aperture centers and corresponds directly with the height of a single equivalent dominant scatterer as shown in Fig 7.
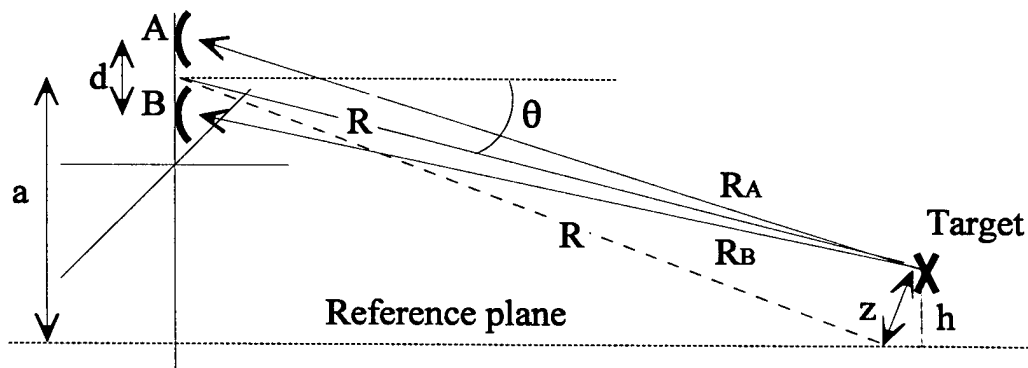
Figure 7: Simple Interferometric System

In Fig 7, d is the separation distance of the phase centers, θ is the viewing angle depression, R is the distance from the target to the center of the aperture arrangement, z is the distance from the target to the reference plane measured perpendicular to R, a is the altitude of the platform above the common ground plane, and R_A and R_B are the path lengths from the target to the respective apertures.

Two SAR maps, created from signals arriving at different apertures, can be combined to create the overall 3-D SAR image as shown in Fig 8, although many IFSAR systems use horizontally displaced phase centers.

Channel A and B SAR Maps   3-D SAR Map
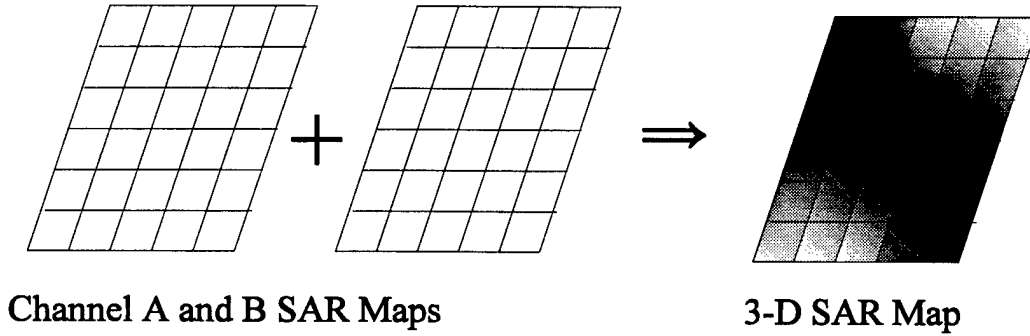
Figure 8: IFSAR Map Creation

If only one aperture transmits, the ground reflection path lengths to apertures A and B differ, resulting in a phase difference of:

$$e^{j\gamma} = e^{jkd\cos\theta\frac{z}{R}} \qquad (3)$$

Equation (3) assumes both channels are co-phased to a common ground reference plane from which z is measured. Here, k is the wave number, and γ is found from:

$$\gamma = \tan^{-1} \left(\frac{\text{Im}\{ S_A S_B{}^\star \}}{\text{Re}\{ S_A S_B{}^\star \}} \right) \qquad (4)$$

S_A is the signal arriving at aperture A, S_B is the signal arriving at aperture B, and R is the range to the resolution cell. It is important to note that these equations assume a single scatterer at a single height in each resolution cell [4, 5].

Equation (4) is solved from the signal set after co-phasing the channels to the reference plane, and the relationship in Eq (3) is then used to establish z. R and θ are found via simple geometry relating platform location data and range gating. Height above the reference ground plane can be found easily from:

$$h = z \cos \theta \qquad (5)$$

IFSAR systems are generally limited to operating with height variations giving a γ between $+\pi$ and $-\pi$. Outside this region, not only does the pixel height become ambiguous, but also the straight line approximation of $\sin(z/R) \approx z/R$ begins to break down and the right side of Eq (3) predicts an incorrect interferometric lobing structure.

Despite the current advances in IFSAR and GMTI technologies, and their applicability to ground based target detection, the application of interferometry to airborne target detection is yet largely unexplored [1].

1.3 Interferometric Airborne Target Detection

Interferometric Clutter Erasure (ICE) is a proposed airborne target detection concept that is used in conjunction with IFSAR processing [6]. Simply stated, the ICE technique is

8

a clutter suppression process that involves "erasing" the ground from beneath airborne targets. Given a target of interest is suspended within "view" of an IFSAR system, the IFSAR mapping process yields a relatively accurate ground map that contains anomalies associated with the target's presence. By "smoothing" over the anomalous points (equivalent to replacing anomalous target data with terrain estimates) a new image is created and "subtracted" from the original image; at this point the ICE process is complete and the remaining image (signal) is assumed to be coming from a reflector *not on the ground.*

It is obvious from the preceding discussion that ICE performance is highly dependent on terrain characteristics and IFSAR mapping capability. Specifically, the ability to produce reasonably accurate and timely estimates of ground clutter height is a major concern for the implementation of the ICE concept. Clutter height variations result from two factors, local roughness and terrain variation (physical character of the ground). Local roughness, or "ground thickness," is defined in this research effort as any variation in clutter height that occurs within a single SAR-sized resolution cell such as caused by trees, rocks, and buildings. Terrain variation includes things such as hills and valleys and occurs on a large enough scale to be easily distinguished on a fine resolution IFSAR map.

Implementation of a *near real-time* interferometry technique, such as the ICE concept, for an air-to-air role requires an aperture with certain critical features, including, two or more vertically stacked phase centers with identical radiation patterns. GMTI and IFSAR techniques typically use horizontally separated phase centers; GMTI uses a left/right configuration while many aircraft mounted and satellite multi-pass IFSAR systems use a front/back configuration [4]. Each of these configurations is depicted in Fig 9 for a platform

moving in the positive x direction. Although typical IFSAR systems use horizontally separated phase centers to meet the steep observation angle requirement, the aperture configuration and specific mission requirements of APG-76 dictate the use vertical phase centers for creating IFSAR maps [7].
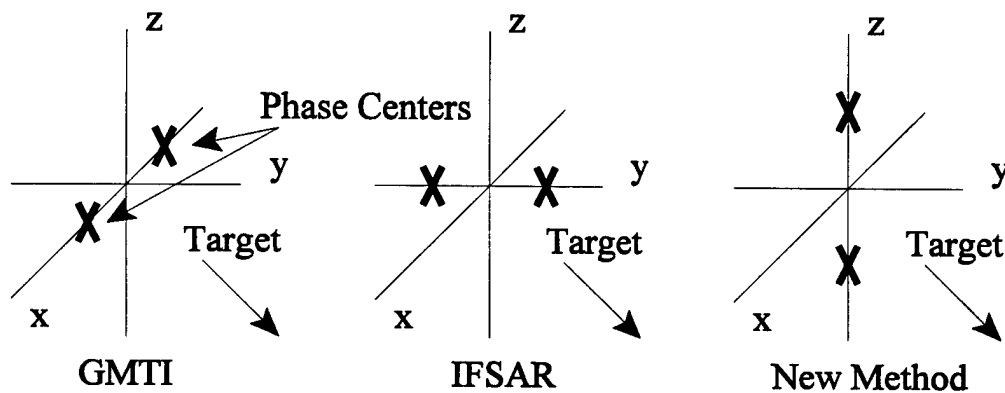
Figure 9: Phase Center Location for Various Interferometry Techniques

The interferometric system describing the ICE concept is shown in Fig 10 and is slightly different than the system shown in Fig 7, since now the "target" is a reflector *above* the ground and the ground is redefined as *clutter*.
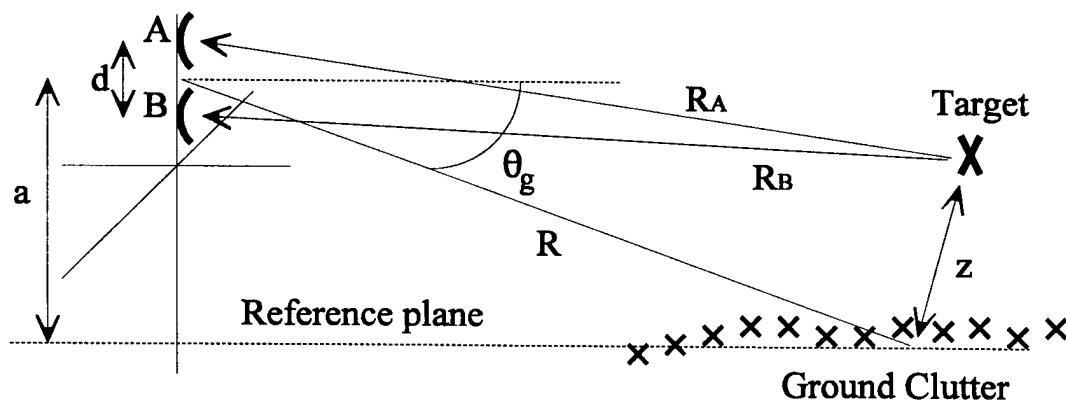
Figure 10: ICE System with Non-Planar Ground Profile

10

Using A and B to denote the pixel heights, with a and b denoting the smoothed map heights (moving average window in 2-D), the ICE system voltage can be described as:

$$V_{ICE} = A - \frac{ab^\star}{|ab|}B \tag{6}$$

An anomalous pixel may return a non-zero value, so that a target can be declared when this value exceeds some threshold. The equivalent single scatterer model describing this situation is shown in Fig 11.
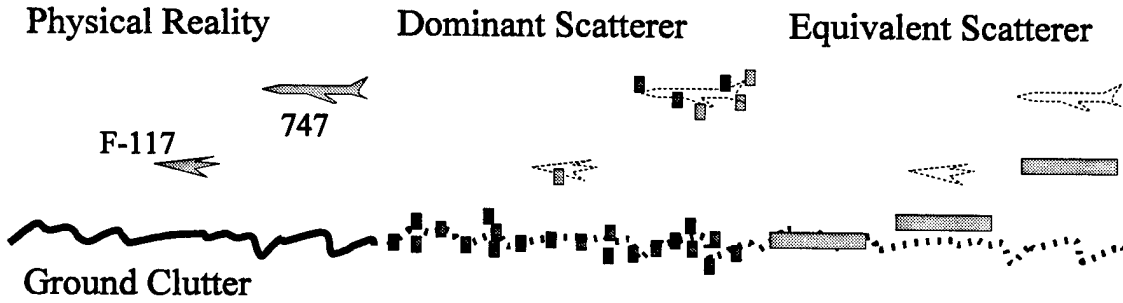
Figure 11: Scattering Models for ICE

A second perspective of the process yields the following formulation:

$$S_B - S_A = \sigma G \left(e^{jk\frac{d}{2}\cos\theta_g \frac{z}{R}} - e^{-jk\frac{d}{2}\cos\theta_g \frac{z}{R}} \right) = 2j\,\sigma G \sin\left(k\frac{d}{2}\cos\theta_g \frac{z}{R} \right) \tag{7}$$

This is the result of subtracting the 2 channels' signals to cancel out ground clutter. The new representation indicates that the target echo power is proportional to its altitude and has a sine functional dependence However, this formulation is only valid for targets inside the first interferometric lobe.

As with all interferometric clutter suppression techniques, the performance of an ICE system depends on many factors, including, target and ground clutter RCS characteristics,

11

receiver channel match, number of receiver channels, target height, ground height/location estimates, ground height variations, ground "thickness", antenna patterns, and any incorporated resolution enhancements (SAR, DBS).

1.4 Adaptive Clutter Erasure Concept

Adaptive Clutter Erasure (ACE) is a derivative of ICE that is suited for a real beam radar. Fighter-type radars typically search for targets using a narrow beam antenna pattern and cannot afford to compromise gain in the boresight direction. The ACE concept calls for a *near real-time* interferometric capability, similar to ICE, modifying the radar aperture itself to create nulls on a real-beam antenna pattern pointed in the direction toward the ground rather than nulling out the ground in a generated IFSAR type map. To perform this action, an ACE system must control at least two displaced phase center locations to actively steer a null or series of nulls while preserving main beam gain in the radar tracking direction. This highlights the different use of ICE as a search system and ACE as a tracking system.

Specifically, ACE modifies distance d in Fig 10 as necessary to introduce a constant azimuth null in the direction to the ground, θ_g. This is in contrast to ICE which maintains a constant distance d in Eq (7) while applying a phase shift to S_A relative to S_B to produce a system null at the expected height of a pixel. Since an IFSAR map is not being formed with ACE, the direction to the ground at the center of the range cell, θ_g, must be estimated given flight attitude, altitude, and aperture pointing direction. An example of the ACE variables applied to both a mechanically and electrically scanned aperture is shown in Fig 12.

12

Although this effort examines implementation using a mechanically scanned aperture, the concept applies equally well to systems with electrically scanned apertures.
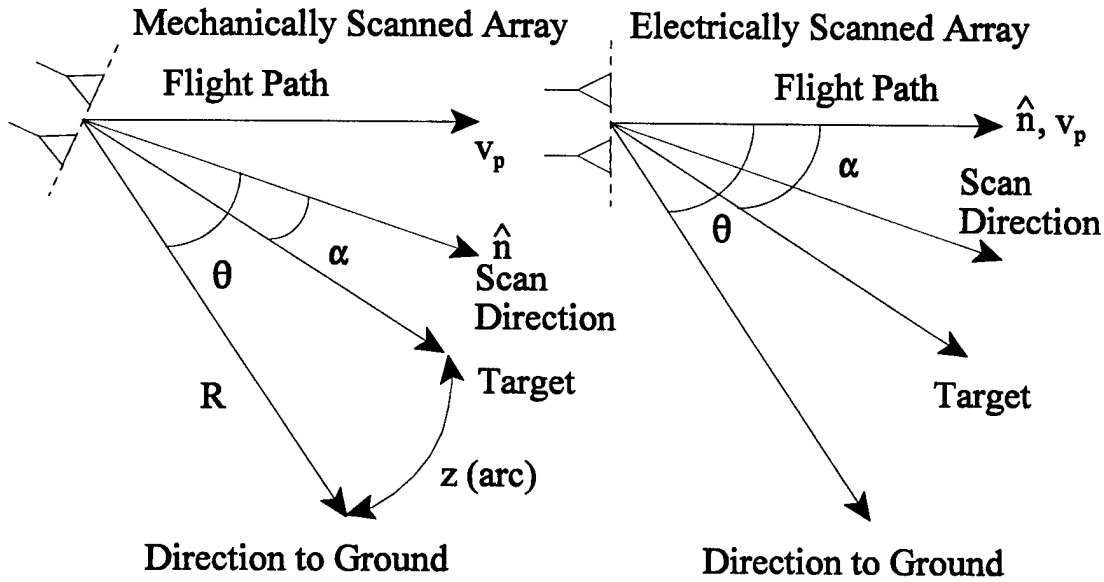
Figure 12: ACE Variables Relating to Radar Aperture

It is important to note that depression angle θ is measured as the angle between the aperture surface normal vector and a vector pointing in the direction toward the ground in the center of the range cell under consideration. For a mechanically scanned array, $\hat{n}$ is mechanical boresight and the direction of the main beam. For a forward pointing phased array, θ is the angle between the platform velocity vector and the direction toward the ground. For a mechanically scanned array in tracking mode, the main beam is generally at $\alpha = 0$ so the gain in this direction must be maintained. For an electronically scanned array, the problem becomes more complicated since the main beam can be at any angle; regardless of the angle, the gain must still be preserved. This latter case presents another level of complexity since a carelessly constructed interferometer may not only place a null on the

13

ground, but also may place a null coincident with the phase scanned main beam. This angle can typically vary up to ±30° in current phased array apertures, so the interferometer construction must adapt to a second constraint: *where not to place a null*. The ACE adaptation to a phased array aperture is only mentioned here by contrast to mechanically scanned apertures and is not examined in detail.

Space-Time Adaptive Processing (STAP) technology has many similarities to ACE although it is more closely related to the ICE concept. STAP combines of signals from elements of array antennas using multiple pulses of a coherent radar waveform to suppress interference and improve target detection [8, 9]. It is a digital beam-forming process that creates nulls in a desired direction using apertures with a given number of ports, each connected to an element or group of array elements. STAP techniques are primarily applicable to large airborne search radars such as the Airborne Warning and Control System (AWACS) [9]. The Doppler processing and fixed aperture configurations used in STAP are equivalent to the SAR processing and fixed phase center constraints in the ICE concept. These are important differences from the ACE system concept defined here, as neither technique, ICE or STAP, qualifies as a real beam technique.

1.5 Document Preview

A detailed analysis of the ACE concept implementation is provided in Chapter 2 along with an initial prototype design used for simulation and validation. The APG-63, a current operational system, is used for baseline perfromance comparison. It is a look-down capable Pulse Doppler system that performs air-to-air search and tracking using a low

sidelobe aperture specifically designed for clutter suppression. The initial ACE system concept is investigated within the physical constraints and operational parameters of the APG-63, including operating frequency band, typical tracking scenarios, aperture size and polarization, element spacing and weighting, field pattern response, and range resolution. Details necessary for creating a high-fidelity digital model of the baseline APG-63 system are readily available. As described in Chapter 2, the extension of this system to an ACE model is straightforward.

The benefit of using an optimized baseline system that is presently used in the same role envisioned for ACE is that performance improvements over currently implemented techniques can be investigated. Additionally, imposing identical physical limitations, i.e., common aperture specifications and resolution cell size, provide realistic improvement predictions rather than predictions based on an impractical idealized design.

Chapter 3 outlines the digital model design philosophy and limitations and highlights the need for development of two sub-models: 1) a terrain backscatter coefficient generator which is described in Chapter 4, and 2) a new terrain interpolator, introduced in Chapter 5, to translate available terrain elevation data to elevation posts at positions needed by the digital model. The backscatter coefficient generator is a probabilistic model based on measured statistics of various terrain types, providing the proper range and variability of real backscatter characteristics. This is in direct contrast with traditional backscatter prediction methods which only provide the expected value of the backscatter for a given terrain type under defined observation conditions.

The terrain interpolator is designed to handle poorly behaved, under-sampled 3-D data such as commonly observed in measured terrain elevation values. The algorithm uses a modified cubic spline formulation and, for nearly all terrain conditions, accurately creates both closely spaced interpolated results from sparse input data and new data sets with different post spacing intervals in 2-D. That is, the algorithm accurately converts a data set with posts of equal arc-second spacing to a data set with posts spaced equally in meters in both dimensions.

Combining the new techniques from Chapters 4 and 5 results in a novel multi-layer 3-D clutter model with tremendous flexibility that accurately characterizes altitude, slope, type, probabilistic reflectivity, and shadowing of terrain on a *pixel-by-pixel* basis. This is in sharp contrast to traditional 2-D clutter modeling techniques which typically include deterministic backscatter characteristics and assume constant terrain. The new model is validated against theoretically predicted results in Chapter 6. External to ACE concept validation, the 3-D clutter modeling approach provides the opportunity to improve terrain classification methodology and enhance radar calibration techniques.

Model results of Chapter 7 indicate a reliably consistent 10 dB Signal-to-Clutter Ratio (SCR) advantage over the APG-63. Performance degradations for the limited number of scenarios where ACE provides minimal or no advantage are *"as expected"* in the sense that simulation results are consistent with predictions from Chapter 2.

2. Theory and Analysis

The ideal ACE system is analyzed using an electromagnetic ray trace propagation technique. The ray trace technique is a valid approach provided the pixel locations, corresponding to ray-clutter intersection points, are appropriately spaced. The analysis begins by using a single ray per ACE sub-aperture which is closely aligned along the boresight of each sub-aperture, as shown in Fig 13. The array is assumed to be mechanically scanned in the direction of the target, i.e., the target is always located on the mechanical boresight axis. The analysis is then expand to incorporate diverging ray bundles, one ray per each sub-aperture element, to examine antenna pattern sidelobe effects.

One way to analyze the ACE concept is to characterize the Signal-to-Clutter Ratio (SCR) for various terrain types, target characteristics, platform dynamics, and aperture configurations, both with and without ACE. The SCR is highly dependent on the nature of the terrain, the Radar Cross Section (RCS) of the target, and platform orientation, and thus provides a measure of system effectiveness improvement.

As defined in Section 2.2, the SCR metric is examined as a way to optimize ACE performance. Probability of Detection (P_D) and False Alarm Rate (FAR) are heavily dependent on this value; maximizing SCR likely improves P_D while simultaneously reducing the FAR. The primary focus of this research effort is pre-detection optimization of aperture interferometry techniques. Signal processing techniques beyond basic interferometry may be used to improve P_D further, but are outside the scope of this effort.

2.1 Signal Phase Information

For high altitude targets, the geometry established in Fig 13 is used to establish the interferometric relationships shown in Fig 14. For this configuration, θ is the depression angle measured from the target to a specific ground clutter point. There is no ground plane phase reference for the ACE system, as in IFSAR or ICE. Rather, exact signal phases are calculated relative to the center of the aperture pair. Given a target located on aperture boresight at range R, signals received by sub-apertures A and B, S_A and S_B, resulting from propagation along paths R_A and R_B, respectively, exhibit no phase difference and add constructively, a difference from the initial ICE concept.
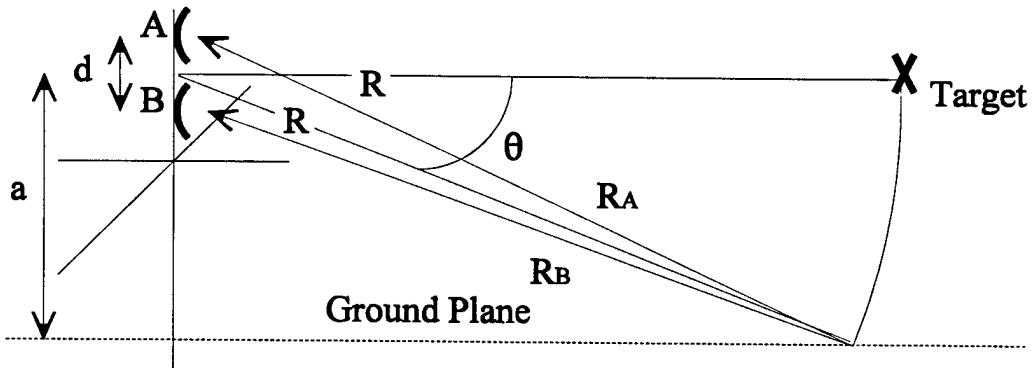
Figure 13: An "Exact" Interferometric System

For ground clutter located at the same range as the target, the sub-aperture signals are given by Eq (8) where σ is complex clutter reflectivity, K is the propagation constant $2\pi/\lambda$, $G(\theta)$ is a complex weighting function which accounts for range, antenna gain, and other factors affecting received voltage levels, and Γ is a composite phase reflection term at the center of a range cell.

18

$$S_A = \sigma G_A(\theta) e^{-jK(R+R_A)} e^{j\Gamma}$$
$$S_B = \sigma G_B(\theta) e^{-jK(R+R_B)} e^{j\Gamma} \tag{8}$$

Assuming a perfect channel match, $G_A(\theta) = G_B(\theta) = G(\theta)$, the channel signals can be combined into one term as shown in Eq (9) where the Γ represents an overall phase.

$$S_A + S_B = \sigma G(\theta) \left\{ e^{-jK(R_A - R_B)} + 1 \right\} e^{-jK(R+R_B)}$$

$$= \sigma G(\theta) \left\{ e^{jK\frac{(R_A - R_B)}{2}} + e^{-jK\frac{(R_A - R_B)}{2}} \right\} e^{j\Gamma} \tag{9}$$

Figure 14 provides a close-up view of the geometrical relationships in Fig 13.
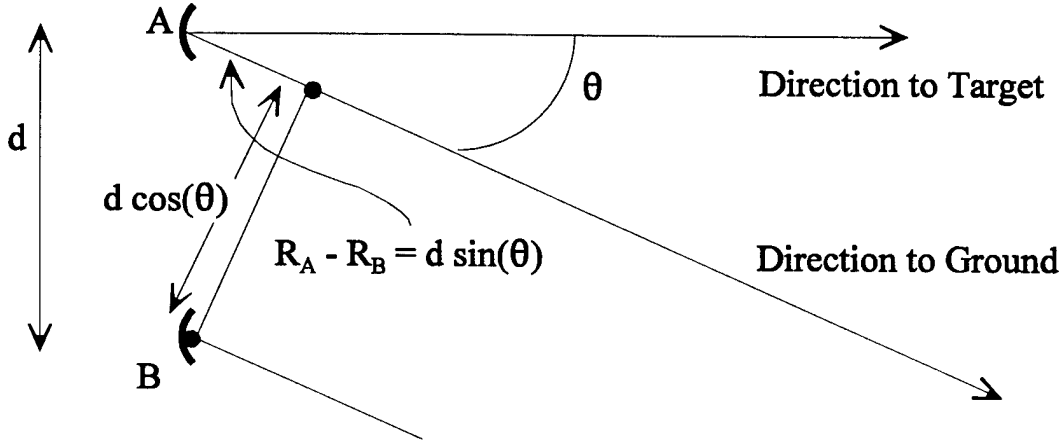
Figure 14: Close-up of ACE Phase Differences

From the relationships given in Fig 14, Eq (8) may be re-written as:

$$S_A = \sigma G_A(\theta) e^{jK\frac{d}{2}\sin\theta} e^{j\Gamma_3}$$

$$S_B = \sigma G_B(\theta) e^{-jK\frac{d}{2}\sin\theta} e^{j\Gamma_3} \tag{10}$$

19

Normalizing the phase, Eq (9) may be rewritten as shown in Eq (11).

$$S_A + S_B = \sigma G(\theta) \left(e^{jK\frac{d}{2}\sin\theta} + e^{-jK\frac{d}{2}\sin\theta} \right) \tag{11}$$

The final ACE voltage, V_{ACE}, may then be expressed as given by Eq (12) where the function $I(K,d,\theta)$ is the *interferometric pattern* and it is assumed that no additional phase shift has been added to either of the sub-aperture channels.

$$V_{ACE} = S_A + S_B = 2\sigma G(\theta) \cos\left(K\frac{d}{2}\sin\theta \right) = 2\sigma G(\theta) I(K,d,\theta) \tag{12}$$

If the interferometer nulls, i.e., nulls of $I(K,d,\theta)$, are not located at the appropriate places, it is possible to introduce a phase difference between the two sub-aperture channels and steer the nulls electrically. However, this should only be considered an option if doing so will reduce sidelobe clutter power by an amount greater than the reduction of received signal power. Revisiting the ACE voltage development process, applying a phase shift of γ on sub-aperture A results in the V_{ACE} expression given by Eq (13) and an interferometric pattern given by Eq (14). Equation (14) indicates that for a small, non-zero γ, the inteferometric pattern has a boresight gain ($\theta = 0$) of slightly less than unity.

$$V_{ACE-shifted} \propto e^{-jK(R_A+R)} \cdot e^{j\gamma} + e^{-jK(R_B+R)} \tag{13}$$

$$I(K,d,\theta,\gamma) = \cos\left(K\frac{d}{2}\sin\theta + \frac{\gamma}{2} \right) \tag{14}$$

For an electronically scanned phased array aperture, the formulation is slightly different, producing the exact voltage formula given by Eq (15) where α is the angle between aperture surface normal $\hat{n}$ and the scanned mainbeam direction.

$$V_{ACE, \text{ Phased Array}} = \sigma G(\theta) \cos\left[K\frac{d}{2}(\sin\theta - \sin\alpha)\right]$$ (15)

2.2 Clutter Erasure Considerations

The ability of an ACE system to suppress or minimize received clutter power, power which typically competes with or masks legitimate target returns, is measured by the improvement in the Signal-to-Clutter Ratio (SCR) of the ACE system relative to a traditional radar system. The scattering center system of Fig 15 is used to develop and analyze an ideal interferometer model which incorporates multiple scattering centers.
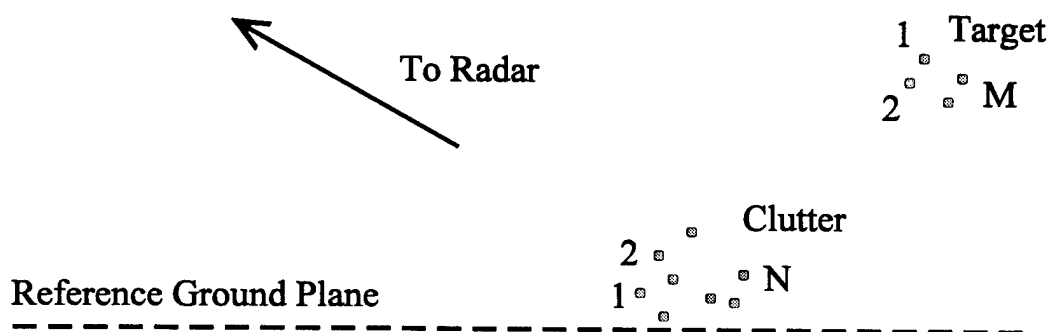
Figure 15: Multiple Scattering Center System

A ray trace analysis examines the situation of multiple dominant scatterers, one collection of M scatterers representing the airborne target and one collection of N scatterers representing ground clutter. Under these conditions, the SCR relationship given by Eq (16)

21

is constructed for a non-phase shifted mechanically scanned aperture. The expected value operator, $E\{x\}$, accounts for the probabilistic nature of scattering center location, number, and complex reflectivity. The denominator of Eq (16) represents the clutter "floor" which, as expressed in Eq (17), is the amount of clutter power, $P_{Clutter}$, surviving the interferometric erasure process.

$$SCR = \frac{E\left\{\left|\sum_{m=1}^{M} \sigma_m G(\theta_m) \cos\left[K\frac{d}{2}\sin(\theta_m)\right]\right|^2\right\}}{E\left\{\left|\sum_{n=1}^{N} \sigma_n G(\theta_n) \cos\left[K\frac{d}{2}\sin(\theta_n)\right]\right|^2\right\}} \tag{16}$$

$$P_{Clutter} = E\left\{\left|\sum_{n=1}^{N} \sigma_n G(\theta_n) \cos\left[K\frac{d}{2}\sin(\theta_n)\right]\right|^2\right\} \tag{17}$$

The behavior of $P_{Clutter}$ is dependent upon clutter reflectivity characteristics, channel matching, terrain height characteristics (thickness, density, and variation), antenna pattern characteristics, and specific radar resolution enhancements or techniques that are employed, i.e.. Synthetatic Aperture Radar (SAR), Doppler Beam Sharpening (DBS), range gating, etc. Additionally, SCR behavior is dependent on target RCS characteristics and altitude above the clutter.

The ACE system, as defined for this research effort, uses single pulse transmission and range gated detection. Range gating limits the physical region, or extent, over which clutter element backscatter contributes to overall returned clutter power. The goal of an ACE

system is to adjust interferometer characteristics such that a null is placed on the ground at the center of a given range cell. The incorporation of SAR and DBS techniques is not examined under this effort. However, nothing in the proposed definition or implementation of ACE prohibits or limits the implementation of either technique. Without SAR or DBS technique implementation, the resolution cell is bounded by range gating front to back, but subject to all radiation pattern sidelobes in azimuth.

Any channel mismatch between ACE sub-apertures will limit system performance. For purposes of this investigation, channel mismatch limitations are not considered. The erasure performance as a function of clutter reflectivity, ground height estimation, and aperture configuration is addressed in later sections.

2.3 Interferometer Phase Center Separation Distance and Null Placement

Examination of Eqs (12) and (14) reveal that if sub-aperture channel phase is not used to control desired null location, say θ degrees toward the ground, phase center separation distance, d, is the only remaining parameter that determines interferometer null location. The ability of an ACE system to enhance performance is directly related to its ability to determine and control sub-aperture phase center separation. Optimal selection of d results in optimal clutter cancellation, except for rare anomalous situations when a non-optimal d might actually produce a lower clutter power due to the interaction of sidelobe phase and weights with essentially random terrain elevations and reflectivities. Performance of a baseline digital system model is compared with an ACE enhanced version of the model to determine relative SCR improvement.

23

The baseline system for this research effort is the APG-63 Pulse Doppler radar system. Its aperture is a circularly planar array consisting of linearly polarized slots with slightly different horizontal and vertical element spacing. The array is approximately 30 inches in diameter and uses a "cosine-on-a-pedestal" tapered amplitude weighting to reduce sidelobe levels and enhance target tracking performance. This aperture has been digitally modeled and its performance verified against published data [10].

The total physical size of the ACE configuration sub-apertures, i.e., the displaced phase center interferometer aperture pair, is restricted to match the APG-63 planar array dimensions. The baseline aperture weighting scheme and element separation distances are maintained. However, the tapered amplitude weighting is compressed and repeated vertically for each ACE sub-aperture, producing two vertically separate phase centers in the same physical space. The main difference between the modeled ACE system and the baseline aperture is that 11 possible amplitude weighting schemes are instantaneously selected for application to the over 1300 array elements. The system is modeled to operate at 10.0 GHz, a typical operating frequency for radars of this type.

The 11 aperture configurations considered include: nine specific ACE configurations, the baseline APG-63 tapered cosine weighting, and a uniformly weighted scheme. For all configurations, individual elements are modeled as having a cosine field pattern response. The nine different ACE configurations cover most of the desired target depression angle range while simultaneously maximizing the percentage of aperture usage. Designated as the ACE-17 thru ACE-25 configurations, they provide sub-aperture phase center separation distances (d) that range from 17 to 25 vertical element spacings. The discrete number of

configurations results from an attempt to keep current model parameters on par with existing system complexity and the fact that the baseline aperture uses a fixed number of elements at fixed locations. Creating a continuous range of null locations would require either a continuously variable range of amplitude weighting or the use of sub-aperture phase shifting. As shown later, neither provides any significant performance improvement, relative to the suite of fixed configurations, to justify the added implementation complexity that each involves.

The nine ACE configurations provide null coverage, with some minimum null depth, over a target depression angle range of about 10 to 85 degrees. A graphical representation of the total aperture area available for ACE implementation and the active region used by the ACE-21 configuration is shown in Fig 16. As shown, the ACE-21 configuration with a 21 element phase center separation distance uses only about 83% of the total available aperture surface area. As a result, the maximum boresight gain for the ACE-21 configuration is reduced by 1.6 dB relative to the baseline system. Overall, maximum boresight gain reductions range from 1.6 dB to 4.1 dB for the nine ACE configurations with the ACE-21 configuration being the most efficient in terms of aperture utilization. Taking this reduction into account, the purpose of this research is to determine whether clutter power is reduced by an even larger margin for ACE implementations, resulting in a net increase in the SCR despite the drop in signal energy.
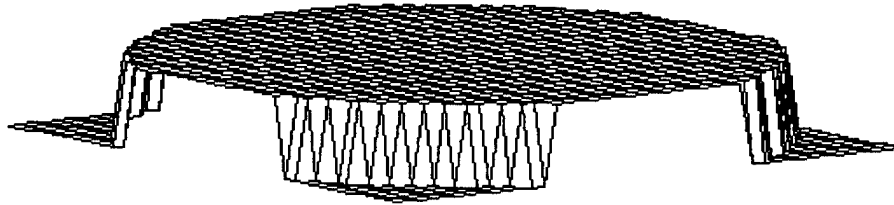
Potential Aperture Usage Area

Actual ACE-21 Aperture Usage Area
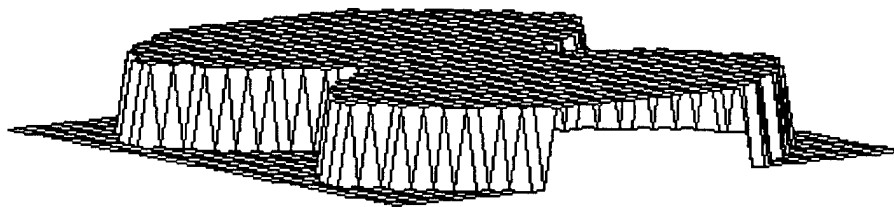
Figure 16: Potential and Active Regions of ACE Aperture

Contour plots for ACE configuration sub-aperture amplitude weightings are shown in Fig 17. The top left plot is for the 17 element separation configuration (ACE-17) and, counting across from top to bottom, the 25 element separation configuration (ACE-25) is on the bottom right. The amplitude taper profile for each configuration is a scaled version of the baseline amplitude taper - - identical in the horizontal direction and reproduced twice in the vertical direction, once for each sub-aperture, producing two distinct phase centers. A profile of the baseline amplitude taper is shown in Fig 18.
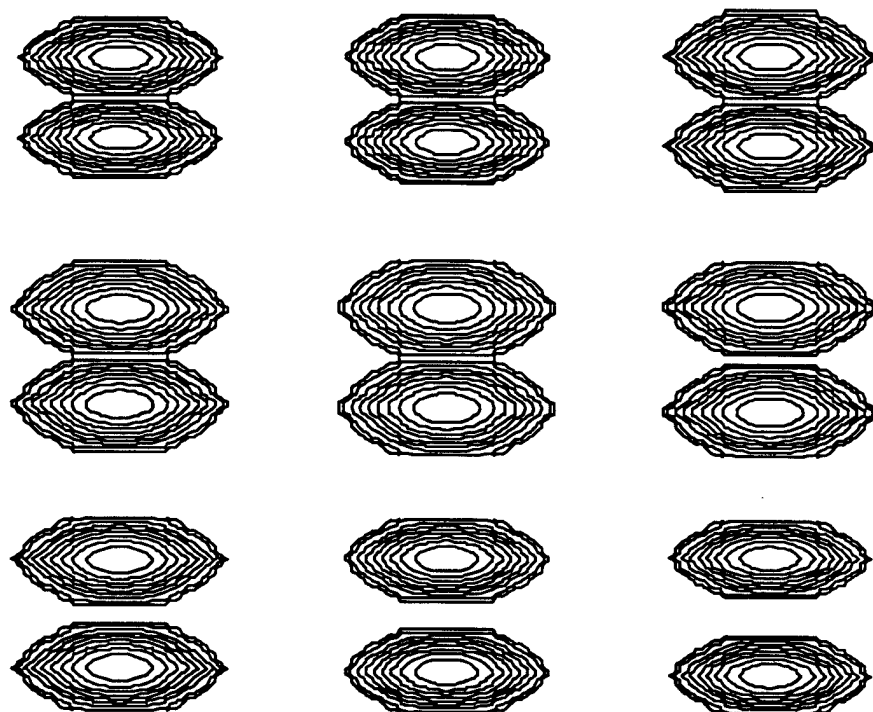
Figure 17: ACE Sub-Aperture Element Weighting

Element Position

— — Baseline System   ———— ACE-21 System
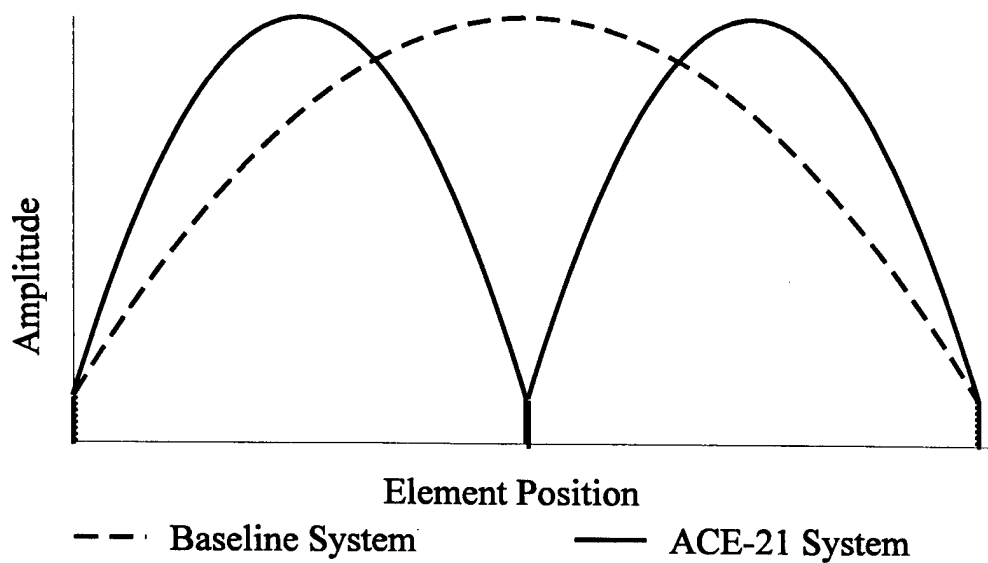
Figure 18: Tapered Amplitude Weighting Profiles

Given multiple aperture weighting configurations are available, the question arises as to how to select the *best* configuration for a given scenario. The selection can made on the basis of predicted interferogram null locations relative to the ground direction for a given range cell. Given that each ACE configuration produces multiple nulls, it possible for two or more configurations to produce a null at nearly the same angle. However, the more the phase separation distance, *d*, deviates from the ACE-21 configuration, the less efficiently the available aperture area is used, and the lower main beam gain will be. To preserve maximum signal power, the configuration satisfying Eq (18) is selected. Notice that *d/λ* is a discrete set where *λ* is the radar's operating wavelength and *dy* is the vertical element spacing.

$$\left(\frac{d}{\lambda}\right)_{Optimum} = \left(\frac{d}{\lambda}\right)_{n}$$

$$\text{Where:} \quad \left(\frac{d}{\lambda}\right)\left(\frac{\lambda}{dy}\right) = \{17, 18, \ldots, 25\}$$

(18)

$$\text{Such That:} \quad \cos\left[K\frac{d}{2}\sin(\theta)\right] \le \text{Null Depth Threshold}$$

$$\text{and} \quad \left|\left(\frac{d}{\lambda}\right)\left(\frac{\lambda}{dy}\right) - 21\right| \quad \text{is Minimized}$$

The solution to Eq(18) can be found using the following algorithm:

$$\text{Set:} \quad I(K,d,\theta) = \cos\left(K\frac{d}{2}\sin\theta\right) = 0$$

(19)

28

$$\cos\left(K\frac{d}{2}\sin\theta\right) = \cos\left(\frac{2\pi}{\lambda}\frac{d}{2}\sin\theta\right) = \cos\left(\frac{d}{\lambda}\pi\sin\theta\right) = 0 \qquad (20)$$

$$\cos\left(\frac{d}{\lambda}\pi\sin\theta\right) = 0$$

$$(21)$$

$$\text{when} \quad \frac{d}{\lambda}\pi\sin\theta = \frac{(2n+1)\pi}{2} \quad \text{or} \quad \left(\frac{d}{\lambda}\right)_n = \frac{(2n+1)\pi}{2\sin\theta}$$

The ACE configuration selection algorithm implements a solution using Eqs (19) thru (21) by solving for d/λ between some maximum and minimum values and closest to a corresponding d/dy of 21 in order to maximize aperture use efficiency. The interferometer pattern is then checked to determine if it provides a solution below a specified null depth threshold value, typically between -20 dB and -30 dB depending on the desired θ value. Integer n provides a discrete set of possible d/dy values. Figure 19 shows the algorithm results for θ between 10 and 85 degrees and d/λ in the range used for this research.

The selected d/λ value is converted to the closest d/dy integer value. If this value does not provide the desired null depth, the null depth for a d/λ value returning a d/dy nearest integer next closest to 21 is tested. The plot shows a *primary selection range* consisting of a family of curves. Equation (21) provides a series of d/λ solutions for possible θ values in the range of interest and, as indicated in Fig 19, the solutions form a series of asymptotic curves. The curved portion of the line in Fig 19 represents the actual asymptotic curve solutions converging at an infinite value of d/λ for $\theta = 0$. The vertically oriented straight

29

lines that jump from one curve to the next are plotting anomalies resulting from the solution

attempting to optimize aperture area use.
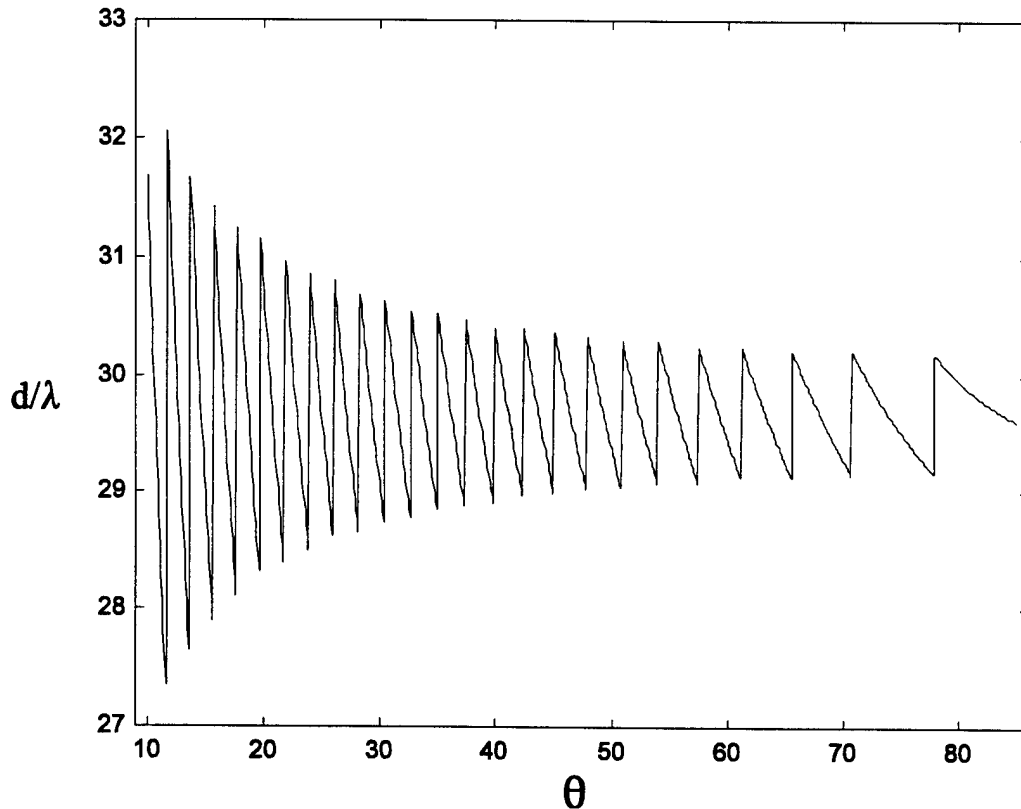
Figure 19: Optimum Phase Center Separation Distance

The next issue addressed is how null location angle θ is determined or estimated.

Two methods are possible. First, using the geometry established in Fig 20, θ may be

estimated using the simple arcsine relationship expressed in Eq (22) where R is the range to

the designated "center" of a given range cell and ϕ is the target depression angle. This

process assumes terrain height variations above the reference ground plane are negligible.

The second method for estimating θ involves the use an on-board digital terrain map. For

this method, terrain height variation above the reference ground plane contributes to the

calculated estimate of θ, as illustrated in Fig 21 and expressed by Eq (23).

30
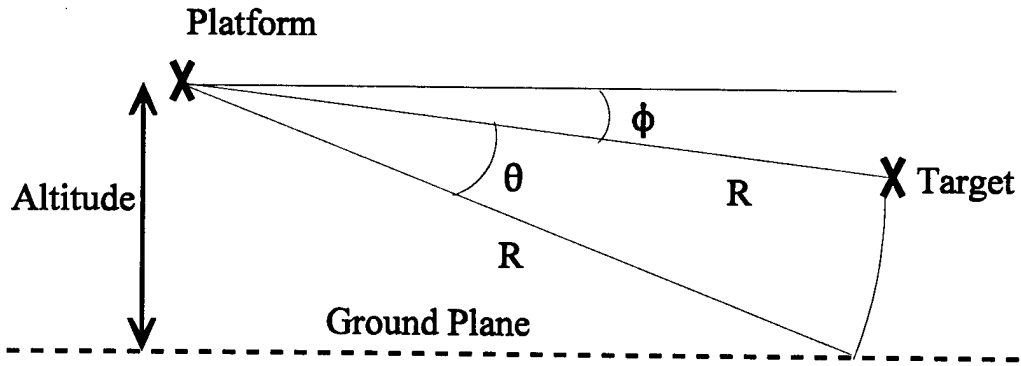
Platform

Figure 20: Depression Angle Calculation Method #1

$$\theta = \text{Arcsin}\left[\frac{\text{Platform Altitude}}{\text{Range (R)}}\right] - \phi \qquad (22)$$
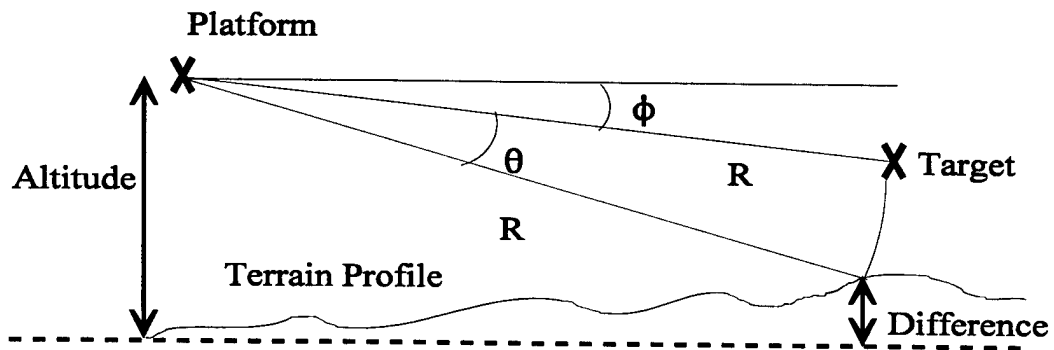
Platform

Figure 21: Depression Angle Calculation Method #2

$$\theta = \text{Arcsin}\left[\frac{\text{Platform Altitude} - \text{Ground Height Difference}}{\text{Range (R)}}\right] - \phi \qquad (23)$$

31

2.4 Generated Null Angular Width and Depth

Generated interferogram nulls differ from natural field pattern nulls existing in normal radar aperture radiation patterns. The interferogram nulls are enforced at specific constant elevation angles in the azimuth/elevation plane antenna pattern and are due to two vertically separated phase centers (versus one for typical air-to-air radar apertures). Each generated null extends across the entire azimuth range of -90 to +90 degrees with their angular positions determined from previously developed equations. By contrast, natural null positions occur as a result of element spacing, amplitude weighting, and aperture dimension and shape, and can be very difficult to predict.

Figures 22 through 32 represent a series of radiation pattern contours at 10 GHz using the APG-63 aperture with 11 different amplitude weighting schemes: the tapered baseline, uniform, and the nine ACE configurations. The vertical and horizontal axes represent elevation and azimuth angles off boresight, respectively. Data is shown for elevation angles up to +10 degrees, placing the main beam near the top of each figure at azimuth and elevation values of 0.0 degrees. This makes the plots easier to view and less redundant since the radiation patterns are symmetrically mirrored about an elevation angle of zero degrees.

Figures 22 and 23 are the radiation patterns for the baseline taper and uniform amplitude cases. In both cases, the patterns exhibit nearly *elliptical* symmetry near boresight. This non-circular symmetry results from the non-uniform element spacing in the horizontal and vertical directions on the APG-63 aperture. Comparison of the figures indicates that the tapered amplitude weighting produces a wider main beam than the uniform case. This is a trade-off for the clutter rejection benefit of lower sidelobe levels, shown later in Fig 40.

32
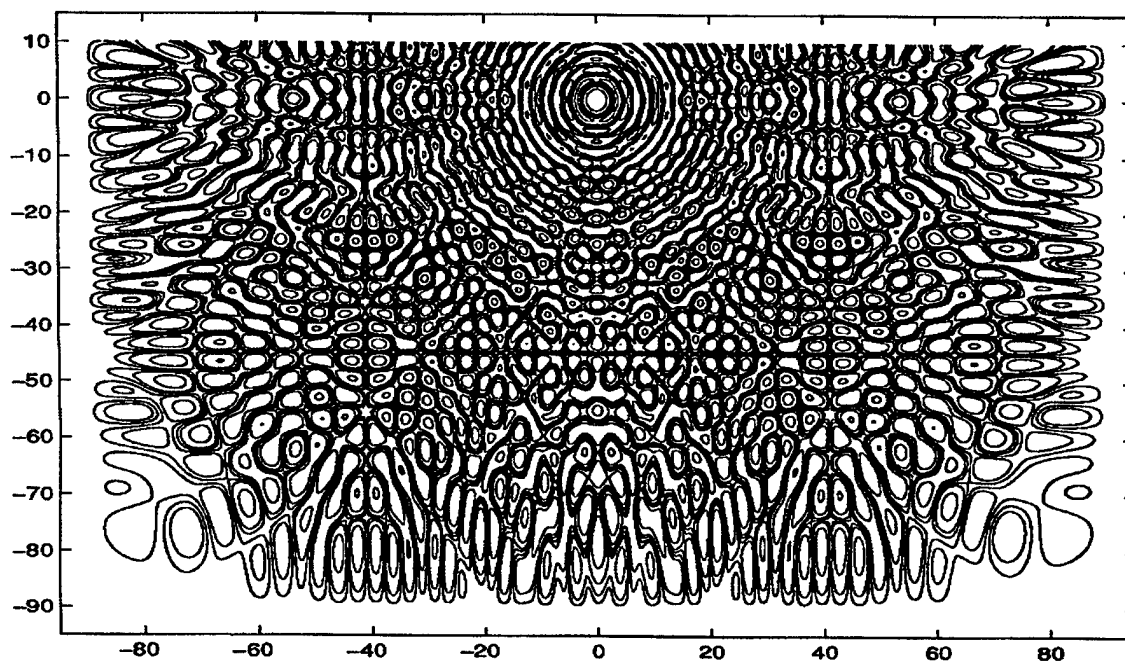
Figure 22: Radiation Pattern for Tapered Amplitude Weighting
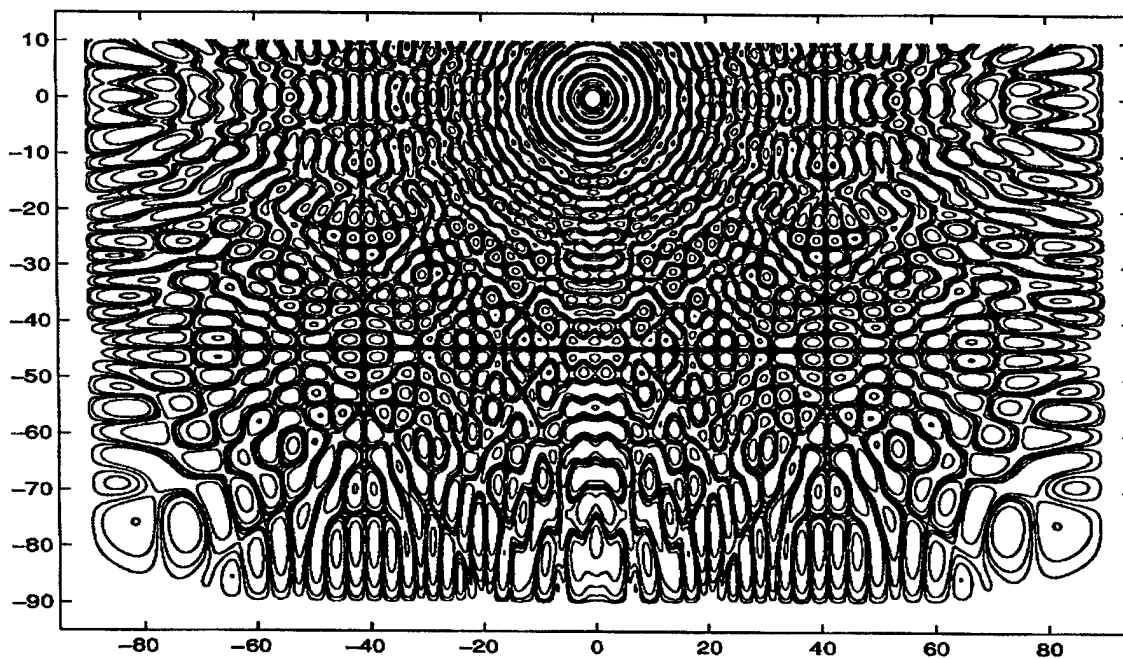
Figure 23: Radiation Pattern for Uniformly Weighted Aperture

Figures 24 through 32 show radiation patterns for the nine ACE configurations. The generated nulls clearly appear as dark constant elevation lines running across the azimuth range, consistent with previous analysis. The object of an ACE system is to map one of these nulls to a given range cell/ground clutter intersection region.

As indicated in the figures, the nine ACE configurations produce a finite number of discretely located nulls from 10 to 85 degrees depression; the ACE configurations are not able to center a null at any arbitrary depression angle. However, as illustrated in Fig 33 and shown by the width of the lines crossing the pattern plots, the nulls do have a non-zero "width" as determined or defined by relative radiation pattern values which fall below neighboring sidelobe levels. Therefore, it is not necessary for an ACE system to "exactly" place a null in the desired direction to achieve performance improvement.
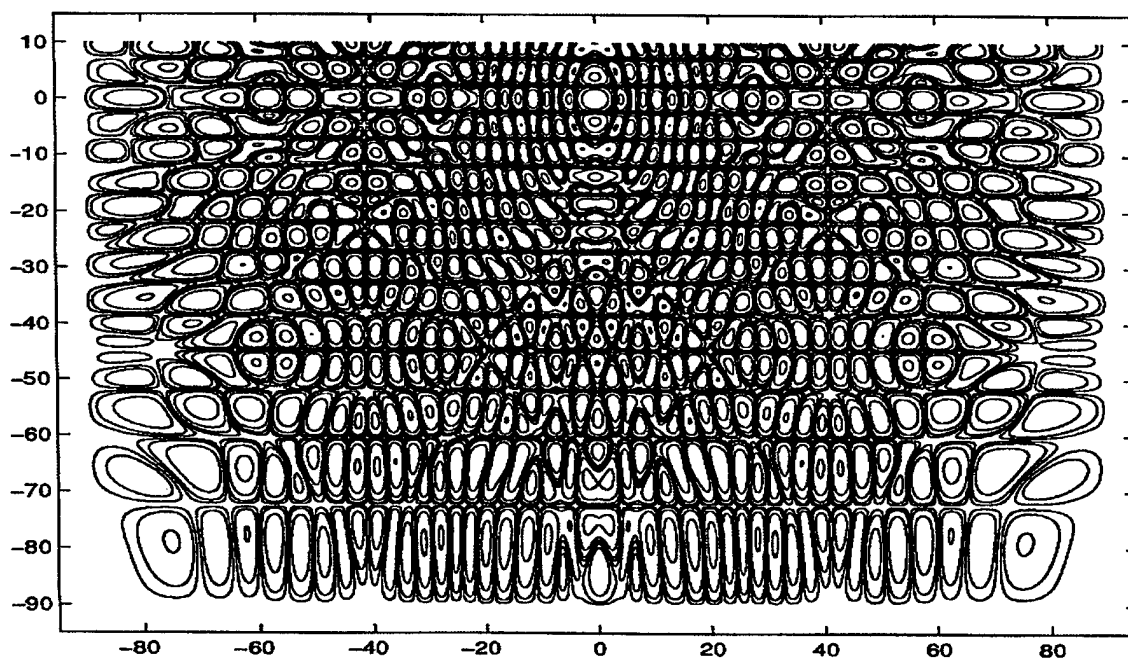
Figure 24: Radiation Pattern for ACE-17 Configuration
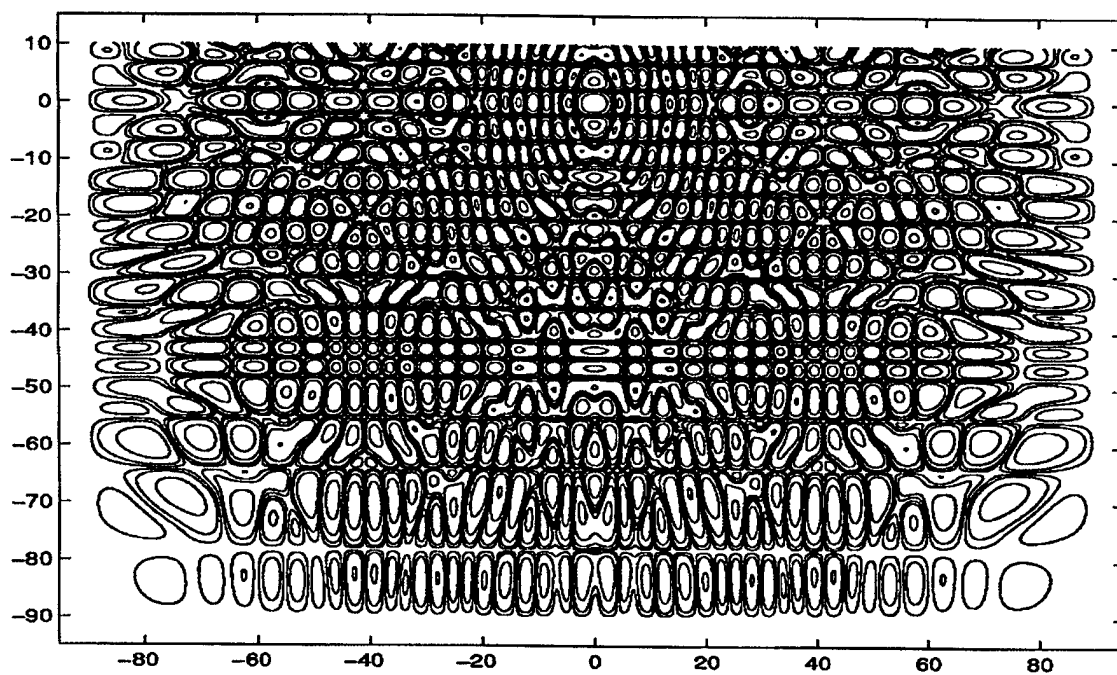
Figure 25: Radiation Pattern for ACE-18 Configuration
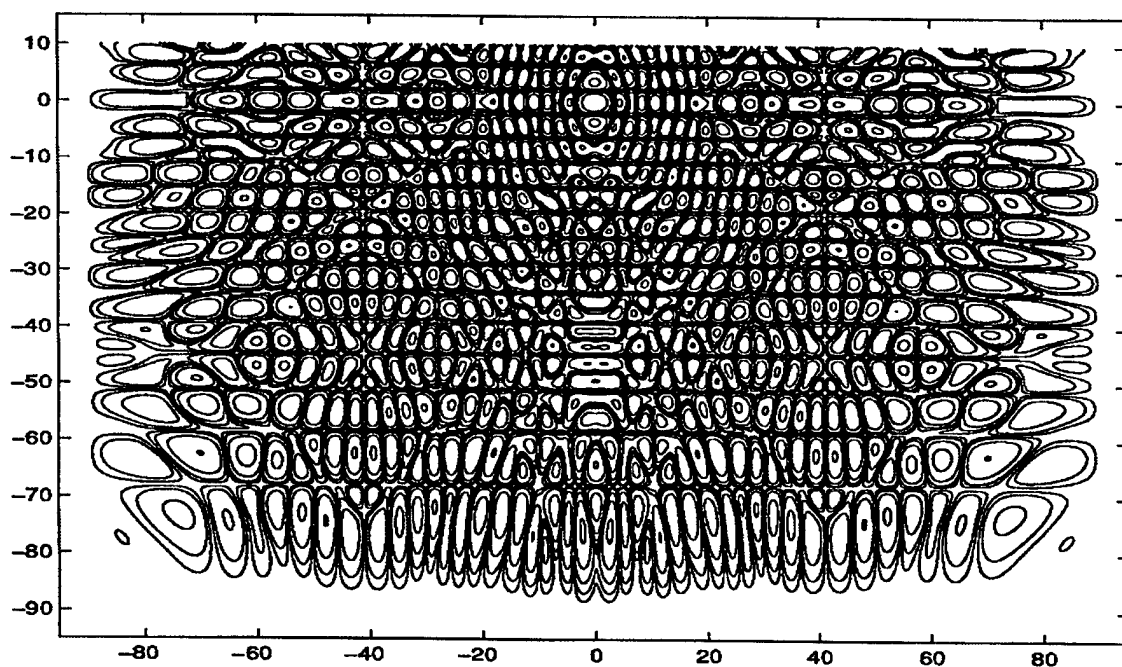
Figure 26: Radiation Pattern for ACE-19 Configuration
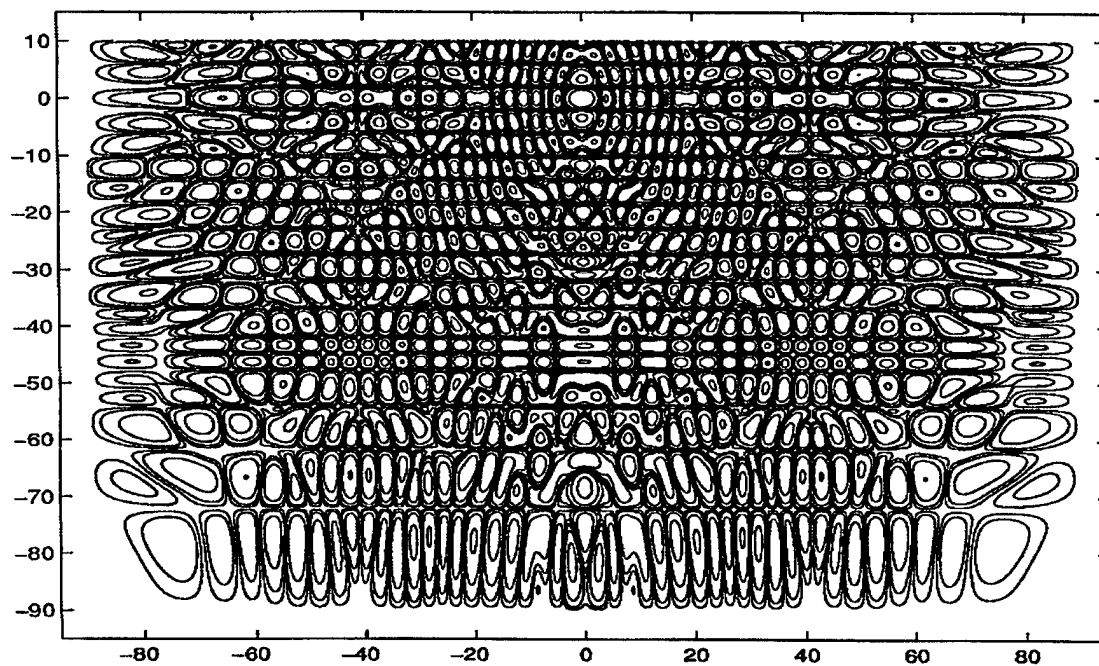
Figure 27: Radiation Pattern for ACE-20 Configuration
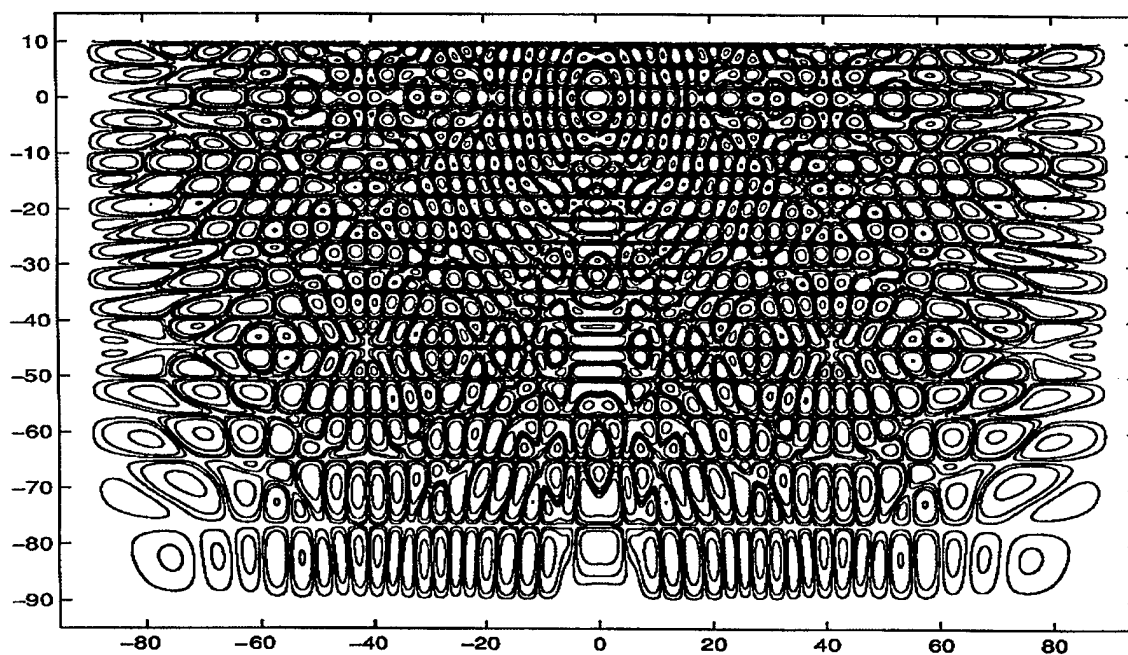
Figure 28: Radiation Pattern for ACE-21 Configuration
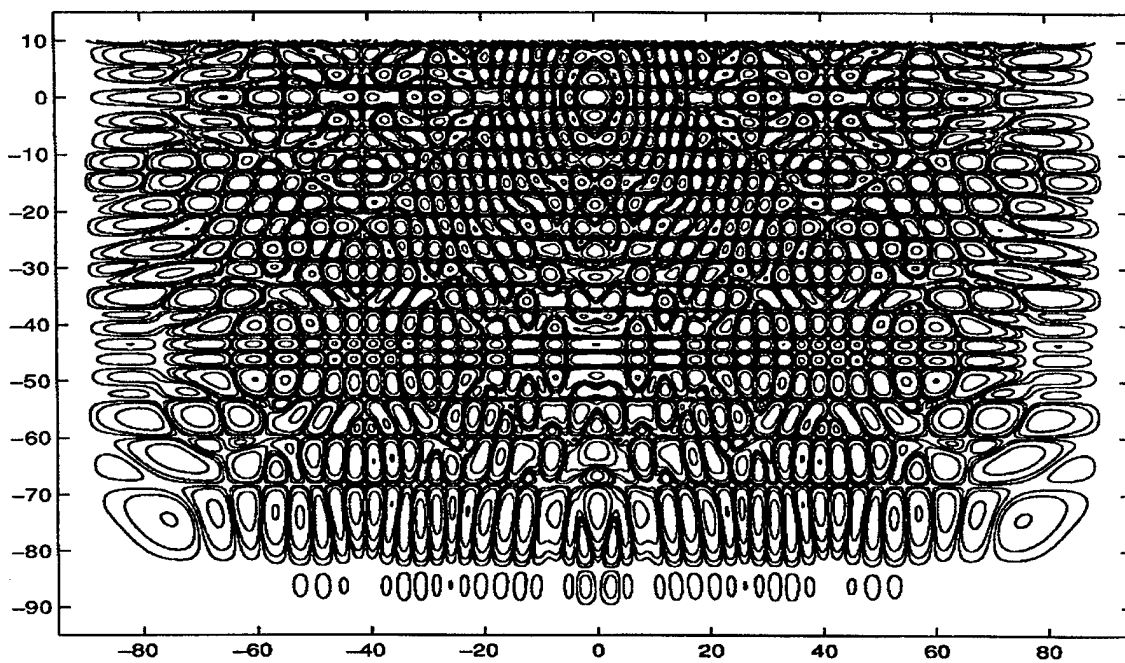
Figure 29: Radiation Pattern for ACE-22 Configuration
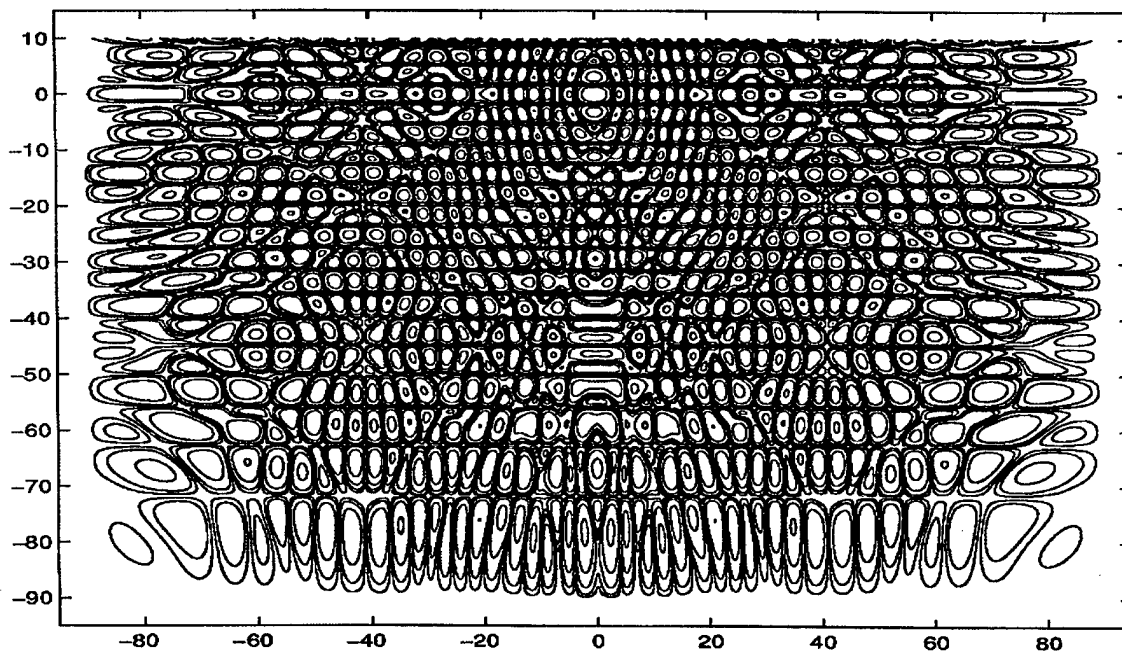
Figure 30: Radiation Pattern for ACE-23 Configuration
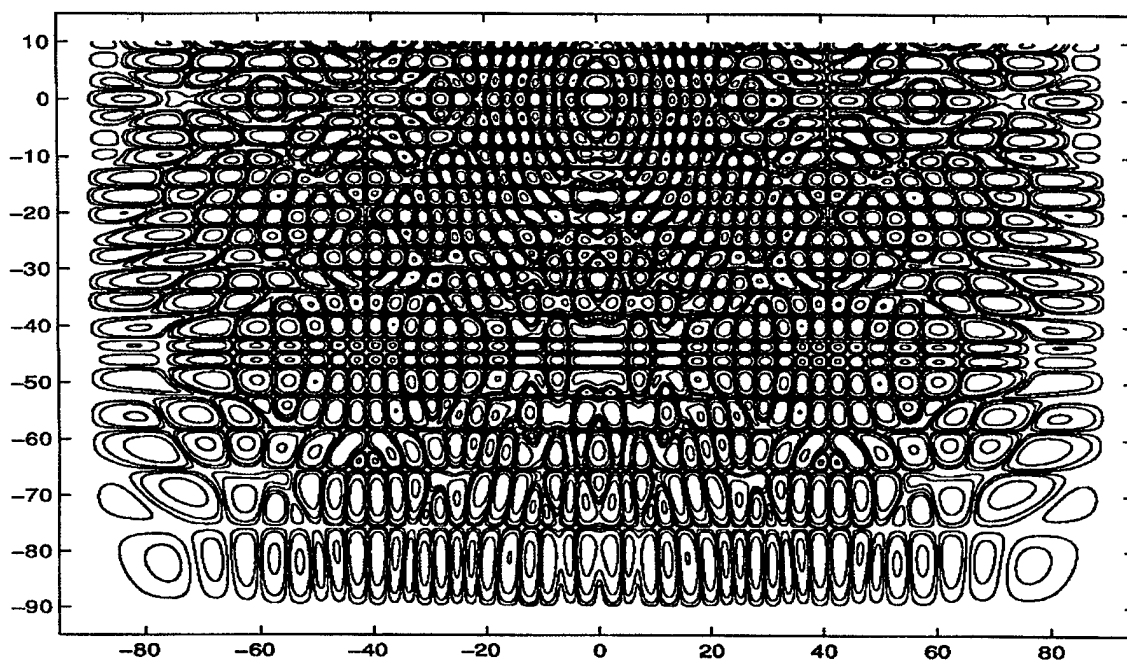
Figure 31: Radiation Pattern for ACE-24 Configuration
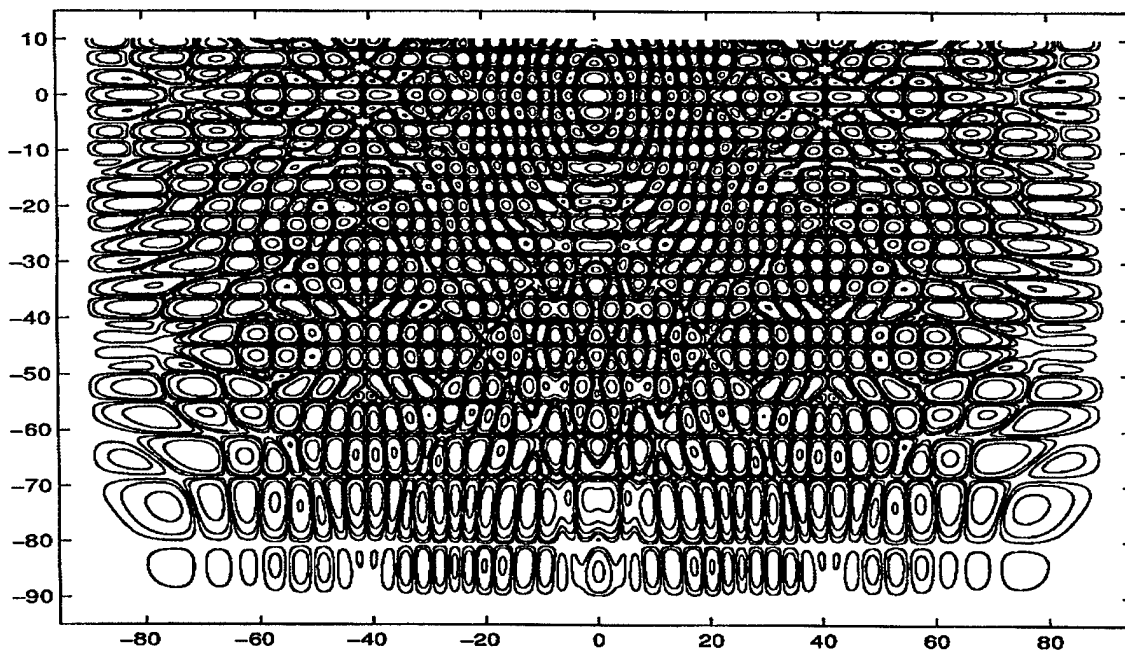
Figure 32: Radiation Pattern for ACE-25 Configuration

38
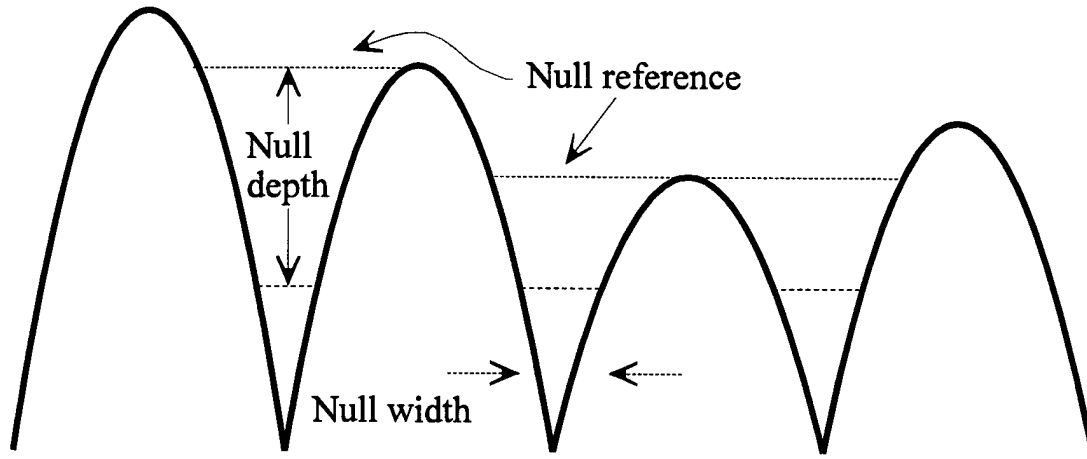
Figure 33: Minimum Depth Definition of Null Width

Because of the inherent antenna lobe phase structure, the configuration selected by the previously introduced algorithm does not necessarily provide the lowest clutter floor. This is because sidelobes on either side of a given null possess odd-phase symmetry, i.e., they are 180 degrees out of phase. It is possible that the nature of the clutter, i.e., the scattering characteristics within a given range cell, can cause the integrated product of ground reflectivity and a non-optimally configured ACE aperture to be closer to zero than an optimally configured ACE system. Essentially, it is possible for the condition shown in Eq (24) to be satisfied where:

$$\int\int F_{Non-Optimum}(\theta,\phi) \cdot RG(\theta,\phi) \cdot \sigma(\theta,\phi) \frac{e^{-jKR(\theta,'\phi)}}{R(\theta,\phi)} d\theta d\phi$$

$$< \int\int F_{ACE\,Optimum}(\theta,\phi) \cdot RG(\theta,\phi) \cdot \sigma(\theta,\phi) \frac{e^{-jKR(\theta,'\phi)}}{R(\theta,\phi)} d\theta d\phi$$

(24)

and $RG(\theta,\phi)$ is the map of the range gate's projection onto the ground, and includes path length differences as a function of azimuth and elevation angle mapping onto the clutter.

Equation (24) provides an alternative method for selecting the ACE aperture configuration: If the target is expected to have a lower return than the ground, *even with ACE*, and ACE is operated with Doppler detection, then the *best* aperture choice is the one with the lowest total received power. This is an anomalous situation which occurs rarely in the ACE simulations.

2.5 Importance of Vertical Stacking of the Phase Centers

The vertically stacked phase center orientation for the ACE system is shown in Fig 34. The left-hand sketch represents normal aperture alignment with the aperture surface normal directed along the negative x-axis. Platform pitch occurs about the y-axis and platform roll occurs about the x-axis, as indicated in the center and right-hand sketches, respectively. As supported by the following results, ACE system performance is much more sensitive to roll angle changes as compared to equivalent changes in pitch angle. It can withstand some degree of variation in pitch angle before clutter suppression performance is degraded, but minimal variations in roll angle before ACE advantage is rapidly destroyed.
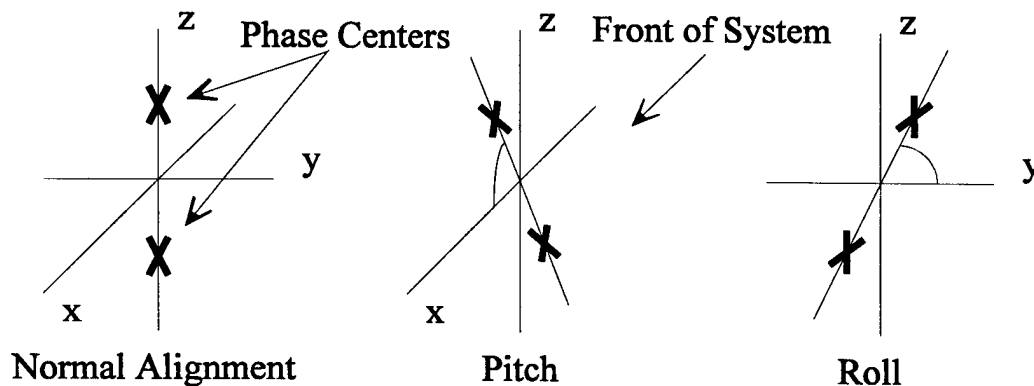
Figure 34: Phase Center Alignment

40

Given an aperture with its surface normal vector parallel to the ground, the rays emanating at a constant depression angle relative to the plane containing the aperture surface normal, intersecting with a perfectly flat ground surface, inscribe a circle centered directly below the radar platform. This same characteristic is exhibited by range borders which also map to circles independently of aperture orientation.

Figures 35 thru 38 represent a series of range cell mappings onto perfectly flat ground. For all cases, the mappings represent the forward projection of a constant depression angle region with an angular width of 3.0 degrees, relative to the normal alignment. All variations between the figures is a result of changing platform characteristics, i.e., pitch and roll variation. Platform characteristics for each figure are as follows:

A) Fig 35: "level" platform, i.e., no pitch or roll

B) Fig 36: 15 degree pitch angle and 0 degree roll angle

C) Fig 37: 0 degree pitch angle and 15 degree roll angle

D) Fig 38: 15 degree pitch angle and 15 degree roll angle
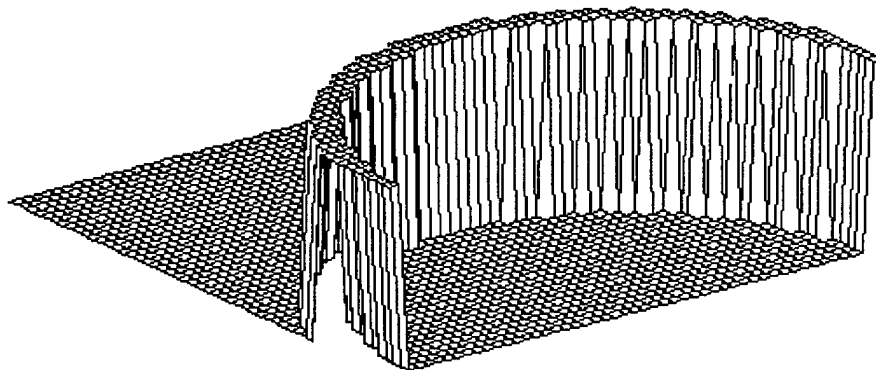
Figure 35: Mapping of Range Cell and Constant Elevation Band for Level Platform
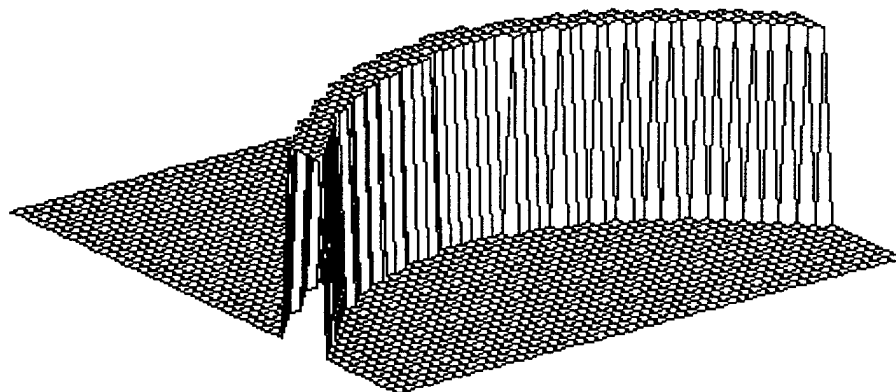
Figure 36: Mapping of Constant Elevation Band for Pitched Aperture
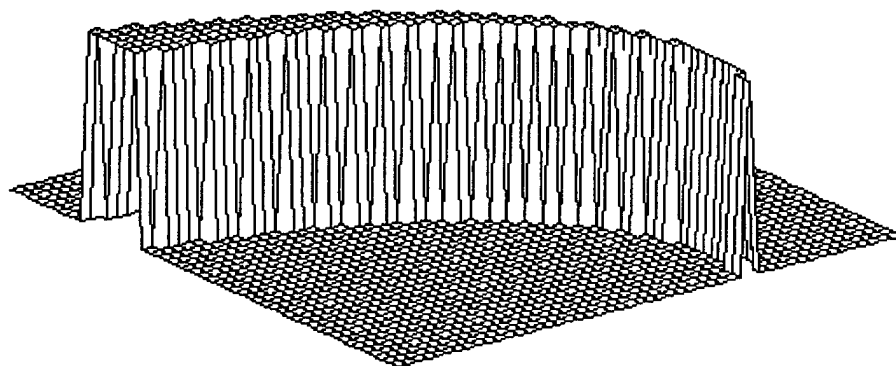
Figure 37: Mapping of Constant Elevation Band for Rolled Aperture
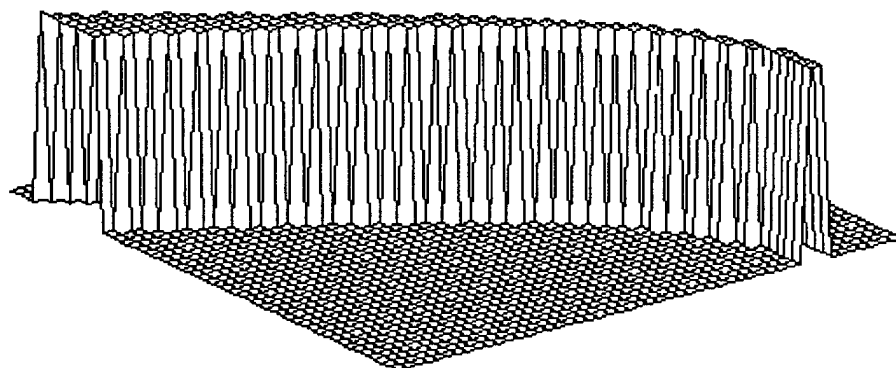
Figure 38: Mapping of Constant Elevation Band for Pitched and Rolled Aperture

Aperture pitch and roll effects, as they relate to ACE's ability to maintain a null within a given range resolution cell, are illustrated in Fig 39. The overlaid (shaded) regions in the figure represent the intersection of a constant elevation depression angle null with a given range cell. The top two plots are for a platform with no roll and pitch angles of 15 and 35 degrees, left and right plot respectively. The bottom left-hand plot is for platform with a 15 degree roll angle and no pitch. The bottom right-hand plot is for a platform with 15 degree roll and 15 degree pitch angles. As indicated in Fig 39, changes in platform pitch angle do not affect ACE performance nearly as much as equivalent roll angle changes. The waves in the lines are the result of ground pixel spacing.
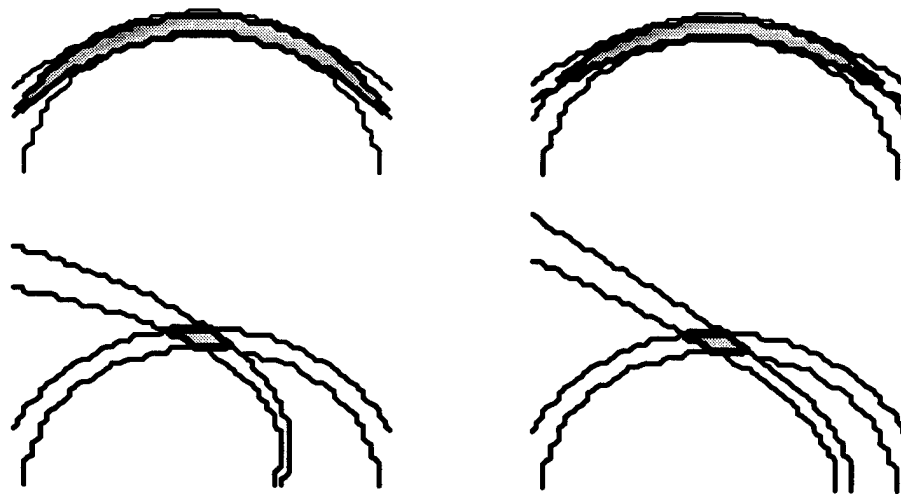
Figure 39: Range Cell vs. Constant Elevation Bands for Various Aperture Attitudes

The importance of eliminating platform roll effects from an ACE system can be illustrated by comparing antenna sidelobe structure. The APG-63 aperture with the baseline amplitude taper is specifically tailored to produce low sidelobe levels in both azimuth and elevation planes. The nine ACE configurations are less than optimal, generally having higher

43

sidelobe levels in both azimuth and elevation when compared with the baseline tapered system. ACE's ability to intelligently manage sidelobe characteristics by selecting a configuration that has the lowest sidelobe levels *mapped to the ground in a specific range cell*, is defeated when a constant angle elevation null cannot be mapped to the ground. Under such conditions, a lower sidelobe aperture is expected to outperform all ACE configurations.

Centerline azimuth and elevation plane radiation patterns are plotted in Fig 40 as a function of angle off boresight for the uniform, baseline taper, and ACE-21 aperture weightings. The uniformly weighted pattern is shown in a sparsely dotted line, the tapered pattern with a dashed line, and the ACE-21 pattern in a solid line.
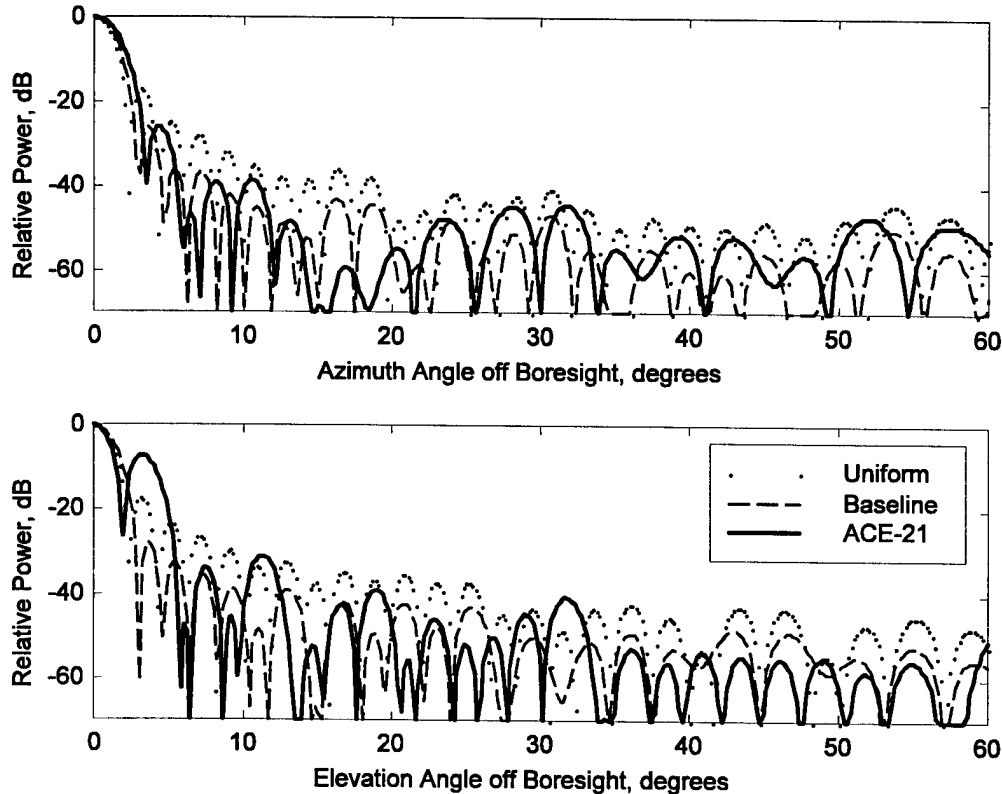
Figure 40: Azimuth and Elevation Plane Radiation Patterns

44

2.6 Clutter Height Variation: Airborne Platform Perspective

A 3-D region of ground clutter transforms to a 2-D azimuth-elevation angle space as viewed from the platform. The physical length and width of the region, as well as ground height variations within the region, contribute to the overall extent of the azimuth-elevation space produced by the transformation. Figure 41 shows the elevation angle mapping of a section of flat ground from the perspective of an airborne platform. Likewise, Fig 42 shows the elevation angle mapping for a section of ground with a specific height profile. Under a worst case scenario, i.e., maximum elevation angle extent, the terrain height is at its lowest altitude near the front of the range cell and at its highest altitude near the back of the range cell, the case shown in Fig 42. In Figs 41 and 42, RG is the physical length of the range gate, θ is the elevation depression angle to the near edge of the range cell, and ϕ is the extent of elevation angle, i.e., the angular region mapped by the intersection of the range gate with a given range cell. Given RG is equal for both cases, it is clear from these figures how the terrain height variations within a given range cell affect the elevation angle extent.
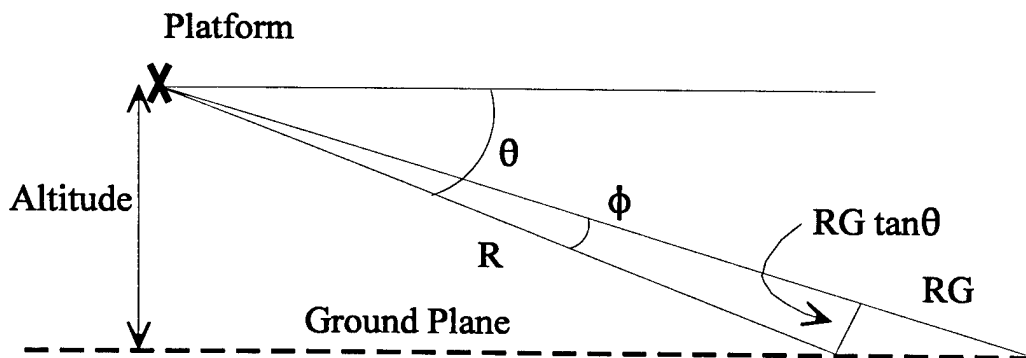
Figure 41: Elevation Angle Extent for Flat Ground

For the flat ground geometry established in Fig 41, the elevation angle extent, ϕ, can be estimated using Eq (25) assuming there is no platform roll, $R \gg RG$, and the elevation depression angle, θ, is fairly small.

$$\phi = \arcsin\left(\frac{RG \tan\theta}{R} \right) \qquad (25)$$
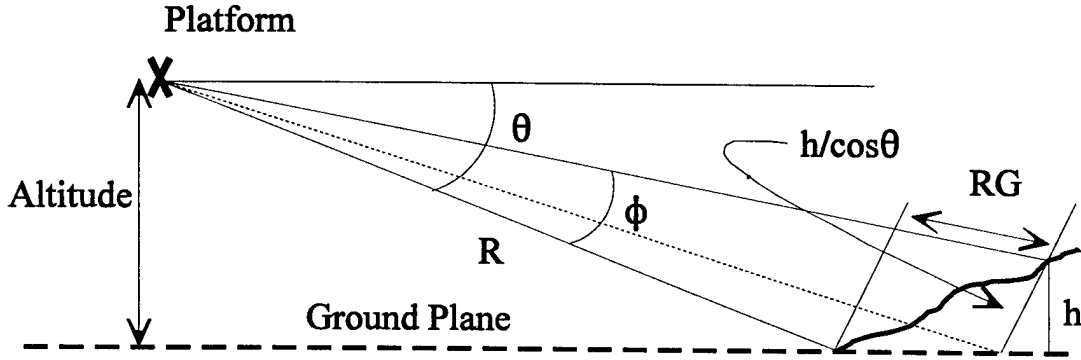
Figure 42: Elevation Angle Extent for Worst Case Ground Profile

Using the profiled ground geometry established in Fig 42 where h is the height difference between the ground at the back and front of the range cell, the same assumptions used in the flat ground case result in the elevation angle extent expression given by Eq (26). This expression reduces to Eq (25) for $h = 0$ which is equivalent to flat ground conditions.

$$\phi = \arcsin\left(\frac{RG \tan\theta}{R} \right) + \arcsin\left(\frac{h}{\cos\theta} \right) \qquad (26)$$

2.7 Clutter Roughness Classification

Since SCR is as a function of terrain roughness, as discussed in Section 2.2, a method for quantifying roughness is needed. Several possibilities were investigated with two

46

emerging as being applicable to ACE performance analysis. Two different roughness indices (RI) were developed for use under slightly different circumstances. The first index, RI_1, as given by Eq (27), is a "global" index taking into account the standard deviation of absolute terrain height over the entire cell of N pixels. The second index, RI_2, as given by Eq (28), is a "local" index taking into account the standard deviation of relative terrain height differences between adjacent pixels within a given cell. Both indices are for N >> 1 such that N ≈ N - 1.

$$RI_1 = \sqrt{\frac{1}{N-1} \sum_{i=1}^{N} \left(x_i - \overline{x_i} \right)^2} \tag{27}$$

$$RI_2 = \sqrt{\frac{1}{N-1} \sum_{i=1}^{N} \left((x_i - x_{i-1}) - \overline{(x_i - x_{i-1})} \right)^2} \tag{28}$$

As defined, both RI characterizations have limitations. The global RI_1 index is relatively insensitive to the difference between level rough terrain and constantly sloped smooth terrain. The local RI_2 index is dependent on pixel spacing and may return different index values for North/South (N/S) as compared with East/West (E/W) differences and also NW/SE and NE/SW diagonal differences. Figure 43 illustrates the potential problem associated with global index RI_1. Assuming each of the curves represent terrain height as a function position, it is visually apparent that the top curve represents drastically "rougher" terrain than does the lower curve. Alternately, we can characterize the top curve as rough terrain with minimal slope and the lower curve as smooth terrain with appreciable sloped.

47

Application of Eq (27) reveals that data for both curves produces an identical RI_1 value of approximately 2.8. Clearly, the RI_1 index is not a good discriminant for this case. Using the same data and Eq (28), produces an RI_2 index value of approximately 0.4 and 0.01 for the upper and lower curves, respectively. Therefore, the RI_2 index is a better index to use to characterize the terrain for this case.
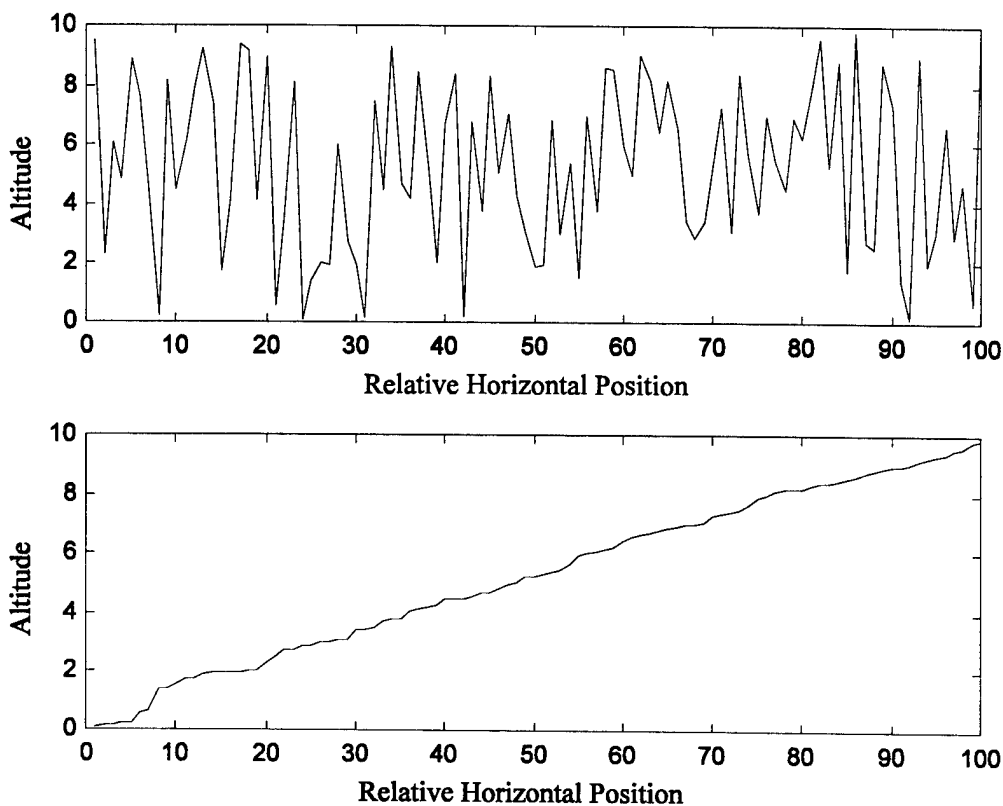
Figure 43: Roughness Index Performance Comparison

The global RI_1 index is used to characterize terrain roughness for ACE performance evaluation. As indicated in Section 2.6, the extent of the antenna pattern angular region mapped to the ground, as determined by the height characteristics within a range cell, determine the amount of clutter that affects ACE performance. As Fig 43 shows, the two

48

drastically different terrain characteristics, rough/level and smooth/sloped, produce the same

relative height variation which results in the same antenna pattern angular extent - equivalent

RI_1 values have mapped to equivalent angular extent. Therefore, the global RI_1 index is a

good metric for characterizing the angular extent over which the ACE system must perform,

a higher global RI_1 index value implies a greater angular extent.

The local RI_2 index is used to characterize and predict terrain interpolation reliability.

For the modified cubic spline interpolation process introduced in Chapter 5, simple ground

slope has minimal impact on interpolation reliability. The upper and lower curves in Fig 44

represent rough terrain with moderate slope and smooth terrain with minimal slope,

respectively; RI_2 is greater for the upper curve than it is for the lower curve. As indicated by
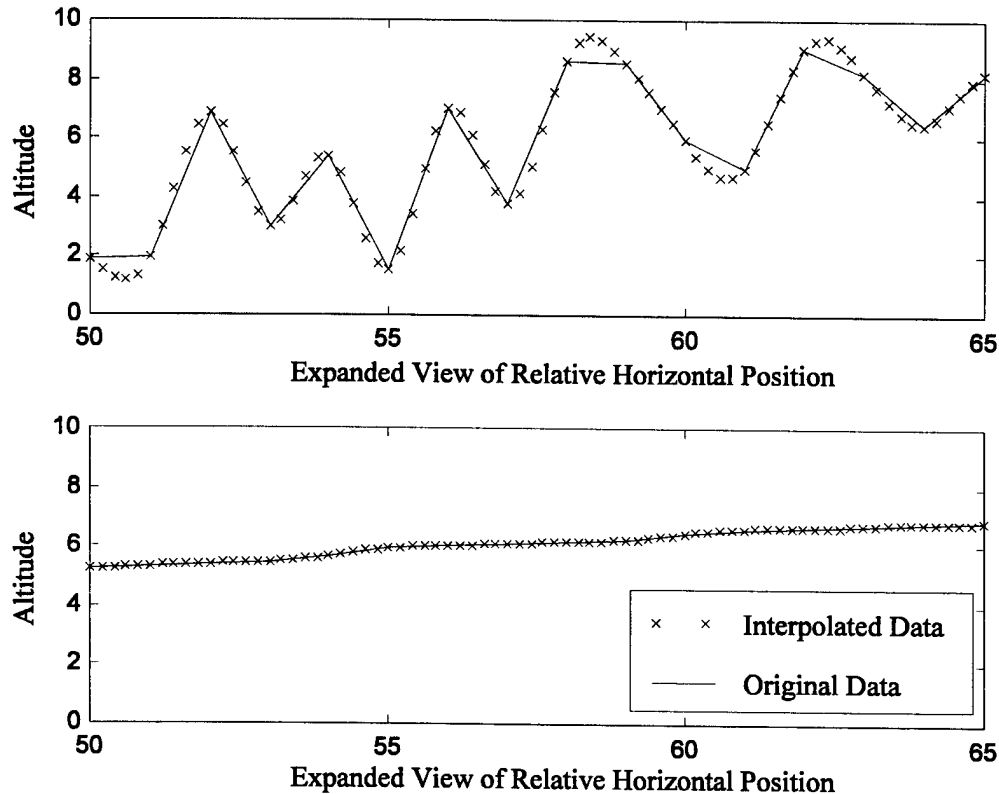
Figure 44: Interpolation Issue for Roughness Index

49

the interpolated "x" values, the terrain with a relatively constant slope is interpolated to a high degree of accuracy and terrain with rapidly changing slope is not as accurately interpolated. Clearly, the absolute maximum height differences within the overall region affect interpolation accuracy less than do relative height differences between adjacent pixels. Given the RI_2 index value reflects local terrain variation phenomena, it is the metric of choice for determining how well the terrain interpolation process works for a given terrain region, a lower RI_2 index value indicates better interpolation results.

3. ACE Digital Model Design

To test and predict the clutter power suppression capability of an ACE system, relative to a radar system with a fixed non-adaptive aperture, model development and subsequent simulation scenarios are based on incorporating or duplicating as many real world effects as possible, including, ground clutter reflection effects and ACE system response. Since a reliable 3-D ground clutter model was not available, one was developed to permit initial examination of the ACE concept and performance estimation.

3.1 Model Philosophy

An electromagnetic ray trace propagation technique is used to model radiation characteristics for both the incident and reflected energy from the ground. Ray position is determined by assigning one ray to each ground "pixel" location where a pixel represents a single point on a given section of ground. At each pixel location, the ground elevation, slope, and backscatter properties for the region it represents are modeled as accurately as possible. All rays emanating from pixels within the modeled radar system's range gate include amplitude and phase information resulting from range variation to the pixel and the terrain backscatter coefficient at the pixel location. Rays incident on the aperture are weighted by complex transmit and receive field pattern values. The assigned weighting values are based on the relationship between ray arrival and aperture surface normal directions. All rays from pixels within a given range gate are coherently summed, not just those that fall within the main bean or the first few sidelobes.

This model provides ground clutter return estimates free from limiting assumptions typically imposed by existing analytic methods. Typical assumptions include: 1) constant mean ground height, 2) constant backscatter properties, 3) constant surface roughness, 4) constant mean ground slope, and 5) separable and/or idealized aperture radiation patterns for the entire illuminated region [11, 12]. For this model, these assumptions are only applied *locally* to the region of ground represented at a single pixel location within the illuminated region. With relatively tight pixel spacing, terrain features such as shorelines, ridgelines, mountains, deep gorges, and abrupt changes in vegetation cover are adequately described.

Ground height variation within a range cell is very important because it directly affects the angular region occupied by clutter. Ground slope is included because it affects the general behavior of the reflection coefficient [13]. Specifiable terrain type, assignable on a pixel-by-pixel basis, allows for combinations of varying backscatter coefficient behaviors within a single illuminated clutter scene.

For ACE system performance characterization, the digital model assumes the aperture is tracking a target in range unambiguous mode. Range ambiguity effects are discussed later and are not the central focus of initial ACE performance evaluation. The ACE system model only includes the *"up-front"* portion of the system, i.e., the aperture itself. Beyond aperture input/output voltage formulation, there is no signal processing modeled. As presently designed and implemented, the model allows for other performance enhancement techniques, i.e., signal processing techniques such as Doppler detection, DBS, and SAR, to be implemented within the confines of the current architecture. This research effort examines

clutter rejection and suppression potential for an ACE equipped system *prior* to integration of these existing target detection enhancement techniques.

3.2 Model Capability and Flexibility Goals

The two main goals for this model are *reliability* and *flexibility*. The reliability goal is met by providing accurate and complete terrain sub-level models for the overall 3-D ground reflectivity model. Figure 45 shows the multi-layer matrix that makes up the 3-D ground model concept where a single pixel description contains all relevant information. The backscatter coefficient for any pixel is the result of contributions from all layers.

Altitude
Northward and Westward Slope
Terrain Type
Surface "Thickness"
Reflectivity Coefficient (Probabilistic)
Shadowing Effect
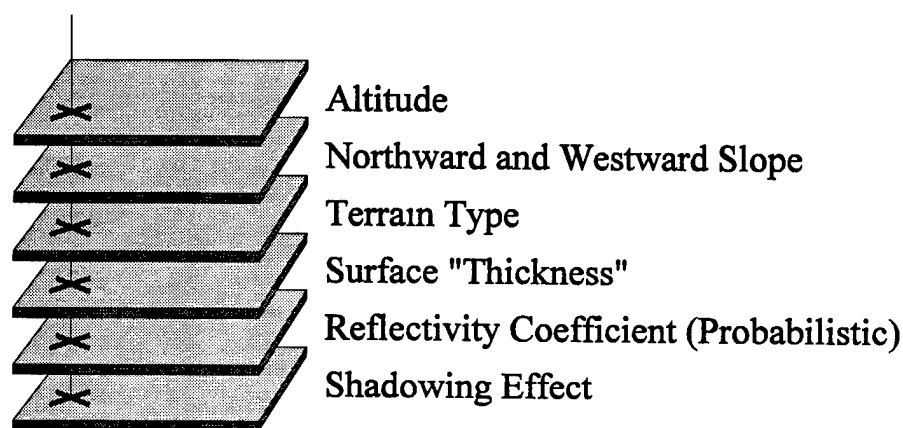
Figure 45: 3-D Clutter Reflectivity Model

A large clutter "scene" is formed using this multi-layer matrix where the entire subset of pixel backscatter coefficients are calculated within a range cell for a given *observation*. Altitude information is used for calculating the elevation angle of the pixel as viewed by the aperture and combined with the localized slope, allows calculation of the angle of incidence of the illumination with the ground. This angle of incidence along with the terrain type

53

specified for that pixel are fed into the backscatter coefficient generator. Surface "thickness" varies as a function of terrain type and corresponds to clutter height differences between the terrain altitude and the earth's crust at the pixel location. For example, trees, large rocks, and man-made objects covering otherwise flat ground do not represent a level clutter height. Given that real terrain exhibits probabilistic reflectivity behavior, the reflectivity coefficient layer of the model reflects the possibility that a given pixel is either "loud" or "quiet" for its specified terrain type and ray incidence angle. Finally, the last layer of the model accounts for rudimentary shadowing effects which are based on ray incidence angles relative to the surface normal greater than 90 degrees and are easily incorporated into the model.

To provide maximum flexibility, the complete digital ACE model incorporates both the 3-D clutter reflectivity effects and ACE operating characteristics with easily changed parameter sets. The complete ACE digital simulation concept is illustrated in Fig 46 where each modeled parameter set is represented by a drawer in a filing cabinet.

All model parameters, i.e., "drawer contents," can be independently changed by simply substituting in a new data file containing new parametric information, no program code changes are required. For example, trees are easily made "taller" or "shorter" by simply substituting in larger or smaller numbers in the "Thickness" drawer. Actual flying aircraft scenarios are easily generated by providing appropriate Target RCS values and ensuring the data in the Target Position & Motion drawers reflects realistic flight characteristics. Simulated scenarios are easily run over "realistic terrain" at any place on the earth by introducing appropriate altitude, slope, and terrain type information. Critical assumptions

54

and conditions required for comparison with analytic predictions are easily satisfied. A detailed discussion of each drawer's "contents" is provided in later sections.
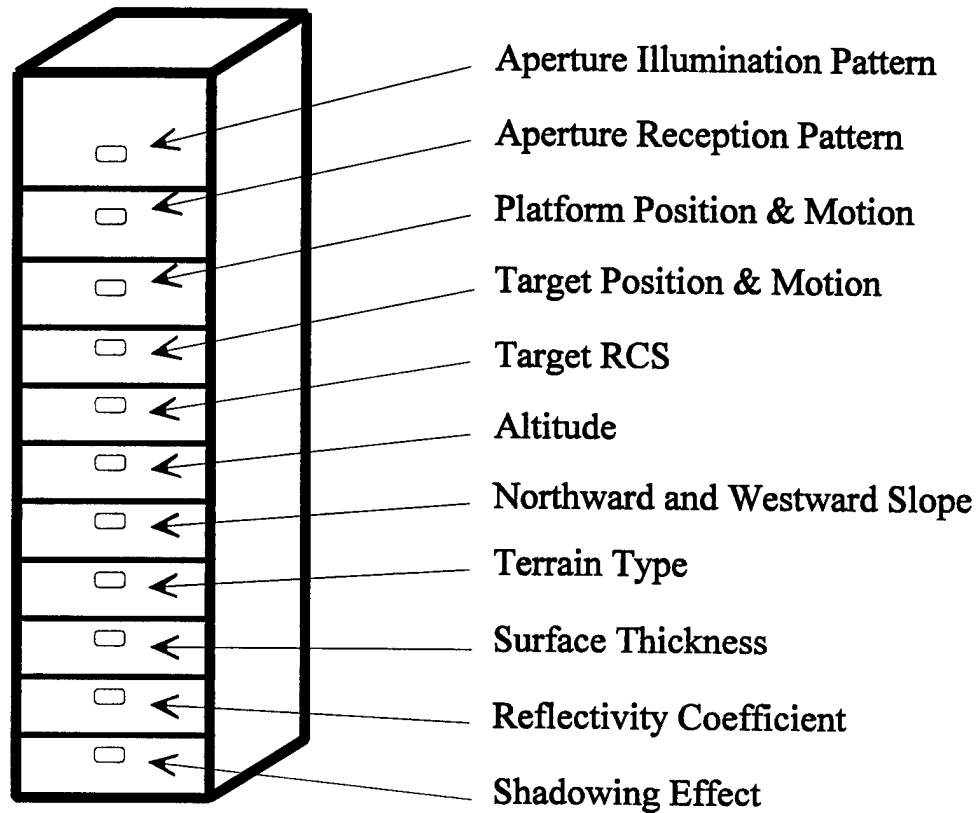
Figure 46: Digital ACE Model Representation

3.3 Platform Articulation and Coordinate Transforms

The model is fully implemented using four distinct coordinate systems. The first three coordinate systems are shown in Figs 47 and 48. The systems are the 1) Global System: a global Cartesian coordinate system referenced to a specific latitude and longitude point with its origin located the most south-western point, 2) Azimuth, Elevation, and Range #1 (AER-1): a coordinate system with its origin on the platform, azimuth reference

unit vector, $\hat{a}_1$, and elevation reference unit vector, $\hat{e}_1$, determined by the range unit vector,

$\hat{r}$, pointing from the platform toward the target and $\hat{z}$ from the Global system, 3) Azimuth,

Elevation and Range #2 (AER-2): same origin location as AER-1 but with $\hat{a}_2$ and $\hat{e}_2$ tilted

to reflect platform roll, and, 4) Azimuth, Elevation and Range #3 (AER-3): a coordinate

system with its origin centered on the target and azimuth and elevation angles defined as the

angles from which the target is observed, including target roll.
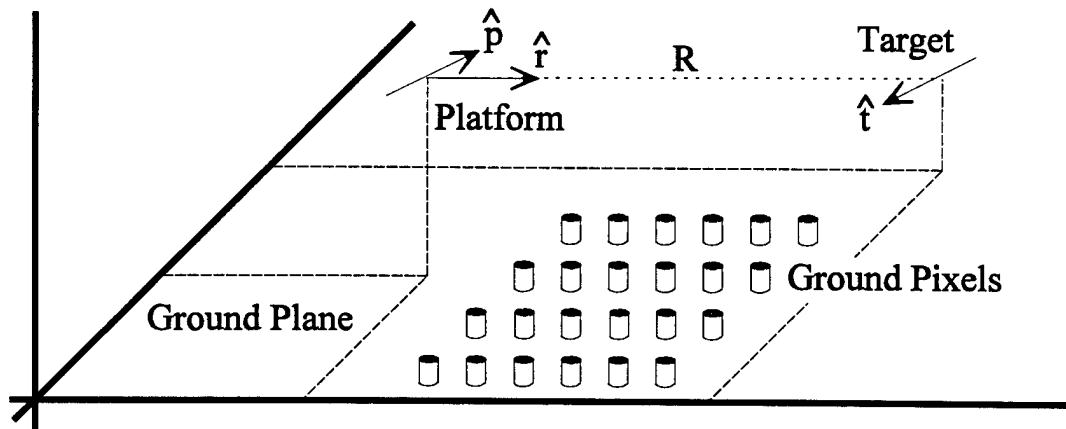
Figure 47: Global Coordinate System

The Global coordinate system is used to define the absolute location and slope of

each ground pixel in the scene. Platform and target position/orientation (directions of travel)

are also initially reported in this system. For every reported target or platform position, the

model requires eight pieces of information: x, y, z position coordinates, the x, y, z

components of the unit orientation vector (either $\hat{p}$ for platform or $\hat{t}$ for target), platform or

target roll angle, and speed along the direction of either $\hat{p}$ or $\hat{t}$.

The platform and target orientation vectors of Fig 47, $\hat{p}$ and $\hat{t}$ respectively, are input

into the model via flight profile information which resides in the Position & Motion

56

"drawers" of the simulation. Range parameters, magnitude R and direction vector $\hat{r}$, are determined per Eqs (29) and (30) where subscripts t and p denote target and platform position coordinates in the global system.

$$R = \sqrt{\left(x_t - x_p\right)^2 + \left(y_t - y_p\right)^2 + \left(z_t - z_p\right)^2} \tag{29}$$

$$\hat{r} = \frac{\left(x_t - x_p\right)}{R}\hat{x} + \frac{\left(y_t - y_p\right)}{R}\hat{y} + \frac{\left(z_t - z_p\right)}{R}\hat{z} \tag{30}$$

The AER-1 coordinate system is used to simulate ACE performance in tracking rather than search mode. In this case, the aperture is "scanned" in such a way that the target appears on the mechanical boresight of the aperture. Unit directional vectors $\hat{a}_1$ and $\hat{e}_1$ define azimuth and elevation target location angles as viewed from the aperture and are found from Eq (31). Platform roll translates to effective aperture roll in the AER-2 coordinate system via Eqs (32) and (33), where subscripts reference the specific AER system..
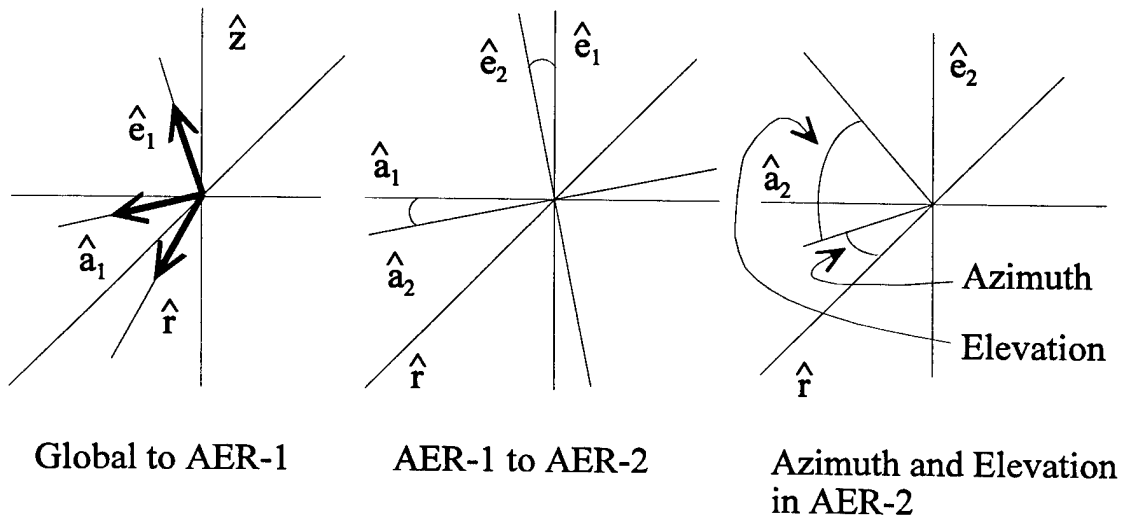
Figure 48: Coordinate Transforms

Global to AER-1   AER-1 to AER-2   Azimuth and Elevation
                                                 in AER-2

57

$$\hat{a}_1 = \frac{\hat{r} \times \hat{z}}{|\hat{r} \times \hat{z}|} \quad ; \quad \hat{e}_1 = \frac{\hat{a}_1 \times \hat{r}}{|\hat{a}_1 \times \hat{r}|} \tag{31}$$

$$\text{Effective Aperture Roll} = (\hat{p} \cdot \hat{r})(\text{Platform Roll}) \tag{32}$$

$$\hat{e}_1 \cdot \hat{e}_2 = \hat{a}_1 \cdot \hat{a}_2 = \cos\left[(\hat{p} \cdot \hat{r})(\text{Platform Roll})\right] \tag{33}$$

Since the target is centered on mechanical boresight, the azimuth and elevation coordinates are used to describe the position of the clutter as viewed from the aperture. In the AER-2 system the azimuth plane is defined as the plane containing both $\hat{a}_2$ and $\hat{r}$ with the clutter azimuth location angle defined as the angle between $\hat{r}$ and the projection of a vector pointing to a given clutter pixel onto the azimuth plane. The elevation plane is defined similarly as the plane containing both $\hat{e}_2$ and $\hat{r}$ with the clutter elevation location angle defined as the angle between $\hat{r}$ and the projection of a vector pointing to the same clutter pixel onto the elevation plane.

3.4 Pixel Spacing Requirements for Ray Trace Reliability

To properly characterize a continuous scene of clutter with a ray trace propagation technique, two parameters are examined to establish minimum pixel spacing requirements, *regularity* and *granularity*. Pixel position regularity addresses constant interval spacing (in some units) within the coordinate system while granularity deals with the maximum allowable number of units within the interval. To provide proper scaling for backscatter

coefficient calculation and subsequent comparisons, the pixel spacing must be regular in the same units for which the coefficients are measured and reported. In this case, normalized measured coefficients with units of square meters are used for comparison and validation. This establishes the Global coordinate system as the system of choice for location regularity.

The granularity requirement ensures that pixels are spaced *closely enough* to ensure the model accurately reflects real world conditions for each scenario considered. The question is, "How do we determine the maximum distance between pixels and in what coordinate system do we define this distance?" Since the aperture response to incoming signals (rays) is found via aperture field pattern multiplication and not by phase weighted summation over the 1368 aperture elements, the minimum ray density is examined in terms of angular separation between rays. For convenience the AER-1 coordinate system is used.

The digital model uses sampled aperture field pattern values for all 11 aperture configurations, i.e., the nine ACE, baseline tapered, and uniformly weighted aperture configurations. The aperture field patterns are sampled at 0.2 degree increments in azimuth and elevation. As expected, most rays incident on the aperture do not arrive from directions that exactly align with sampled field pattern locations. In this case, the field pattern value assigned to the ray is determined by interpolating the four field pattern values that have location angles most closely aligned with the received ray. With an appropriate ray density factor, the ray trace method provides results consistent with a continuous clutter scene integrated over a continuous aperture field pattern. However, when the ray density factor is not sufficient, the ray trace method does not provide enough intersection points with the sampled field pattern and the aperture's response is not accurately represented.

Since the aperture field pattern is essentially a Fourier Transform of the amplitude weighting, the following test is proposed to determine the ray density factor: 1) decimate the sampled field pattern by some factor, 2) take the Fourier Transform of the decimated field pattern, and, 3) interpolate to the original sample density with a zero-padded inverse Fourier Transform. As the decimation factor increases, the interpolated field pattern sets begin to diverge from the original data set. The decimation factor producing the least acceptable re-creation of the original aperture field pattern determines the minimum acceptable angular resolution and in turn sets the maximum pixel spacing distance. Degradation of the re-created field pattern from an increasingly decimated data set is a gradual process, so the threshold chosen for minimum density was a purely qualitative choice. The theory behind this approach is that as long as the decimated aperture field pattern contains enough information to reproduce the sidelobe structure with FFT interpolation, the aperture response is accurately reflected by ray intersections at that particular density. When the Fourier Transform interpolation procedure can no longer distinguish between sidelobes, the modeled response of the aperture becomes unreliable at a corresponding ray density.

Figure 49 illustrates the effects of the decimation and interpolation test process for a section of the field pattern using a uniformly illuminated aperture. Plots are shown for the original field pattern data and field pattern data for decimation factors (thinning ratios) of two, four, and five. Similar results are obtained for the ACE and baseline tapered aperture configurations. Based on the results, a decimation factor of four seems to provide a lower bound for sample density. For this density factor, one sample per 0.8 degrees, the Fourier Transform interpolation method barely reproduces noticeable sidelobe structure.
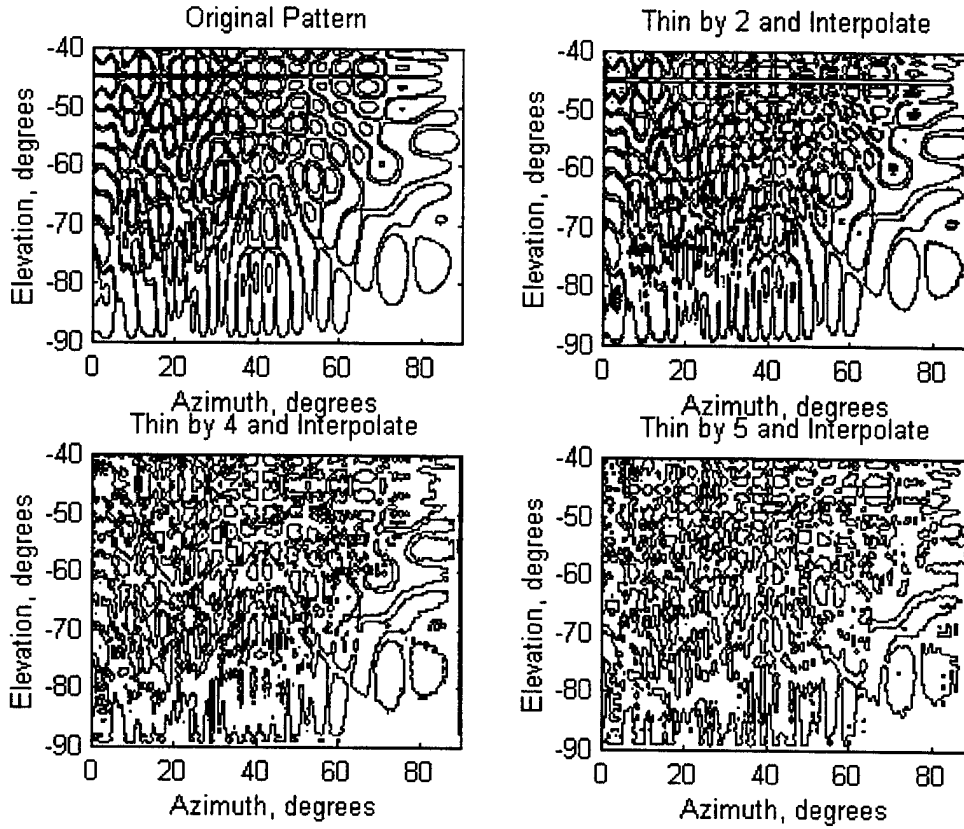
Figure 49: Test for Minimum Required Angular Resolution

Figure 50 shows the relationship between the maximum angular separation distance between rays, Δ, and the minimum pixel separation distance, d. The relationship between Δ and d is given by Eq (34) where θ is the pixel depression angle which equals the angle of incidence between a ray parallel to R and the ground plane surface normal vector. For small Δ, the small argument approximation of $sin(x) = x$ may be used to express d in terms of Δ, θ, and R as given by Eq (35). Assuming an angular resolution of 0.8 degrees ($\Delta = 0.014$ radians) and worst case depression angle of $\theta = \pi/2$ results in the approximate expression for d given in Eq (35).

61
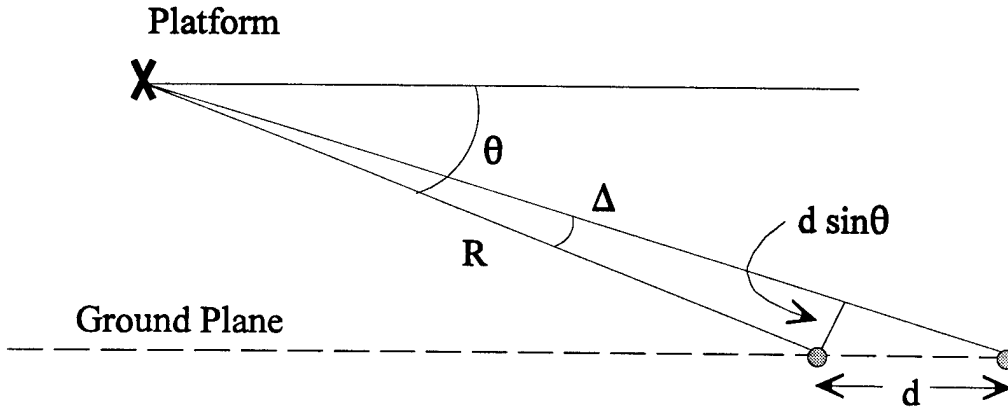
Figure 50: Relation Between Required Angular Resolution and Pixel Spacing

$$\Delta = \arcsin\left(\frac{d \sin\theta}{R} \right) \tag{34}$$

$$d = \frac{\Delta R}{\sin\theta} \approx 0.014\,R \tag{35}$$

Provided the distance R from the radar platform to the center of a range gate is greater than about 7.0 km, a pixel separation distance of $d = 100$ meters in both the x and y dimensions in the Global system provides the necessary angular resolution in the AER-1 system after coordinate transformation. The pixel spacing requirements are thus established as regular 100 meter spacing in the Global Cartesian coordinate system.

One final note regarding pixel spacing determination. Pixels are required to be separated by distance d and *regularly spaced* over the surface area of interest. For the Global Cartesian coordinate system, the surface area of interest is the projected area of the terrain in the x-y plane. Given terrain height variations are z directed, the projected surface area of the terrain does not entirely describe the physical characteristics of the terrain in all regions. For example, a tall hill with steep sides having a projected area of 1 km^2 in x-y plane has

more physical surface area than a perfectly flat, level section of ground with the same projected area (in this case the projected area approximately equals the physical area). Errors in surface area representation are not accounted for in this model since they are not expected to adversely affect backscatter calculations.

3.5 Resources Available

Construction and testing of the 3-D clutter model requires fusion of two different types of data sets, measured RCS statistics for various terrain types and digitized measured ground height. Measured RCS statistics are available for numerous real world scatterers such as trees, grass, and roads [14]. These statistics are normalized and reported in units of m^2 which is very convenient for creating RCS values representative of the ground in proper units. However, a sub-model is needed to provide backscatter coefficients for a computer simulation. This task is discussed in Chapter 4.

The National Imagery and Mapping Agency (NIMA), formerly the Defense Mapping Agency (DMA), has nearly worldwide Digital Terrain Elevation Data (DTED) available on compact disks (CDs) [15]. The DTED files are rastered data sets of altitude posts, i.e. a large matrix where each element represents altitude above sea level and the element position in the matrix corresponds to the altitude post position on the earth's surface. DTED is currently available in Level 1 and Level 2 format where Level 1 posts are equally spaced in 3.0 arc second intervals in both latitude and longitude and Level 2 a denser with post spacing every 1.0 arc second in each dimension. Since equal arc second spacing does not correspond to equal rectangular grid spacing, interpolation is used to transform post spacing from a

63

spherical system to a Cartesian system using a locally planar sea level approximation. Details of the DTED interpolation process are provided in Chapter 5.

Since this research effort is the first to fuse measured backscatter statistics and DTED data to create a novel 3-D clutter model, a reliable source of theoretically predicted scattering behavior from ground patches, patches which include variations in scattering center height and distribution, is needed to provide a basis for comparison and validation of digital model results. The Beckmann electromagnetic scattering model [12] provides such a basis and was used to obtain the validation results provided in Chapter 6.

4. Backscatter Coefficient Generator

For the digital model to produce realistic terrain backscatter values, a backscatter coefficient generation routine is required that is based on "real world" reflection values. Two possibilities exist for generating such data: 1) a very complicated electromagnetic model could be used to exactly calculate scattering for various terrain types, or 2) a simple generating function may be found that, by the nature of its construction, returns coefficient values similar to those observed when measuring terrain scattering.

4.1 Model Philosophy

A reliable backscatter coefficient generating function produces complex values that reflect dependence on both terrain type and angle of incidence. Further, the scattering coefficient values produced should extend over the entire range of measured data, accurately reflecting the wide range of possible scattering values for any single terrain type. Any generating function that repeatedly returns the same complex coefficient value for a given terrain type and observation angle is overly simplistic and is not acceptable for validation of the ACE technique.

As published by Ulaby and Dobson, the measured backscatter data set used for this research effort does not represent actual backscatter numbers, rather, the statistical properties of the backscatter numbers and their frequency of occurrence in histogram form [14]. This data reflects reality in that backscattered energy from any patch of terrain is determined by the actual properties of the terrain, the process is so complicated it may be viewed as probabilistic. Such a presentation of statistical backscatter data, in terms describing a

random variable, lends itself to the second of the two generating function development methods mentioned above. Specifically, a backscatter generating function is developed, independent of the electromagnetic properties of the terrain, whose output characteristics match the statistical mean and standard deviation of the measured data to the number of significant figures reported, provided the inputs to the generating function match the terrain type and angle of incidence of the measurements. Additionally, the frequency of occurrence of the generator output is compared to the frequency of occurrence of the measured data using a Chi-Square test; this test failed to reject the backscatter generator as representative of the measurements at a 0.05 level of significance.

The measured data set contains statistical mean and standard deviation values for nine different terrain types at incidence angles of 0 to 80 degrees in 10 degree increments. For development and demonstration purposes, only the X-band Vertical-Vertical (VV) polarization backscattering data is considered. Although more detailed data is available, i.e., "finer" terrain classifications, multiple polarization cases, and multiple radar frequency bands, the selected subset of published data provides an adequate basis for developing an initial backscatter coefficient generator prototype. The following nine terrain "type" classifications are considered for generator development with a additional "composite" or "unknown" terrain type produced by statistically combining data of each.

Soil and Rock	Trees	Grasses
Shrubs	Short Vegetation	Road Surfaces
Urban Areas	Dry Snow	Wet Snow

Different statistical Probability Density Functions (PDF's) can be formed by functionally operating on a uniformly distributed Random Variable (RV) which takes on values between 0 and 1, notationally [U(0,1) RV]. Since U(0,1) RV generators are widely available and easily constructed, a backscatter generating function is created using a U(0,1) RV to provide statistical variability while accepting terrain type and incidence angle as input arguments. When the generator function uses a single manifestation of the U(0,1) RV it returns a single number. However, when a long sequence of U(0,1) RV is used with a given terrain type and incidence angle, coincident with the measured data set, the first two statistical moments of the generator output data match exactly with published values. These results were obtained for all measured data sets with 10 degree incidence angle spacing using any of the nine terrain types.

4.2 Generating Function Issues

The backscatter generating function shown in Eq (36) is essentially a Weibull distribution based on a U(0,1) RV formulation with three parametric inputs, α, β and γ. The U(0,1) RV provides the probabilistic effect for the output data and the three input parameters provide functional behavioral "control" as a function of terrain type and angle of incidence. Functionally, the backscatter function operates in this manner: Terrain type and angle of incidence input arguments are used in a 2-D look-up table to find the corresponding variables, α and β; γ is fixed at 0.01 for this version of the model. These parameters are then used in the function along with the RV to produce the output coefficient. The number of RV terms passed to the function determines the number of output coefficients produced.

$$\sigma_{\text{Backscatter}} = \beta \cdot \left\{ \left[-\ln(RV) \right]^{\alpha} \right\} + \gamma \tag{36}$$

The α and β parameter values directly affect the statistical mean and standard deviation of the output stream; the γ term is a modification to the functional form found to be necessary to produce the desired results, but it is constant for all terrain types and angles of incidence. For the backscatter generator to operate under conditions outside the scope of this research, i.e., at other frequencies or wave polarizations, the value of γ may need to be changed. The values of α, β and γ are experimentally determined by a process described in the discussion that follows.

First, some comments on using the measured data set are necessary. The 10 degree angular granularity of the measured data sets is too coarse to produce acceptable results. Therefore, the statistical mean and standard deviation of the measured data sets are interpolated using cubic splines, producing "finer" data sets with one degree angular granularity. For incidence angles above 80 degrees, interpolation is not possible and due to grazing effects extrapolation might not be reliable. Therefore, another functional form is found to transition from measured values at 80 degrees to a mean 20 dB lower at 90 degrees. This -20 dB value was selected based on the general backscatter curve roll-off characteristics for non-specific terrain types [13] rather than on measured data. However, angles in this region are rarely encountered in an ACE performance simulation since the geometry required to provide grazing angle backscatter places the clutter in the radar's main beam. ACE does not function as such and both the platform and target are on the ground. A grazing angle condition only exists at a few points which, due to their slope, are nearly totally shadowed.

The specifics of the angular transition region are as follows: If the function takes an argument set containing an angle of incidence of 90 degrees, the α-β values corresponding to an 80 degree angle of incidence are used, and the result is then lowered by 20 dB. If the functional form takes an argument set containing an angle of incidence between 80 and 90 degrees, the α-β values corresponding to an 80 degree angle of incidence are used, and the result is then lowered by an amount corresponding to the angle's value relative to the 80 and 90 degree limits. The transition curve is arc shaped and based on a portion of a sinusoid, attempting to preserve first derivative continuity of the moments at 80 degrees.

The "desired" statistical means and standard deviations are indexed on terrain type and incidence angle in one degree increments over the 0 to 80 degree range. The final data set used for "developing" the generating function consists of raw published values at 10 degree spacing with cubic spline interpolated values in between. The α-β search space is first defined and the first two statistical moments of the function output are found for every α-β combination in this space. A single weighted error is found at all points between the "desired" and "calculated" data sets for both the mean and standard deviation. The weighted error is the simple mean of mean and standard deviation errors divided by the measured value. The α-β pair corresponding to the lowest weighted error is then selected and referenced to the terrain type and angle of incidence index.

After an initial α-β "trial pair" are associated with each terrain type at each incidence angle, the α-β values are "conditioned", i.e. the granularity of the α-β spacing is reduced and a higher density search space is constructed in the neighborhood of the trial pair. A final α-β pair is found that produces the lowest possible weighted error; the absolute error between the

"desired" and "calculated" means and standard deviations is 0.0 within tolerance of the significant figures provided in the original published data set, i.e., the "calculated" moments matched the "measured" moments to within the original number of significant figures.

A few issues surfaced during initial attempts at creating the backscatter generating function. The statistical moments of the output data stream are closely related to the quality of the U(0,1) RV. If the RV algorithm used for generating the α and β set does not produce a truly uniform distribution, incorrect α-β parameter sets are found. This is also true if the RV is not "long enough," i.e., the sequence produced by the RV needs to contain enough elements such that it possess the desired mean and variance properties. Several "typical" U(0,1) RV generators, as available in common programing language packages, were considered and found inadequate for producing a "stable" α-β set. Each attempt at finding an α -β pair for a given terrain type and incidence angle with a particular U(0,1) RV algorithm produced a slightly different set. Thus, for constructing a reliable α-β set a generated input sequence was used:

$$\text{Construction Series} = \left\{ \frac{1}{N}, \frac{2}{N}, \dots, \frac{N-1}{N} \right\} \tag{37}$$

Further, the α-β set is dependent on N and converges for N $\approx$ 100,000.

The RV quality issue is not overly important in the use of the backscatter generating function since the quality of RVs generated via most popular random number generators improves for very long sequences. Considering that a new RV manifestation is called for each pixel, as observed by the simulated radar at each platform position, for which the SCR is calculated, the length of the RV sequence forces convergence to a nearly uniform PDF.

Using such a lengthy sequence would have not only prevented timely construction of the appropriate α-β set, but also, would have made testing of alternate functional forms impractical.

Another issue addressed is the granularity and extent of the α-β search space. Early results suggested that relatively small α-β combinations are most likely to produce a solution for the generating function look-up table with a few solution pairs existing for significantly large values of α and/or β. In addition, the smaller the α-β values, the more sensitive the resulting weighted error. The top left-hand plot in Fig 51 graphically demonstrates the clustering effect of small α-β solution pairs where each dot represents a possible solution. Constructing an α-β search space with fine enough granularity and large enough extent would have provided a computationally infeasible construction scenario. Therefore, the α-β search space is constructed with varying granularity, dense for small α-β values and sparse for larger α-β values. This results in more evenly spaced solution pairs as depicted graphically in the top right-hand plot of Fig 51.

Finally, the weighted error, a single number containing both the mean and standard deviation errors of the backscatter generator output, is examined for the possibility of producing multiple relative minima. Even with a variable density search space, the granularity of the α-β increment does not guarantee the initial "trial pair" will survive and become the "final pair" used in the model. The variable density approach only provides a "trial pair" of sufficient quality such that the "final pair" can be found in reasonable time. Since the "final pair" solution requires construction of an ultra-high resolution search space in the neighborhood of the "trial pair," and is selected from the minimum weighted error

71

found in this space, it was necessary to ensure that the relative minimum found in the ultra-high resolution search space is a global minimum. When an α-β pair is found that has a weighted error of 0.0 to the decimal place of the measured data, this "final" α-β pair is placed in the look-up table, indexed to the corresponding terrain type and angle of incidence. The process is then repeated for the next terrain type and angle of incidence pair.
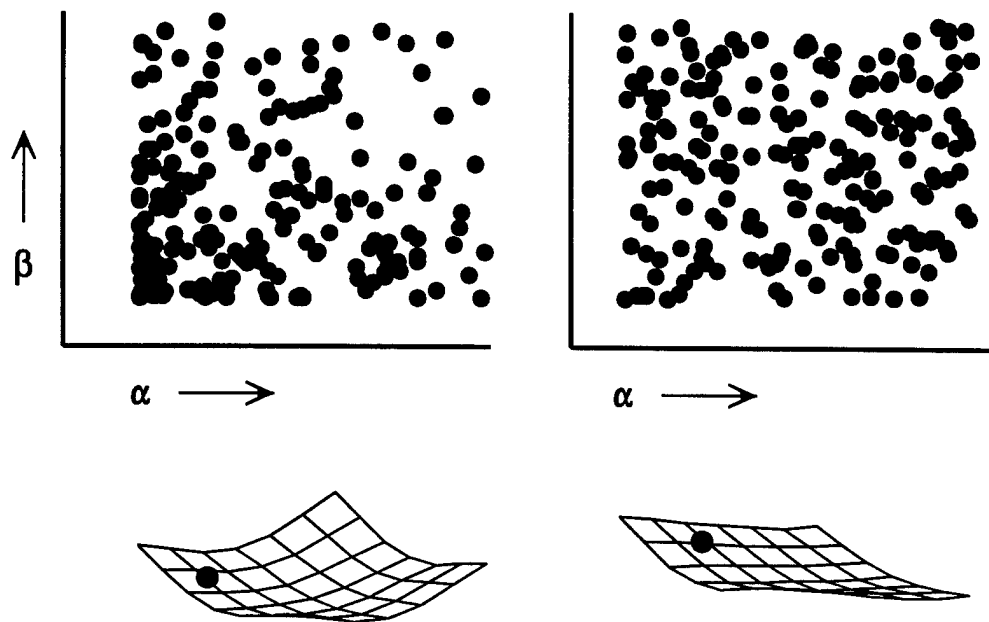
Figure 51: Generating Function Parameter Selection Issues

The lower portion of Fig 51 reflects two possibilities for the neighborhood search or "conditioning" phase of the α-β parameter set construction. The "final pair" is either found in the neighborhood of the "test pair," represented by the black dot on the lower left-hand side of the figure, or the minimum is found on an edge of the neighborhood as shown on the lower right-hand side of the figure. For this later case, a new "test pair" is created on the edge and a new search space defined until a "final pair" is found.

This process was repeated using different functional forms, and the function producing the best overall performance, shown in Eq (36), was selected for use. Results from the backscatter coefficient generator are shown in Fig 52 and compare very well with equivalent published plots from the same measured data set [16].
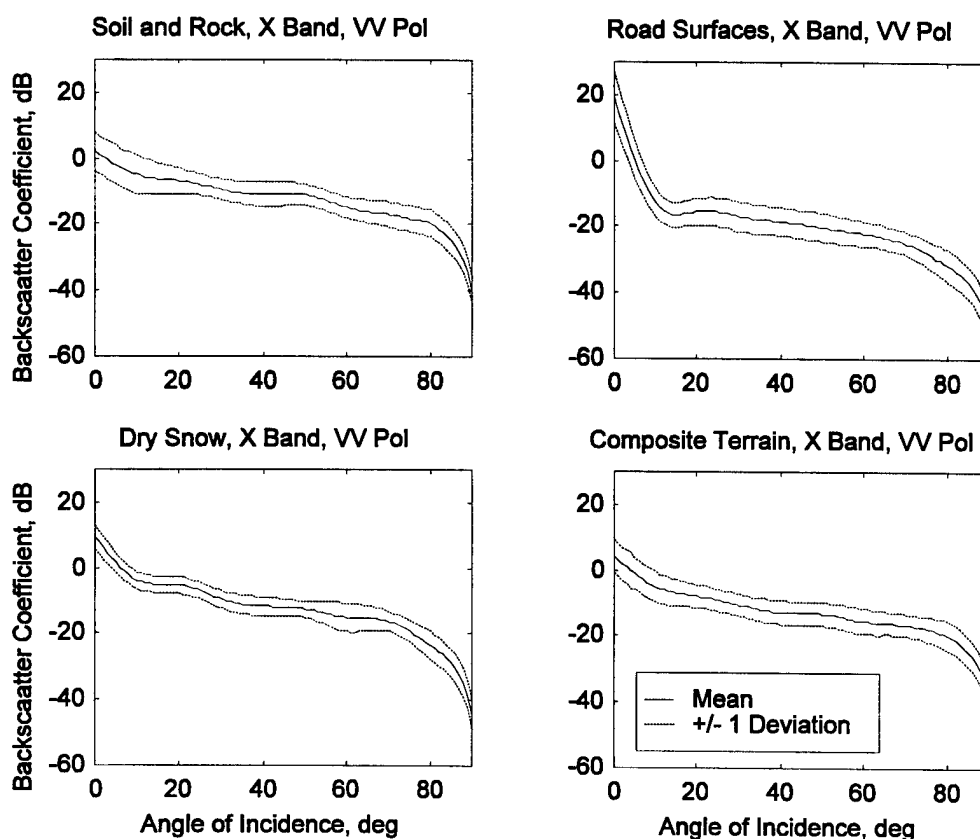
Figure 52: Calculated Backscatter Statistics for Various Terrain Types

4.3 Comparison of Generator Results with Measured Data

When using two degrees of freedom, almost any well chosen function can simultaneously meet two target values. Virtually any PDF can match a desired mean and

standard deviation exactly. The difficulty in choosing an appropriate functional form that can reliably represent a measured data set is manifest by attempting to reproduce an output with a frequency of occurrence (FOQ) histogram similar to that of the measured data.

Figures 53 through 56 are backscatter coefficient FOQ histograms for various terrain types. The overlaid data represents a comparison of measurements, as published by Ulaby, with results from the generator for specified terrain types and incidence angles using the input sequence from Eq (37) with N = 100,000. The solid dark lines in the figures outline the histograms obtained from the backscatter coefficient generator FOQ; the figures suggest a near optimal choice for the backscatter coefficient generating function.

Two Chi-Square tests performed on the data shown in Fig 54 indicate that the generating function performance does indeed accurately represent the measurements. Since the Chi-Square test statistic depends on the number of degrees of freedom [17], two separate groupings were used. For one test, the data was divided into 0.5 dB bins, consistent with published data. The threshold for rejection, i.e., rejecting the generator as representative of the measurements, was 55.8 at a standard 0.05 level of significance. The test result was only 2.95, about 5% of the level for rejection. For the second test, the data was grouped into 1 dB bins, reducing the number of degrees of freedom. The new result was 1.7, again about 5% of the new rejection threshold of 30.1 for the same level of significance. These results indicate the generator "cannot be rejected"since the Chi-Square is a "null hypothesis" test.
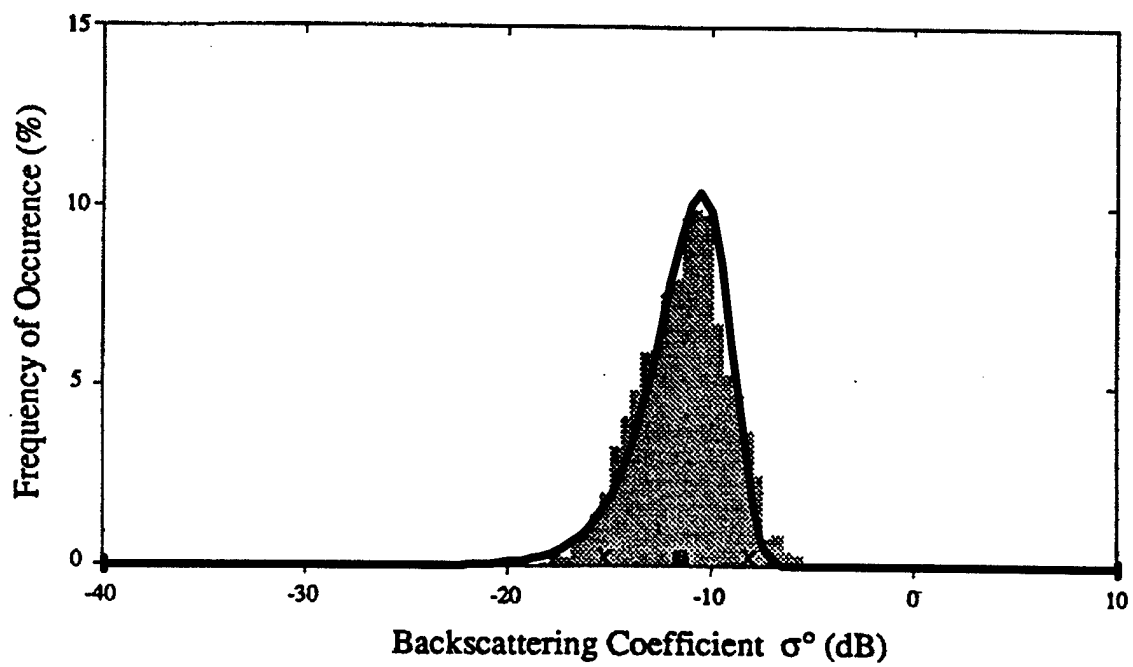
Figure 53: Measured versus Generated Coefficients, Shrubs at 60 degrees
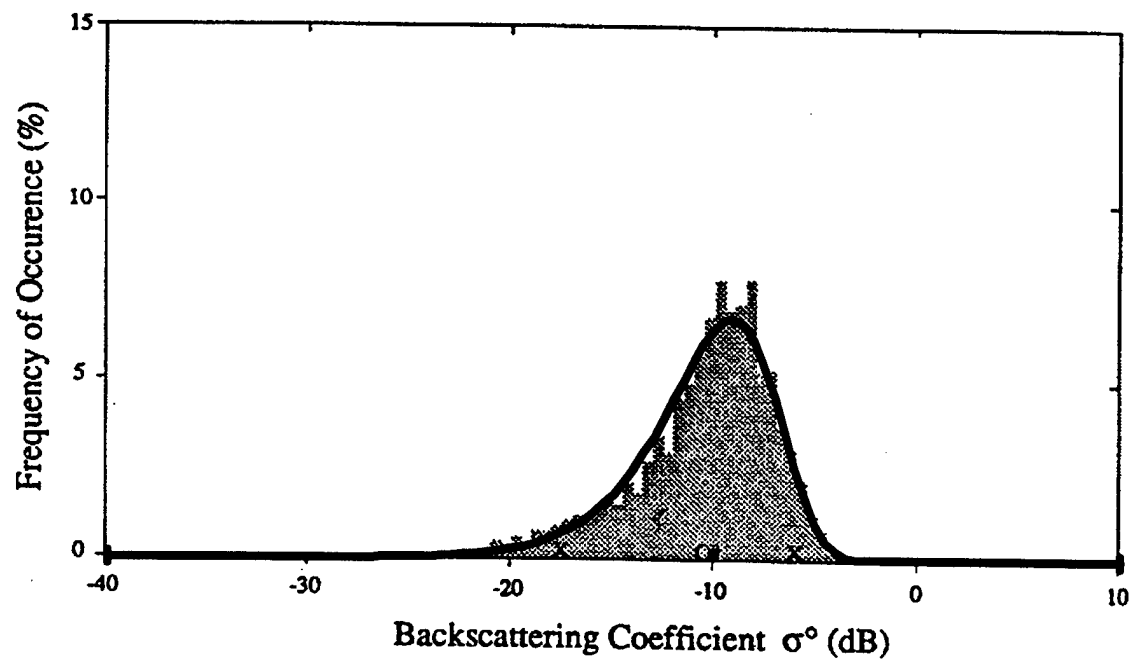
Figure 54: Measured versus Generated Coefficients, Short Vegetation at 40 degrees
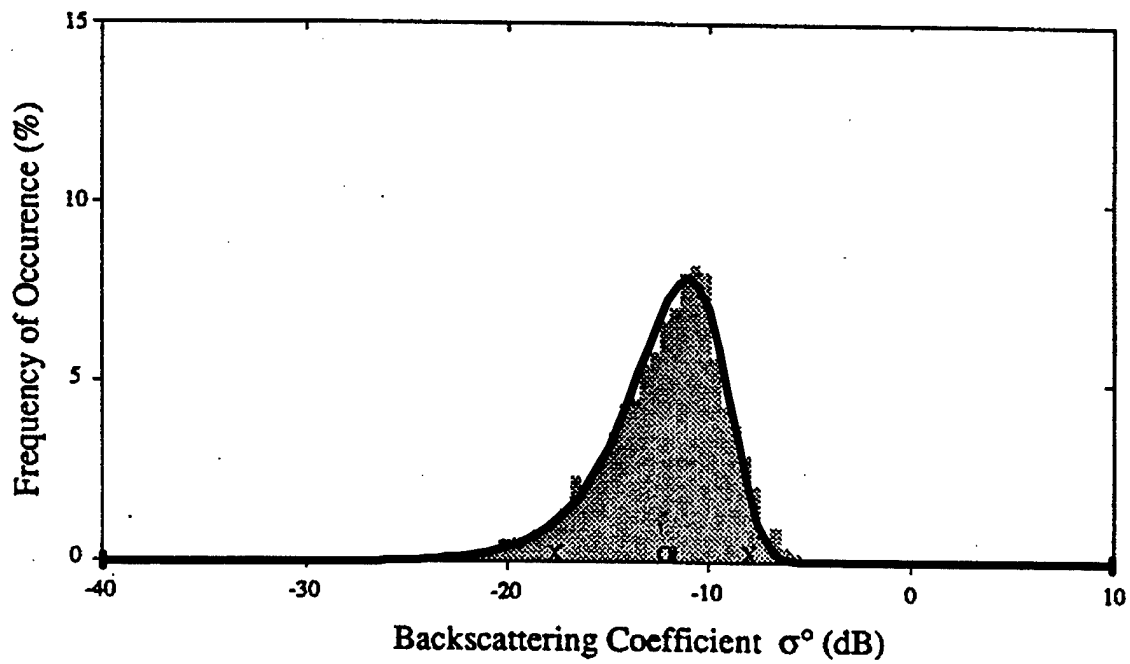
Figure 55: Measured versus Generated Coefficients, Short Vegetation at 60 degrees
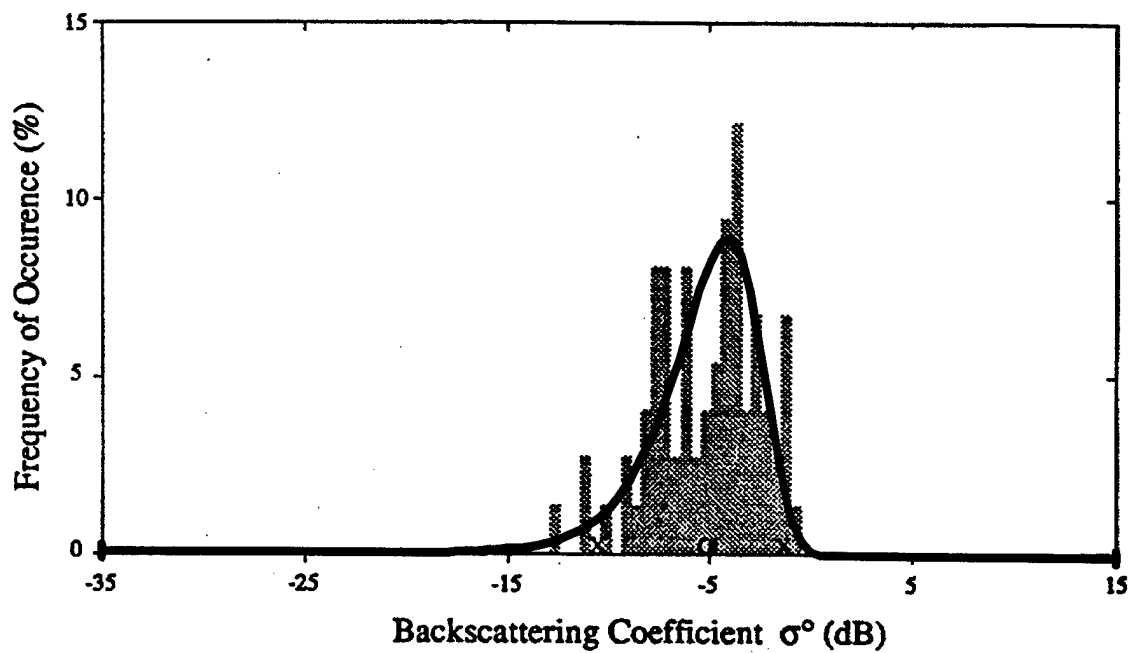
Figure 56: Measured versus Generated Coefficients, Dry Snow at 20 degrees

5. Terrain Interpolator

Level 1 Digital Terrain Elevation Data (DTED) with elevation post spacing every three arc seconds is available from the National Imagery and Mapping Agency (NIMA) for much of the earth's surface. These DTED data sets provide reliably consistent ground elevation data over virtually all terrain profiles, ranging from flat desert to rugged mountainous terrain. For constructing the digital model under this research effort, the DTED data represents the *best available* ground model available. Unfortunately, DTED elevation posts are not evenly spaced in meter units, a condition required in Section 3.4 for deriving ground pixel spacing requirements to ensure optimum model performance under various scenarios. Therefore, the DTED data is pre-processed to obtain evenly spaced data in meter units with a maximum distance in each row and/or column of 100 meters for most anticipated simulation altitudes.

Since current DTED data sets are based on the 1984 World Geodetic Survey (WGS-84) ellipsoid earth model datum, the conversion from three arc second to meter spacing at sea level is done using the earth's geometric characteristics and properties according to Eqs (38) and (39).

$$R_{Equator} = 6,378,137 \text{ Meters}$$

$$\text{Eccentricity} = 0.818191908426 \tag{38}$$

$$R_{Polar} = R_{Equator} \sqrt{1 - \text{Eccentricity}^2} = 0.99665 \, R_{Equator}$$

$$1 \text{ Arc Second}_{\text{Equator}} = \frac{2 \pi R_{\text{Equator}}}{360 \times 60 \times 60} \text{ Meters}$$

(39)

$$3 \text{ Arc Seconds}_{\text{Equator}} = \frac{6 \times \pi \times 6,378,137}{1,296,000} \text{ Meters} = 92.7662 \text{ Meters}$$

Since the earth's radial distance is a function of latitude, the general conversion is:

$$3 \text{ Arc Seconds}_{\text{East/West}} = 92.7662 \text{ Cos (Latitude) Meters}$$

(40)

According to Eq (40), the original DTED data post spacing is not only a non-integer number of meters but also is non-constant. However, its behavior is consistent and predictable so that a properly chosen interpolation technique can provide good estimates of both azimuth and elevation values at desired pixel locations.

5.1 Interpolation Function Uses

An interpolation scheme has been developed under this research effort which accomplishes the following tasks: 1) conversion of original DTED data from the original non-uniform spacing to a uniform 100 Meter by 100 Meter rectangular grid, 2) synthesization of new data between given data points, thereby increasing resolution, 3) determination of ground slope at specified pixel locations, and 4) estimation of mountain peak location and height for peaks not explicitly included in the DTED sampled data. Figure 57 graphically depicts the spacing conversion and data synthesization functions of the interpolation scheme.

The Xs in the figure are original data points, position converted data is represented by the Os, and the synthesized higher resolution data is represented by the smaller os.
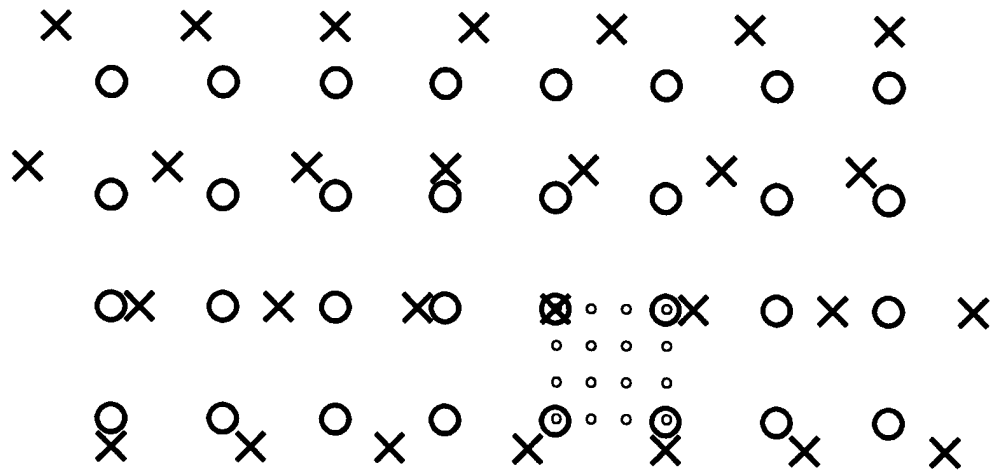
Figure 57: Data Coordinate Transformation and Higher Resolution Synthesis

The need for synthesizing higher resolution data is driven by: 1) potential simulation scenarios where platform-target ranges are closer than the minimum range requirement calculated in Chapter 3, and 2) anticipation that higher resolution terrain data may be required in support of future SAR simulations and models. Additionally, an interpolation method that excels at synthesis can be expected to excel at data position conversion as well. Likewise, an interpolation technique that performs poorly at synthesis should not be expected to perform reliable data position conversion. Data position conversion can be viewed as higher resolution synthesis by a factor equal to the least common denominator of the original and final data spacing followed by decimation to the desired number of points.

Estimation of ground slope at a specified pixel location is necessary for calculating the angle of incidence, i.e., calculation of the angle between the surface normal vector and

79

the ray pointing toward the ACE system aperture as shown in Fig 58. This angle is important

since it directly affects the backscatter coefficient value. Using terrain slope in incidence

calculations also leads to a quick, although not complete, definition of shadowing, i.e.,

shadowing may be defined to occur at pixel locations where the angle of incidence is greater

than 90 degrees. This condition is shown in the rightmost sketch of Fig 58. In the absence

of ground slope information, the angle of incidence for all pixels at an altitude lower than the

ACE platform would have an upper limit slightly below 90 degrees, always appearing as

illustrated in the leftmost sketch of the figure, regardless of how much the ground is pitched.
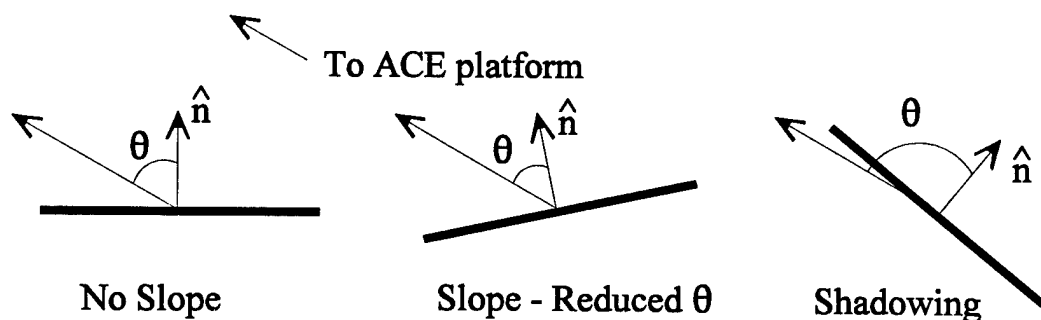
Figure 58: Effect of Ground Slope on Angle of Incidence

Since DTED data exists at predefined locations, i.e., at equal arc second intervals,

there is no gaurantee that relative or localized extremum are included in the data set. Rather,

the extreme altitude points can be expected *not to fall on an elevation post* and therefore *not

included* in the DTED, i.e., relatively sharp terrain peaks are not reflected in the DTED data

and the highest reported elevation value within the neighborhood of the peak is somewhat

lower than the actual peak elevation. Via numerical integration techniques, it can be shown

that the expected value of the horizontal radial distance between a terrain extremum and the

closest DTED sample taken within the neighborhood of the extremum can be estimated in accordance with Eq (41) (valid for DTED Level 1 data only).

$$E\{ \Delta \} = 92.7662 \times 0.271 \sqrt{1 + \text{Cos}^2(\text{Latitude})} \text{ Meters} \qquad (41)$$

For example, at a location of 36 degrees latitude near the Grand Canyon, Eq (41) yields an expected radial distance value of 32.3 meters (106 feet) when using DTED Level 1 data. By a similar process used for deriving Eq (41), it can be shown that the expected radial distance value for DTED Level 2 data at the same location is 10.8 meters (35.4 feet). This result is consistent with the fact that DTED Level 2 data is nine times denser than Level 1 data with altitude post spacing every 1 arc second in each direction. A good interpolation technique can provide a realistic estimate of peak height and location between DTED posts by synthesizing higher resolution data with sufficient density and searching for the highest value in the synthesized data set.

5.2 Existing Interpolation Methods

Three common interpolation methods were examined for applicability to this research, including, the Bi-Linear, Bi-Cubic, and Bi-Cubic Splines techniques [18]. Bi-Cubic interpolation requires the specification of both the data point values and derivatives. Manual estimation and specification of directional derivatives for a large data set, such as a DTED file, is prohibitively time consuming. Estimation of derivatives via recursion formulas turns Bi-Cubic interpolation into Bi-Cubic Spline interpolation. In

essence, the two primary methods considered under this effort were the Bi-Linear and Bi-Cubic Splines techniques.

The formulation for Bi-Linear interpolation of data on a regular, square grid is straightforward. For the interval shown in Fig 59, Eq (42) may be used to obtain an altitude value for point E where A, B, C, D represent given altitude values, Δx and Δy are the x and y dimensions of the interval, and t_x and t_y are the x and y distances from point A to the interpolation point. Other variants to this technique exist for sampled data on an irregular grid, or at triangular rather than square intervals.
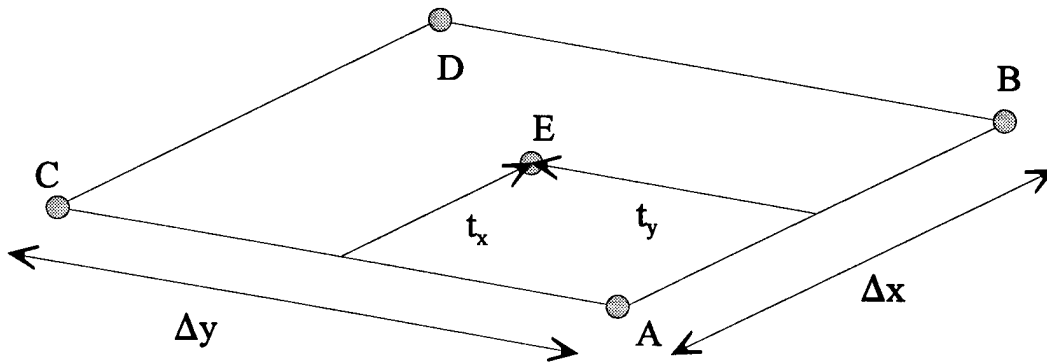
Figure 59: Bi-Linear Interpolation Interval Parameters

$$E = A \left(1 - \frac{t_x}{\Delta x} \right) \left(1 - \frac{t_y}{\Delta y} \right) + B \left(\frac{t_x}{\Delta x} \right) \left(1 - \frac{t_y}{\Delta y} \right)$$
$$+ C \left(\frac{t_y}{\Delta y} \right) \left(1 - \frac{t_x}{\Delta x} \right) + D \left(\frac{t_x}{\Delta x} \right) \left(\frac{t_y}{\Delta y} \right) \tag{42}$$

The Bi-Cubic Spline interpolation technique is somewhat more complex than the Bi-Linear technique and involves of the following steps: 1) each row of data in a 2-D matrix is interpolated via cubic splines, 2) spline values are calculated at points corresponding to

columns where new interpolated data is desired, 3) interpolation is carried out between each column of solved points. This procedure is graphically illustrated in Fig 59 where each arrow represents a spline, original data points are shown as Xs, and the final interpolated data set is represented by the Os. The mathematical formulation for a single 1-D spline is shown in Eq (43). With cubic spline interpolation, a new cubic equation is created for each interval between data points. As indicated by the subscript n in Eq (43), each spline is only valid over a single interval.
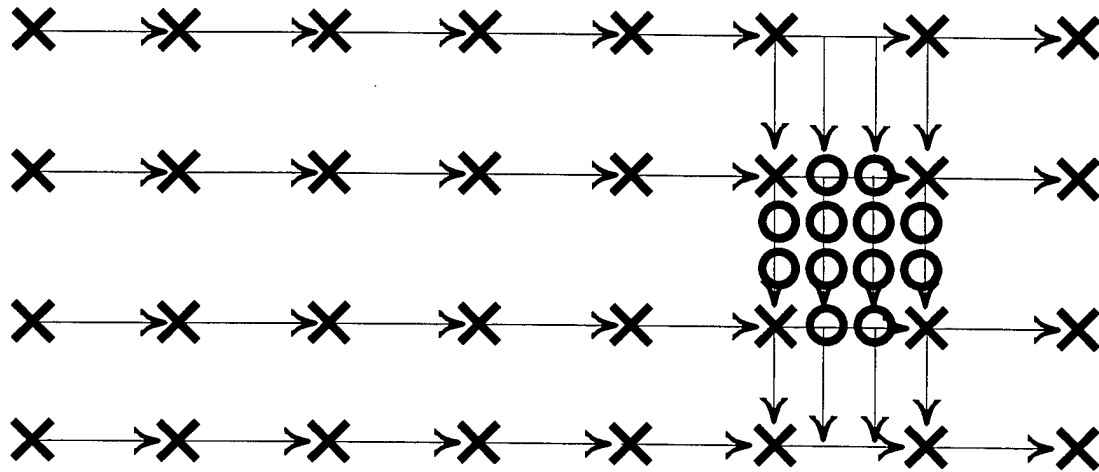
Figure 60: Bi-Cubic Spline Interpolation Method

$$S_n(t) = a_n + b_n t + c_n t^2 + d_n t^3 \tag{43}$$

The generation of cubic-spline coefficients is well documented in many texts addressing interpolation and is not repeated here. However, the multi-dimensional aspect of cubic spline interpolation merits a few comments.

The extension of cubic-spline interpolation techniques from 1-D is not limited to 2-D, but rather may be extended to any number of dimensions [19]. For an N-Dimensional data set, the procedure involves the following: 1) order the dimensions 1 through N,

83

2) interpolate dimension #1 in all other dimensions, dimension #2 through N, 3) interpolate dimension #2 in the higher density dimension #1 and the remaining dimensions, dimension #3 through N, . . . 4) continue this process until all N dimensions have been interpolated. Since interpolation of the final dimension requires interpolation between points found from interpolation of all lower numbered dimensions, the final step requires $F^{(N-1)}$ times as many calculations as interpolation of the first dimension. For this example, F is the interpolation factor, the number of desired points in each dimension divided by the number of original points in each dimension, assumed to be constant.

This procedure raises the interesting question of whether or not the ordering of dimensions affects the results. The answer is "No," so long as a single, unique interpolation scheme is used in all dimensions. This is reflected in the following statement:

Given an N-Dimensional data set, S_N, regularly spaced in Cartesian coordinates and any unique 1-D interpolation operator, $_DI_F^{O}$, using a polynomial of order O (not zero), interpolation factor F, operating in dimension number D, then:

$$_1I_F^{O}\left\{ _2I_F^{O}\left[\cdots \, _NI_F^{O}\left(S_N\right) \cdots \right] \right\} = \, _{A_1}I_F^{O}\left\{ _{A_2}I_F^{O}\left[\cdots \, _{A_N}I_F^{O}\left(S_N\right) \cdots \right] \right\} \qquad (44)$$

where $\{A_1, A_2, \dots A_N\}$ is any permutation of $\{1, 2, \dots N\}$. As presented here without rigorous proof for an iterative application of all 1-D polynomials, it can be proven for 2-D LaGrange polynomials [20]. This has been verified numerically for piecewise 1-D polynomials from linear up to cubic over a wide array of multi-dimensional poorly behaved and undersampled data sets. The use of poorly behaved data sets was to validate Eq (44) even when the polynomials were ringing wildly. Further, Eq (44) may be valid for any

84

unique method, not just polynomials and has important consequences for users of multi-dimensional interpolation techniques [19]. The interpretation of these results for Bi-Cubic Spline application is that a "rows then columns" order produces identical results as "columns then rows" processing order.

Neither the Bi-Linear nor the Bi-Cubic Spline interpolation method are used in their pure form for the terrain interpolation technique developed under this research effort. The new method, K-Splines, is a hybrid technique developed with the goal of exploiting the best properties of each method while avoiding the problems associated with each.

5.3 Bi-Linear Interpolation Issues

Although the Bi-Linear interpolation is unique to any subset of the original data, is easily implemented, and lacks the anomaly propagation problem of the Bi-Cubic Spline method (Sect 5.4), it produces an unwanted smoothing or filtering effect. As discussed earlier, terrain extremum such as mountain peaks and valleys are not expected to be accurately characterized by sampled DTED data. Unfortunately, all linear interpolation techniques produce interpolated data values that fall between the extremum of the sampled data used, i.e., if a mountain peak exists between four elevation samples taken at slightly lower and differing elevation values, then the interpolated altitude value at the latitude and longitude position of the peak is not only lower than the actual peak value but is also lower than the highest elevation sample used for the interpolation. This effect is demonstrated by comparing Figs 61 and 62 where linear interpolation has been used to convert the original DTED data of Fig 61 from equal arc second spacing to the regularly spaced 100 meter by 100
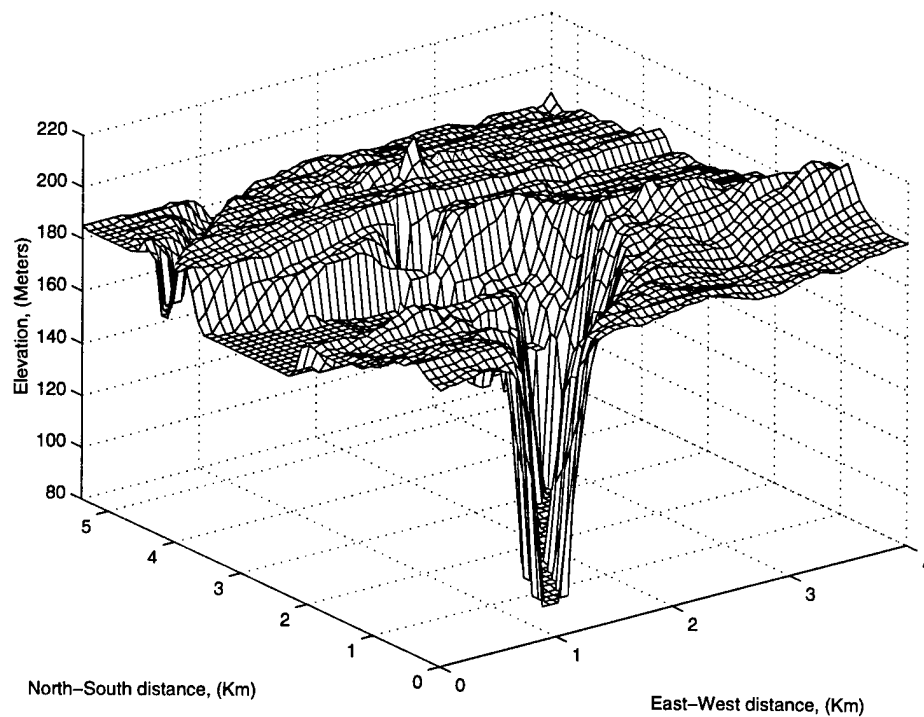
Figure 61: Original Niagra Falls DTED as Viewed from North-East
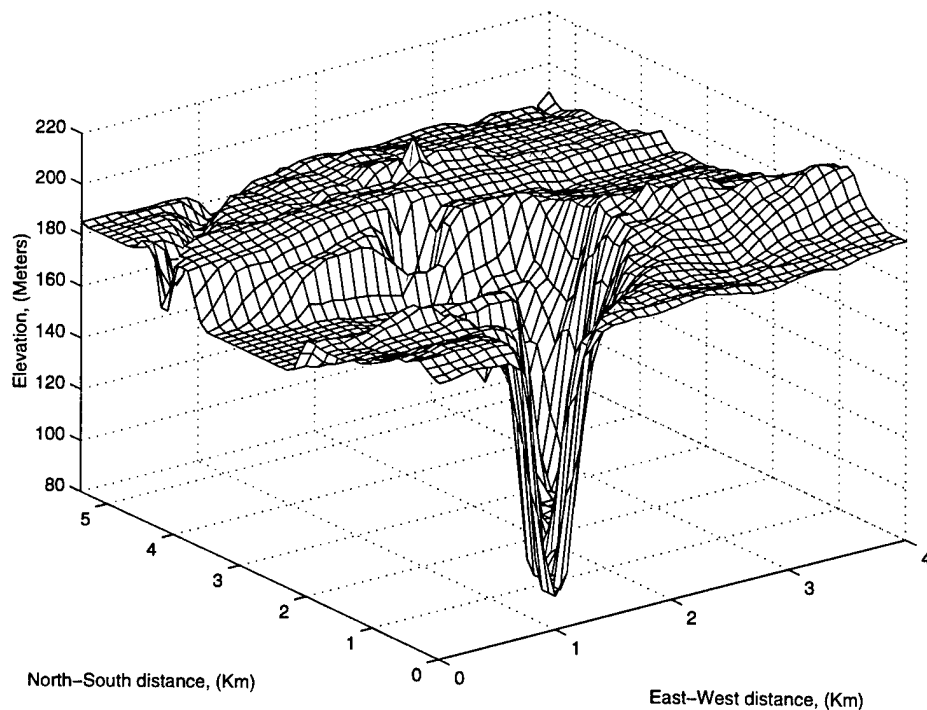
Figure 62: 100 Meter Spacing Data Set Found via Linear Interpolation

meter Cartesian grid of Fig 62. The original DTED has N/S and E/W roughness indices (RI_2) of 6.3 and 6.9, respectively. The same indexes for the Bi-Linear interpolated data set, adjusted for the spacing change, are 5.0 and 5.6. These new indices are about 80% of their original values, meaning the process of converting from equal arc second spacing to equal meter spacing smoothed the data by 20% as indicated by the change in the RI_2 index.

Such a result is not desirable if the intention of the interpolation process is to create a representative data set with only the horizontal positions of the altitude posts shifted to a more convenient spacing. Despite these shortcomings, linear interpolation techniques do possess two important properties that are desirable goals of any new method, namely, uniqueness and anomaly isolation. To examine these properties, the Bi-Cubic Spline interpolation technique is discussed since it can have problems with both.

5.4 Bi-Cubic Spline Interpolation Issues

The popularity of Bi-Cubic Spline interpolation is based on the performance of regular cubic splines in 1-D. For well behaved adequately sampled data sets, cubic splines often provide the best performance for the computational time and complexity involved. In the 2-D case, the splines are not limited to producing interpolated values within the range of sampled data being used and can actually estimate peak values occurring *between* samples. A side benefit of the technique is that the first derivatives of the polynomials are available at all the data points and thus provide an estimate of ground slope at any point. The two values (from the 2-D splines) can be combined to specify ground slope for use in the angle of incidence calculation.

Another interesting characteristic of the Bi-Cubic Spline method is that it can be used to convert DTED Level 1 data to an evenly spaced 100 meter data set. When reapplied to the evenly spaced data set, the Bi-Cubic Spline method recalculates the original data set with very high fidelity at the original 3 arc second spacing intervals (minus the last row and column). For example, a 601 by 601 matrix of DTED Level 1 data points was converted to a 557 by 451 matrix (at 36 degree latitude) of 100 meter by 100 meter data set with rectangular post spacing. This new data set was then re-interpolated to construct a 600 by 600 matrix of data that was virtually identical to a subset of the original DTED data, i.e. the original data set minus the last row and column. This same process cannot be accurately done with Bi-Linear interpolation since each iteration of the interpolation process produces more adverse smoothing.

Two potential problems are encountered when applying Bi-Cubic Spline interpolation techniques directly to DTED data: 1) error propagation due to "anomalous" data points and, 2) an apparent lack of uniqueness when interpolating multiple intersecting subsets of a larger data set. Cubic splines are formed using a recursion relationship that relates functional derivatives with sample data values. For the recursion relation to be solved and provide valid coefficient values, the second-order derivatives at the spline end points must be specified. If these values are unknown, as typically the case for data such as DTED, the derivative values are set to 0.0 [18]. Errors that result from specifying zero derivative values when the actual values are non-zero may be called "edge effect errors" for the 2-D case, since the error terms are largest at the edges of a 2-D data set and decrease when moving toward the center.

The uniqueness problem arises when edge effect errors from an interpolation procedure appear inside an interpolated data set. This occurs during the following scenario: a very large data set is examined at its original density and a subsection selected for interpolation to a higher resolution. Unfortunately, the Bi-Cubic Spline method requires interpolation of either all rows then only the columns appearing in the desired subset, or, all columns and then only the rows appearing in the subset. The computational time required for this procedure can become quite large. To speed up the interpolation process, only the region of interest is subjected to the Bi-Cubic Spline method, i.e., only a subset of the rows and columns are used. If another subset of data is selected for interpolation such that it "overlaps" the first subset, i.e., it contains some data points in common with the first data set, and consists of a different group of rows and columns, the edge effects of the interpolation process on this new subset of data produces slightly different values at the overlapping points; interpolated values are a function of the rows and columns in the procedure. Therefore, unless the entire data set is used during all subset interpolation procedures, the interpolated values are not unique. Since the Bi-Linear interpolation technique does not use a recursion formula, it has no edge effects and therefore is immune to potential uniqueness problems.

The anomaly propagation problem results from one or more data points causing excessive "ringing" in the splines that propagates through the data set via the recursive derivative calculation process. Here the term "anomaly" does not imply incorrect or inaccurate data, rather, the presence of a data point(s) that causes perturbations in the interpolated data set that might not exist in real data sampled at the same resolution. An

89

example of the 1-D cubic-spline "ringing" effect is shown in Fig 63 where asterisks represent original data points and the solid line is the interpolated result. The single original data point with a different function value at x = 6 represents the "anomalous" point even though its value may be accurate. The dips and rises in the curve between original data points having the same value may be assumed to be erroneous if the data set were representing real terrain.
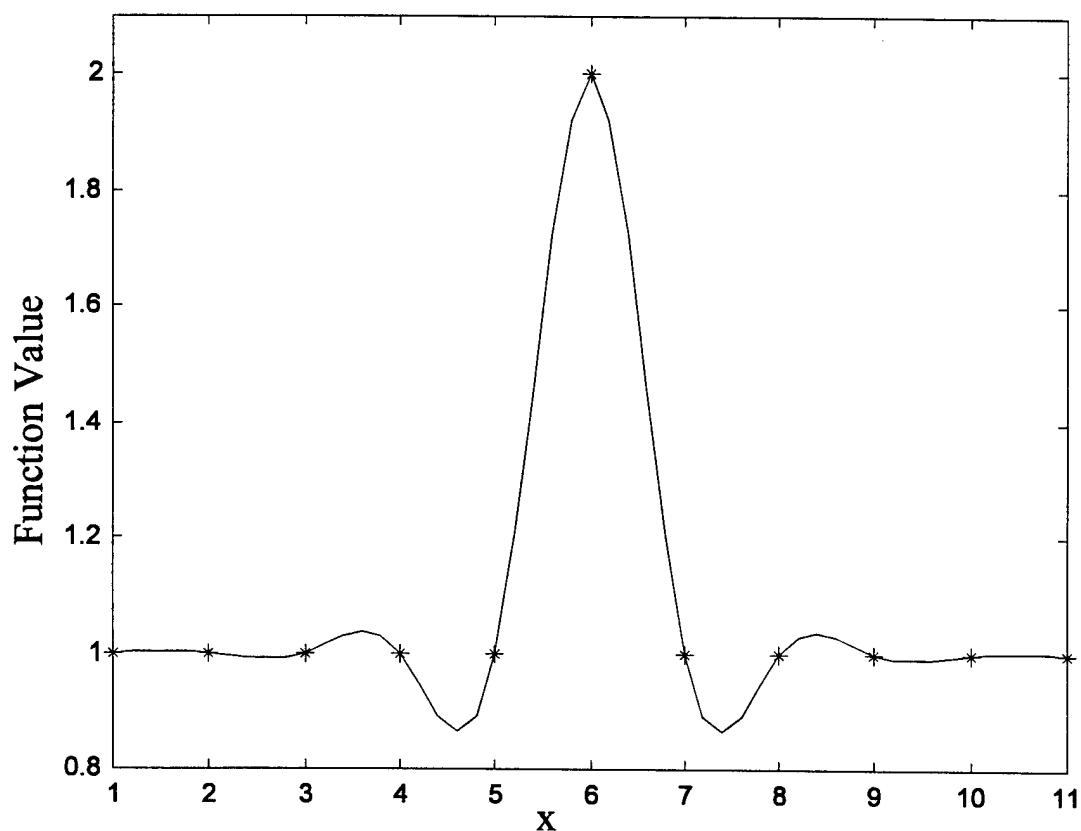
Figure 63: Ringing Effect in Cubic Spline Interpolation

In Bi-Cubic Splines, this "ringing" affects the recursion relationship of all splines formed in the neighborhood of the "anomaly", not just the splines in the same row or column. This occurs because secondary splines are created using the interpolated values from splines created during the initial interpolation process. The ringing effects created

during the initial spline creation process are therefore passed on to all splines subsequently created within its neighborhood as illustrated in Fig 64.
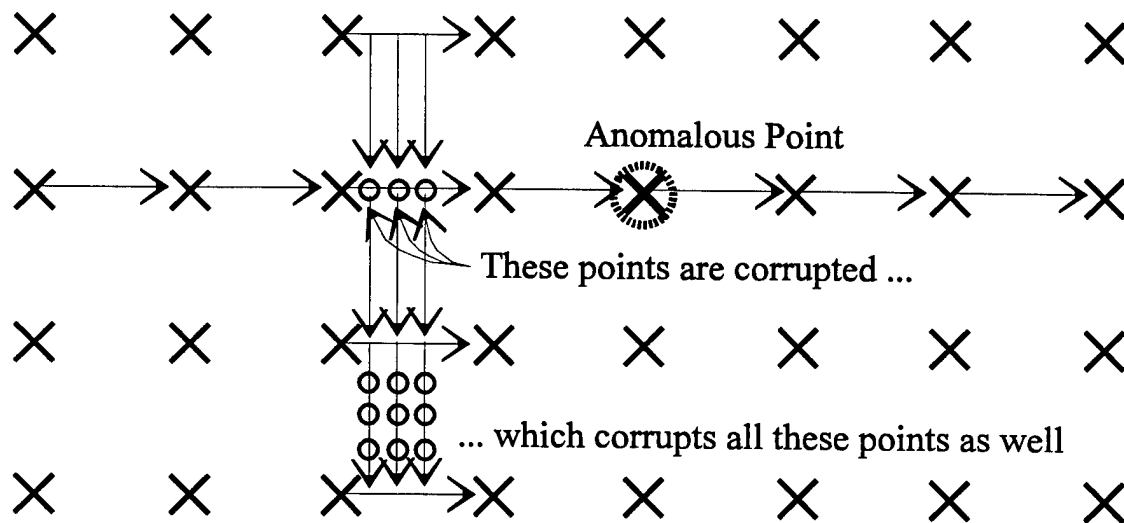
Figure 64: Anomaly Propagation Method in Bi-Cubic Spline Interpolation

Unfortunately, DTED data is not only full of such anomalous points but the anomalous point are spatially correlated as well. For many scenarios, the perturbations from closely spaced data points cause interference patterns, an excellent example of which is shown in Fig 65 [21] where the interference patterns appear as "Cornrows." For this figure, a pure cubic interpolation method was applied to Level 1 DTED data to produce the scene. The ridge lines shown in the figure do not exist in the real terrain, their presence is merely an artifact of the interpolation procedure produced by the "ringing" previously discussed.

The polynomial ringing is analogous to the aliasing phenomena exhibited the Fast Fourier Transform (FFT) and indicative of sampled data taken at a resolution inappropriate for the interpolation method being used. Since a Low Pass Filter (LPF) used prior to or in

91
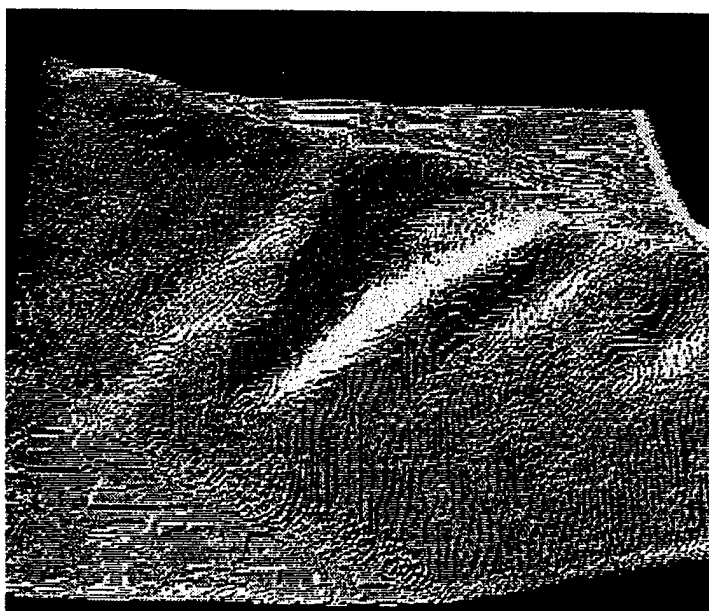
Figure 65: "Cornrow" Effect of Cubic Interpolation

conjunction with an FFT can reduce or eliminate aliasing, it seems possible that an equivalent LPF operation may be applied to the interpolation problem to help control the ringing. In fact, linear interpolation may be regarded as an LPF operation of sorts and is immune to ringing. This is in contrast to Bi-Cubic Spline techniques which may be regarded as having no "band-limiting" properties whatsoever. The interpolation problem may be viewed from a digital signal processing perspective. Just as too narrow a filter bandwidth can distort a signal and not pass an accurate replica (Bi-Linear) and no filtering leaves room for aliasing (Bi-Cubic), it makes sense that some form of engineered "bandwidth" control may provide a balance between predictive performance and acceptable behavior. What is needed for accurate DTED interpolation is a process that incorporates the predictive behavior of the Bi-Cubic with the uniqueness and anomaly isolation properties of the Bi-Linear technique; ergo, the development of "K-Splines" as presented below.

92

5.5 New Method: K-Splines

A new hybrid linear/cubic interpolation method, named "K-Splines", has been specifically developed to interpolate poorly behaved data sets such as encounter in DTED files. With this method, the RI_2 roughness index measures of interpolated data sets are virtually identical to original data sets when adjusted for the new spacing, independent of the direction used to calculate the roughness index.

The K-Spline interpolation technique involves two main steps: 1) determination of cubic spline coefficients, satisfying Eq (43), at given data points, and 2) interpolation and averaging within the region of interest, i.e., within the region to be interpolated. The uniqueness problem is solved by performing the cubic spline interpolation step only once. Computational efficiency, relative to Bi-Cubic Spline interpolation, is realized by enforcing the requirement that no matter how often Step 2 is performed, the spline coefficients are only found once at the original data point locations.

When a given region of interest is to be interpolated, only the coefficients at the four original data point "corners" surrounding each interval are needed to construct the entire surface within the region. Within the region between the set of four points, the following procedure is performed: 1) a new spline is formed in one direction by linearly interpolating the "edge" spline coefficients. This is cubic in one direction and linear in the orthogonal direction, 2) a linear error correction term is then applied to compensate for the difference between the value of the new spline at its end point and the value of the spline at the far edge of the interval, and 3) this procedure is repeated in the orthogonal direction and the simple mean of the two values obtained from different directional approaches is found.

Using only the original data points to find intermediate values prevents the ringing effects of anomalous points, which only exist between the original values as indicated in Fig 63, from affecting neighboring regions. This prevents the formulation of the so called "cornrow" effect illustrated in Fig 65. Additionally, because of the inherent anomaly isolation feature of the technique, it has been successfully applied to an image filter for screening out noise using a decimation and reconstruction process for images [22].

5.6 Comparison of the New Method with Bi-Cubic Splines

The advantages of the K-Spline method over the Bi-Cubic method are: 1) K-Spline coefficient calculations are much faster when the original data set is large and the desired interpolation region is relatively small or multiple regions are being examined, 2) a change in desired resolution does not require reconstruction and evaluation of new splines spanning at least one dimension of the data set, 3) edge effects are minimized on the interior of the data set, and 4) errors due to anomalous points are contained rather than propagated.

The test scenario of a plane containing three anomalous points is presented in Fig 66. This data set is interpolated using both the Bi-Cubic Spline and K-Spline techniques. The regions containing the anomalous points are nulled out, i.e., the regions containing the data points with a value of 2.0 are set to a constant value of 1.0, the same value as the rest of the points in the original data set. This nulling operation allows the perturbations caused by the anomalous points to be examined, rather than allowing the anomalous point values to mask the ringing effect. The final interpolation results, minus the anomalous points, are shown in

Figs 67 and 68. Although not totally removed, the adverse "ringing" effects are clearly reduced when the K-Spline technique is applied.
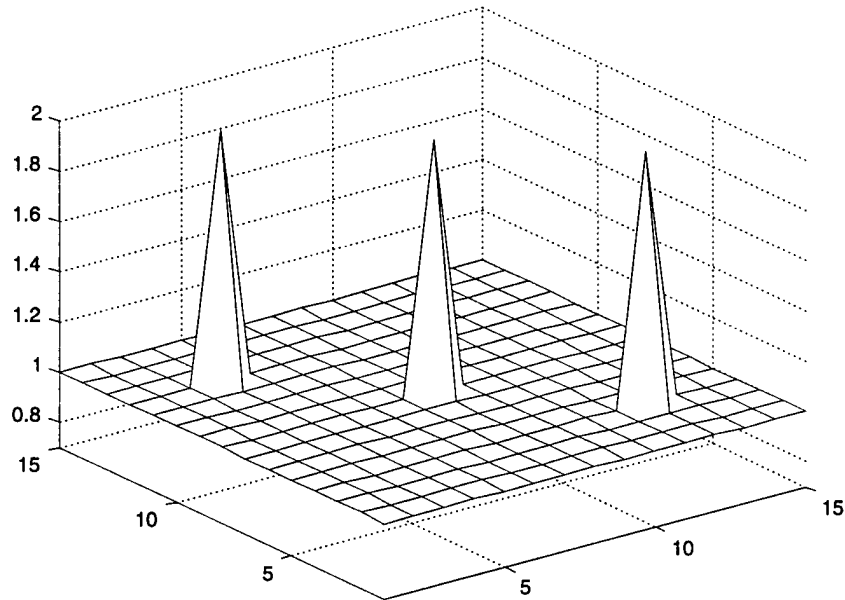
Figure 66: Anomalous Points on a Plane

Since data plotted in Figs 67 and 68 can be assumed to be errors, a metric describing the "amount" of error provides a meaningful comparison between the methods. Two possible metrics are the mean absolute error and the number of points with error. The center region of the Bi-Cubic Spline error of Fig 67 has a mean absolute error of approximately 0.0139 while the K-Spline mean absolute error of Fig 68 is approximately 0.0108 over the same central region. In addition, there are 3232 points with error in Fig 67 as compared to only 2208 points with error in Fig 68. In this context, error is defined as any value outside the range of 0.995 to 1.005 for both plots containing 5041 total data points.
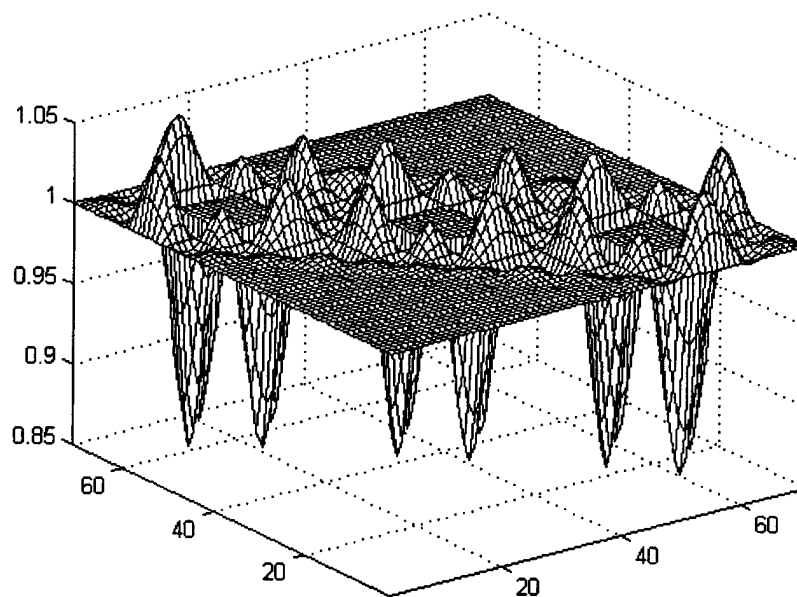
Figure 67: Perturbations in Bi-Cubic Spline Interpolated Data Set
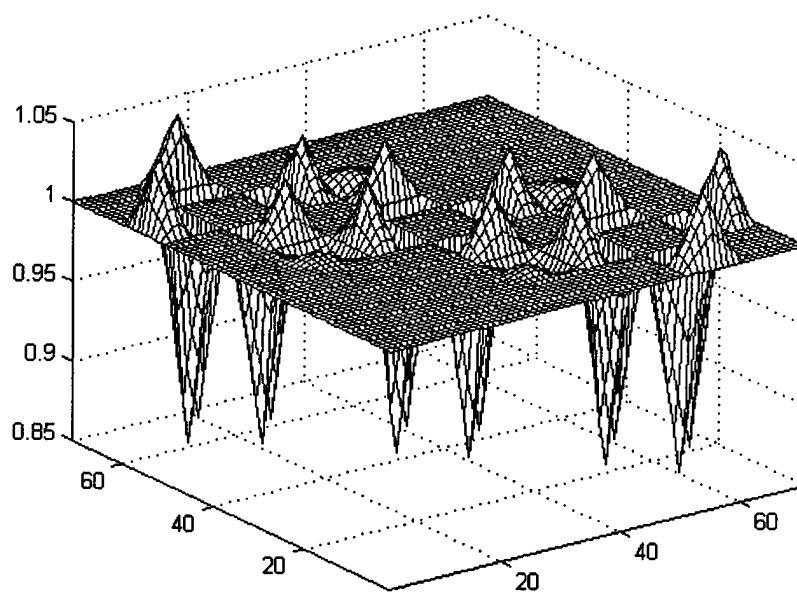
Figure 68: Perturbations in K-Spline Interpolated Data Set

96

The Bi-Cubic and K-Spline interpolation techniques are also compared using using original DTED data of a "close-up" shot of Niagra Falls as shown in Fig 69. The interpolation results for each technique are provided in Figs 70 and 71. For easier viewing of the data set, the East/West axis is flipped in Figs 69 through 71. The original data set clearly shows a flat region at the top and bottom of the falls, corresponding to a level water surface. The Bi-Cubic Spline method introduces severe oscillations within these regions with oscillations continuing on the lake prior to the falls. Although the K-Spline interpolated data set contains some unwanted oscillations, they are highly muted when compared with the Bi-Cubic data set within the same regions. Regions containing the most severe oscillation differences, including a shore line perturbation, are indicated by dark circles on Figs 70 and 71.
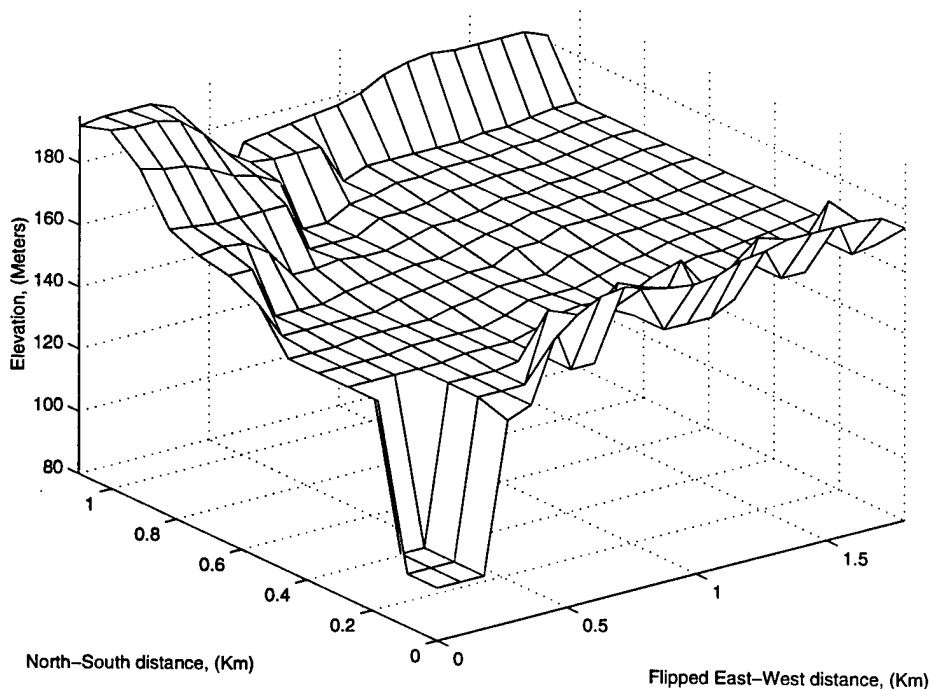
Figure 69: Close-up of Niagra Falls DTED, Flipped East-West Axis
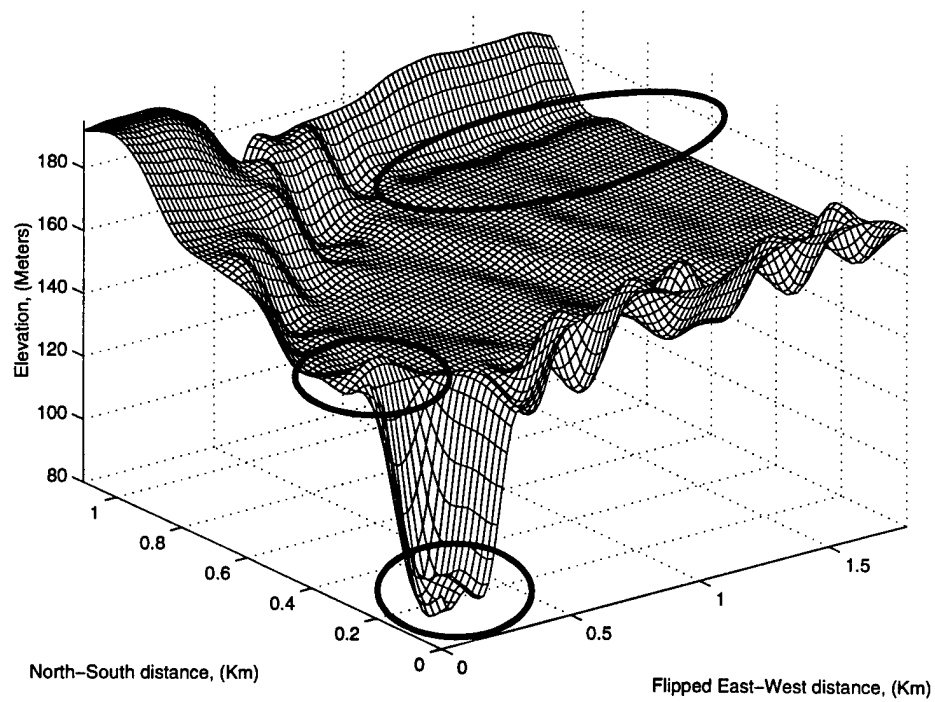
Figure 70: Bi-Cubic Spline Interpolation of DTED
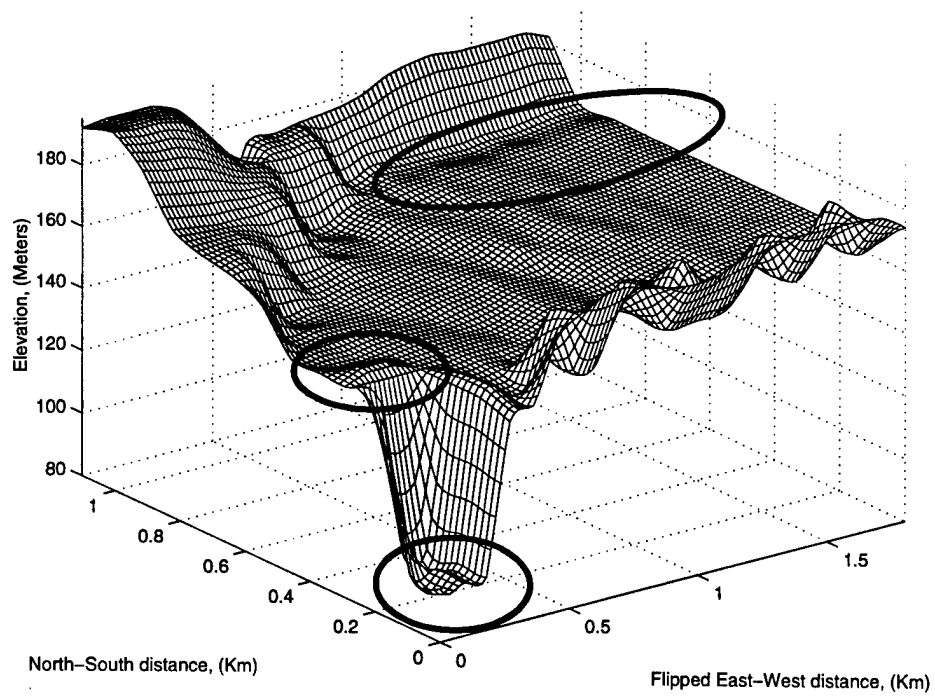
Figure 71: K-Spline Interpolation of DTED

98

5.7 Validation of K-Splines Using Measured Terrain Data

The performance of the K-Spline method in synthesizing Level 2 data from Level 1 is evaluated by the following procedure: A Level 2 DTED data set is selected as a truth model, thinned to Level 1 resolution, and the K-Spline method applied to interpolate data with Level 2 resolution. The interpolated Level 2 data set (excluding original common data points) is subtracted *point-by-point* from the original DTED to create a *synthesization error* data set. Although DTED contains *collection errors*, i.e. errors due to sampling, data processing, and integerization, this validation method for calculating and characterizing synthesization error represents a best possible measure of performance for the process.

At points in the synthesized Level 2 data set that coincide with Level 1 resolution data (one out of every nine points), there is no synthesis error and these points are not included in the error estimation. Elsewhere, errors appear to be normally (Gaussian) distributed with zero mean (average) and a standard deviation of less than one meter, as determined by application of the validation process to over 285 million DTED data points over fairly rugged terrain. This initial error analysis specifically excluded DTED regions containing ocean areas, as these regions are specified to have zero altitude, and synthesis of a perfectly flat region would artificially drive down the error values.

For relatively smooth ground, synthesis errors are negligible and only become worse as the terrain becomes more rugged with sharper ridge lines and peaks. The integer-only reporting of DTED affects the synthesis error analysis; access to real numbers with even just one decimal place accuracy could improve overall performance. Figures 72 through 75 show the results of the validation process using DTED over a region near Killeen, Texas.
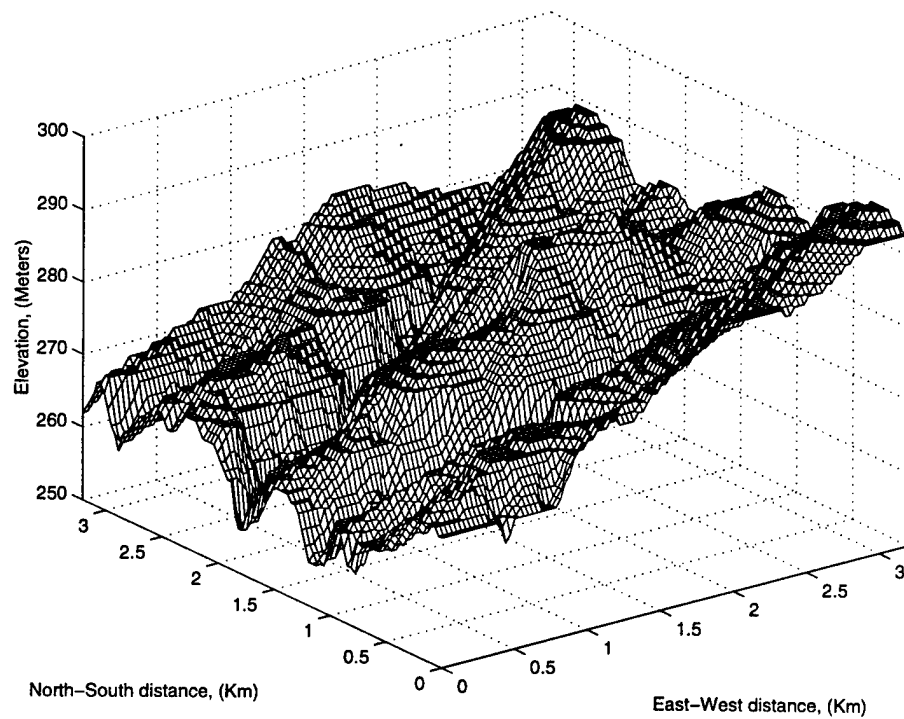
Figure 72: Original Level 2 DTED Map
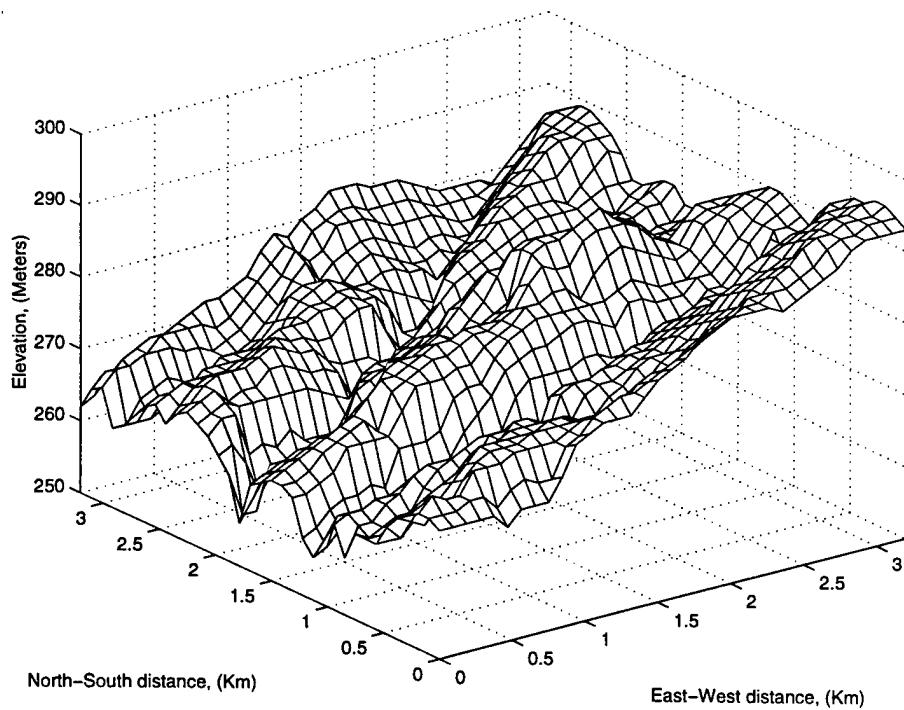
Figure 73: Original Level 1 DTED Map

100
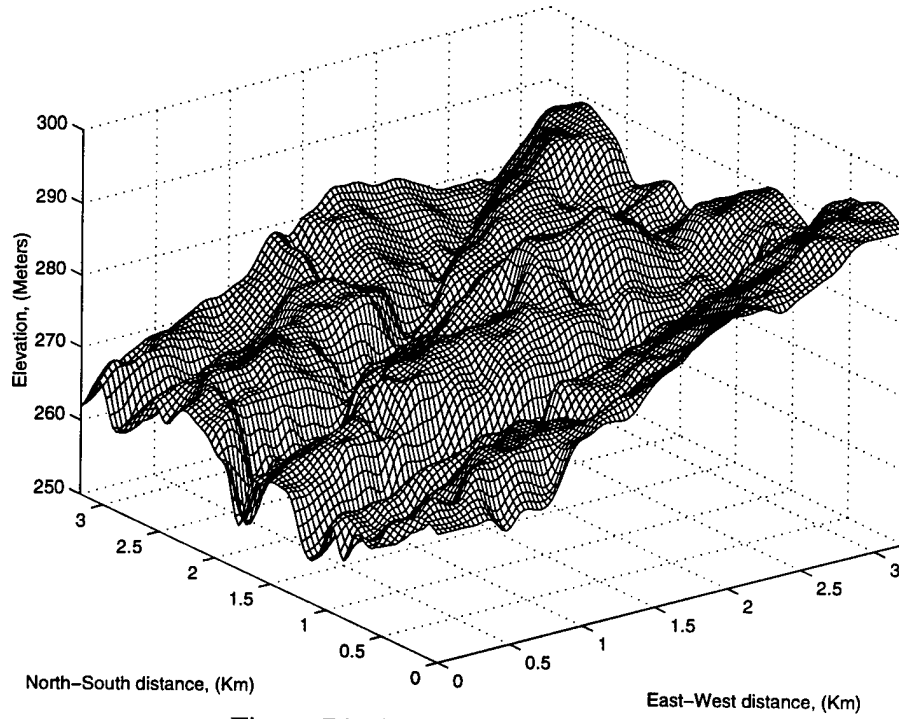
Figure 74: Synthesized Level 2 Map
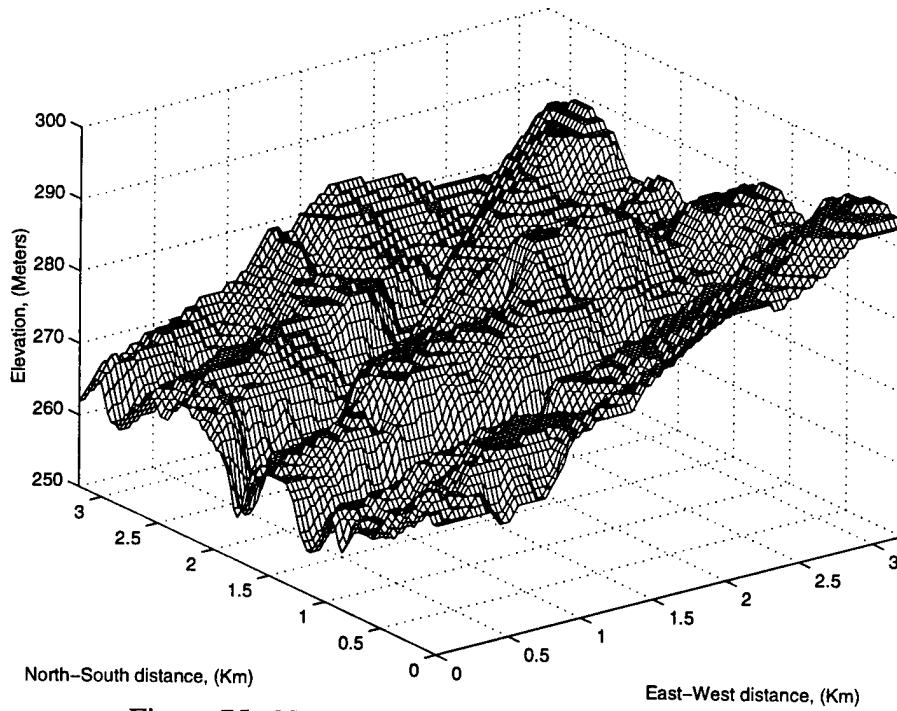
Figure 75: Nearest Integer Synthesized Level 2 Map

101

Figure 72 is a plot of the original Level 2 DTED data and Fig 73 is a plot of the same data set "thinned" to Level 1 resolution. Note that since DTED is reported/stored as integers, the figures contain miniature ridge lines. Figure 74 is a plot of the synthesized Level 2 data obtained with the K-Spline interpolation technique and the "thinned" Level 1 data of Fig 73. The data in Fig 74 represents a plot of "real numbers" obtained from the interpolation process. Finally, Fig 75 is a plot of the synthesized Level 2 data of Fig 74 where the data has been rounded to the "nearest integer" value for direct comparison with the original integerized DTED data of Fig 72. A direct comparison of the K-Spline data with the DTED data indicates a mean error of 0.0081 for the real number synthesized data and 0.0104 for the nearest integer synthesized data, virtually zero mean error for both cases. The error in both cases exhibits a Gaussian distribution with a standard deviation of about 0.5 meters for both real and integer data. This error profile suggests good confidence in the synthesized results.

6. Model Validation Against Beckmann

The Beckmann equation is an analytic derivation and allows validation of model results, under varying surface roughness conditions, against curves generated by a theoretical prediction. Although Beckmann's formulation requires simplifications not easily met by typical DTED based earth models, the flexibility of this digital model allows for implementation of necessary constraints such that Beckmann's conditions are easily duplicated.

6.1 Beckmann Equation

The conditions required for formulating an equation to calculate the normalized RCS of a patch of terrain are: 1) homogeneous media with constant Fresnel half-space reflection coefficients, 2) constant RMS height variation, σ_H, 3) constant lateral clutter height correlation distance, T, 4) an idealized antenna aperture with no sidelobes, 5) constant slope planar surface, and 6) limited number of Fresnel zones on the ground with an estimable taper-off contribution. The Beckmann equation was derived for bistatic scattering prediction.

Figure 76 shows the coordinate system used in Beckmann's formulation, and Fig 77 demonstrates the concept of Fresnel Zones. The Fresnel Zone issues are important, because Beckmann assumes an idealized field pattern radiating from the source antenna (identically reproduced by the observation antenna), and the Fresnel Zones provide a tapering off of the scattering contribution near the edge of the main beam's projection onto the ground. These zones are regions projected onto the ground that contain all points where the path length from the source to the observation point are within one-half wavelength, $\lambda/2$, of some reference.

103
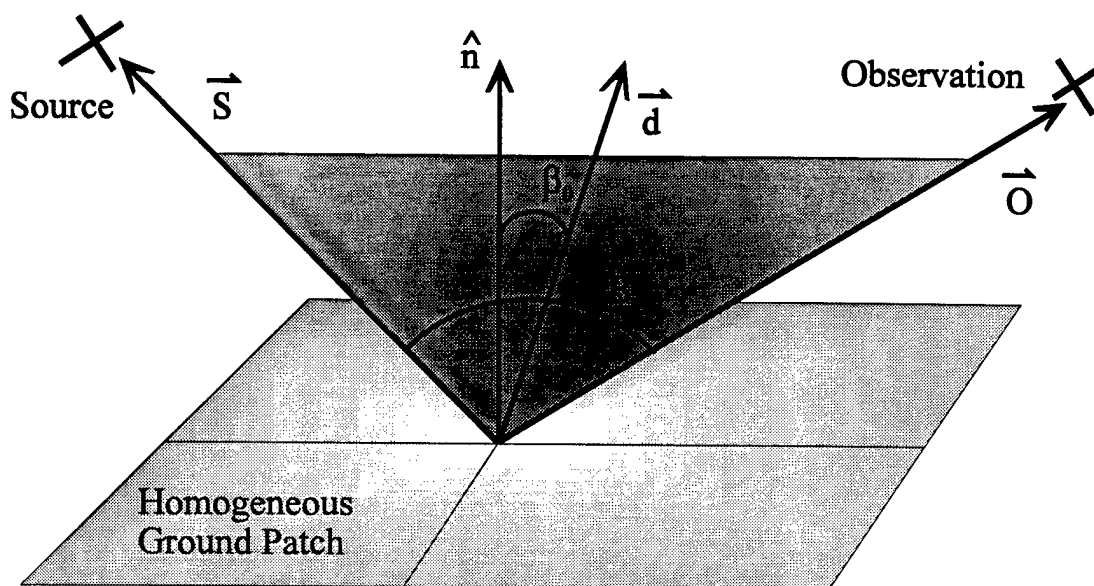
Figure 76: Coordinate System for Beckmann Equation
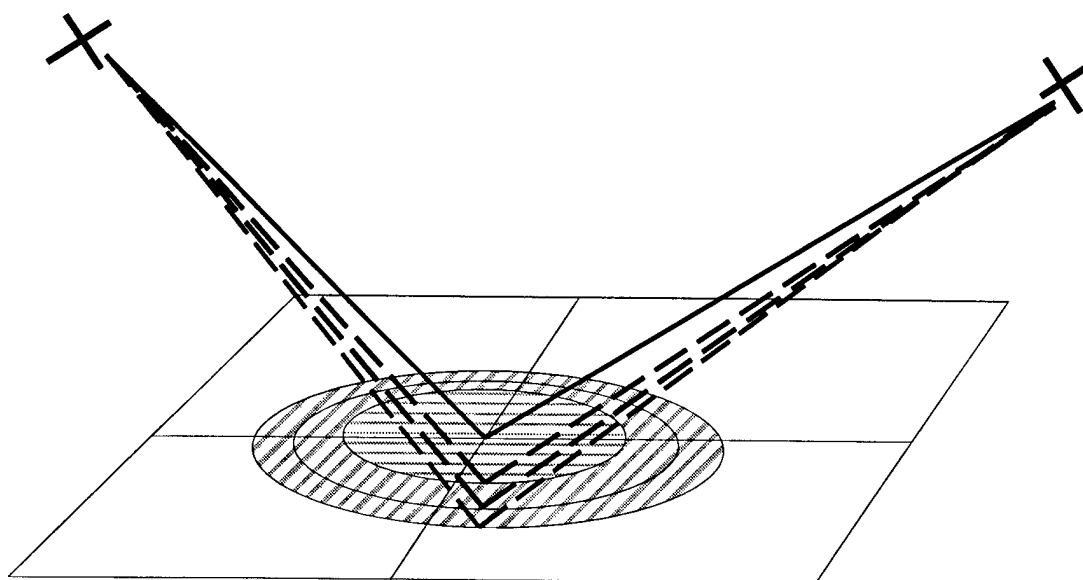
Figure 77: Fresnel Zones on Flat Surface

The solid line in Fig 77 represents the shortest ground reflection path from the source to an observation point. If this path length is L, the dashed lines represent reflection paths with length $L+\lambda/4$, $L+\lambda/2$, and $L+3\lambda/4$. Each circle on the surface is the locus of all points

with exactly the same path length, corresponding to a particular dashed line, and the two

cross-hatched regions represent the first two Fresnel Zones. Since reflection contributions

from successively higher Fresnel Zones, counting outward from the center, alternate in phase

and taper off in amplitude, Beckmann assumes the contribution of the sum of all Fresnel

zones after *"the first few"* [23] can be neglected.

Beckmann's formulation for calculating normalized RCS for a ground patch [24] is:

$$\sigma_B = \pi T^2 \left| \frac{1}{2\sqrt{\pi}} R^\pm \frac{\vec{d} \cdot \vec{d}}{d_z} \right|^2 e^{-g} \sum_{m=1}^{\infty} \frac{g^m}{m! \, m} e^{-\frac{d_{xy}^2 T^2}{4m}} \tag{45}$$

where:

T = lateral clutter height correlation distance in meters

$$\text{ex: } C(0) = 1 \, , \, C(\infty) = 0 \, , \, C(T) = e^{-1}$$

$R^\pm$ = vertical (+), horizontal (−) Fresnel half−space reflection coefficients

$g = \sigma_H^2 d_z^2$ = "projection of roughness" onto plane of incidence

$$\sigma_H^2 = \text{RMS height variation}$$

$$\vec{d} = \begin{bmatrix} d_x \\ d_y \\ d_z \end{bmatrix} = \vec{S} + \vec{O} = \text{bistatic bisector}$$

$\left| \vec{S} \right| = \left| \vec{O} \right| = \dfrac{2\pi}{\lambda}$ = normalized magnitude of source and observation vectors

$\left| \vec{d} \right| = \dfrac{4\pi}{\lambda} \cos\left(\dfrac{B}{2} \right)$ $\qquad\qquad$ $\vec{S}, \vec{O}, \vec{d}$ all lie in plane of incidence

$d_{xy} = \sqrt{d_x^2 + d_y^2} = \dfrac{4\pi}{\lambda} \cos\left(\dfrac{B}{2} \right) \sin\beta_0$

$d_z = \dfrac{4\pi}{\lambda} \cos\left(\dfrac{B}{2} \right) \cos\beta_0$ = vertical component of $\vec{d}$

β_0 = angle between $\hat{n}$ and plane containing both $\vec{S}$ and $\vec{O}$

Equation (45) is separable into two major components, as is shown in Eq (46), including: 1) a "terrain type" portion containing the $R^\pm$ reflection coefficients, and 2) a "roughness" portion containing T, σ_H (via g), and the summation terms. Any variation of permittivity or permeability of ground clutter constitutes a violation of the equation assumptions.

$$\sigma_B = \left[\left|\frac{1}{2\sqrt{\pi}}R^\pm\right|^2\right] \cdot \left[\pi T^2\left|\frac{\vec{d}\cdot\vec{d}}{d_z}\right|^2 e^{-g}\sum_{m=1}^{\infty}\frac{g^m}{m!\,m}e^{-\frac{d_{xy}^2 T^2}{4m}}\right] \qquad (46)$$

Since the "terrain type" portion contains only the familiar Fresnel half-space reflection coefficients and some constants, this portion provides no insight into scattering behavior as a function of clutter height variations.

The "roughness" is described by two parameters, the constant RMS height term, σ_H (see Eq (45)), and the lateral clutter height correlation distance, T. The correlation distance is the separation distance between any two points within a single ground patch such that the autocorrelation of the height is a constant value of e^{-1}. Given these constraints, the equation is not valid for describing scattering in regions with very rugged terrain.

Beckmann's assumptions are easily implemented within the digital model, including the constraint that the antennas have negligible sidelobe levels. The digital model's flexibility allows it to use both realistic DTED-based terrain values and generated terrain scenes satisfying the requirements of the Beckmann equation, as well as both realistic and idealized antenna radiation patterns.

When solving Beckmann's equation, care must be taken when computing the summation portion of the equation. The summation terms do not monotonically decrease and may actually approach zero for lower numbered terms. As such, the typical simple series convergence test of Eq (47):

$$\left| \sum_{m=1}^{N+1} S_m - \sum_{m=1}^{N} S_m \right| \leq \varepsilon \tag{47}$$

cannot be applied since the index number of the first significant term in the summation is unpredictable. This could force an early exit from the numerical summation routine and return an incorrect result. Two situations are illustrated graphically in Fig 78. In Series A the initial series terms start out as significant contributors to the summation, while for Series B the terms do not reach significant values until some later index.
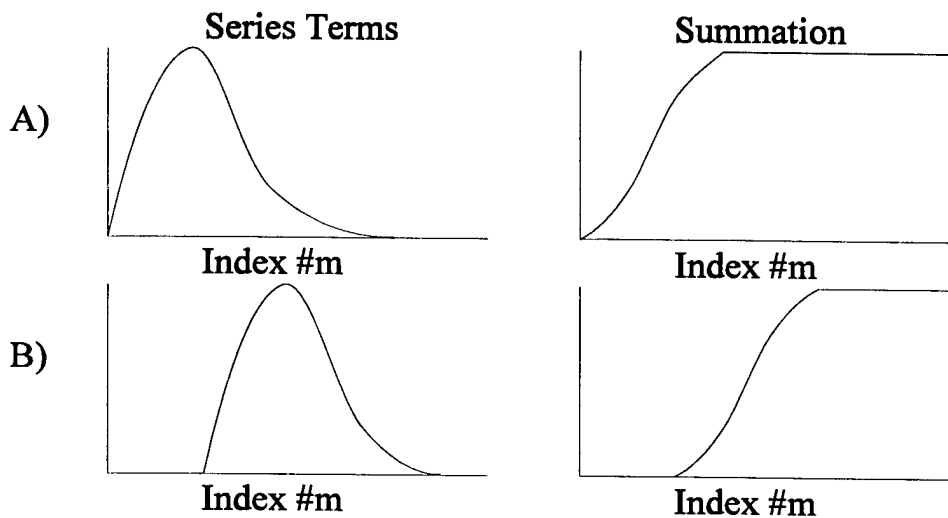
Figure 78: Beckmann Equation Summation Issue

107

The convergence test must not be initiated until after the series terms begin producing a meaningful accumulation in the summation. Since the series convergence was non-typical, the series was also tested for multiple regions of contributing terms after an initial satisfaction of convergence, i.e. high numbered series terms were examined for a resurgence in magnitude. This test was performed for multiple roughness indexes, up until calculation of the terms could no longer avoid numeric overflows, but no cases of multiple contributing regions were found.

6.2 Comparison of Results

For a comparison between digital model results and the Beckmann equation, the aperture field pattern in the model was set to an idealized main beam with a tapered edge and no sidelobes. Ground scenes were generated via computer, rather than read in from DTED files, to maintain constant roughness and to provide specific "amounts" of roughness. Since the comparison is really a comparison of the effective normalized backscatter from a patch of ground, the digital model was set up to keep radar propagation effects constant, i.i.e, the aperture gain, path length effects, and beam solid angle were held constant. For different surface roughnesses, the distance from the platform to a centered aiming point on the ground was fixed and the platform position was varied from a position nearly directly overhead, i.e., off by a fraction of a degree from true normal incidence, to a grazing angle near 90 degrees. This allowed the results from the digital model to be easily normalized, resulting in curves describing normalized backscatter coefficient versus angle of incidence for different roughness indexes.

The digital model is only capable of monostatic radar simulations. Therefore, the

bistatic bisector angle, B, in Beckmann's equation was set to 0.0 and the equation was solved

for the incidence angles varying from 0 to 90 degrees for different roughness indexes. A

matching case of surface roughness was run for both the digital model and the Beckmann

equation, producing results as shown in Fig 79. Two other curves are also shown in the

figure: Beckmann equation results for a surface "five times as rough" and digital model

results for a surface "ten times as rough" as the smoothest direct comparison surface.
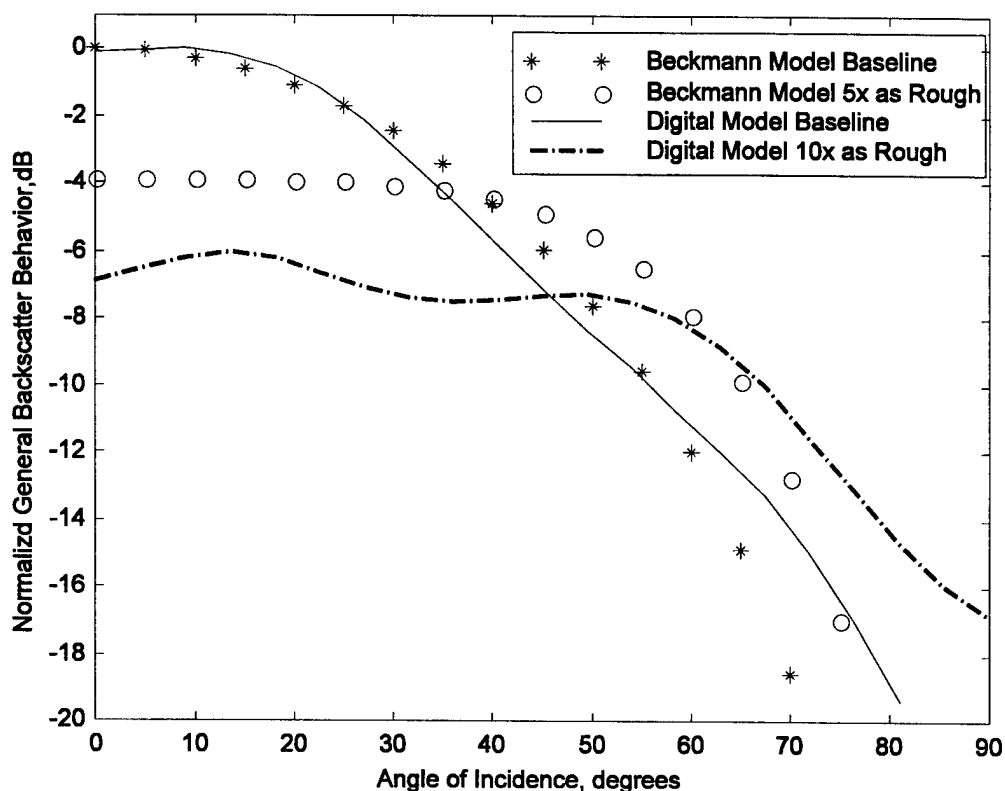
Figure 79: Validation of Digital Model Results with Beckmann Equation

Figure 79 shows how the scattering behavior follows a simple pattern for both

calculation methods. A smoother surface produces higher backscatter at angles near normal

109

incidence and falls off faster as a function of increasing angle of incidence. The rougher surface produces lower backscatter at angles near normal incidence and a wider angular region exists before backscatter levels begin to fall off.

The figure shows good agreement between digital model results and theoretical prediction, within about 1 dB of each other for the baseline surface roughness over angles from normal incidence up to 60 degrees. Beyond 60 degrees, the reduced slopes of a few individual pixels cause higher backscatter levels and the digital results diverge from the theoretical prediction. The digital model results do not approach $-\infty$ dB (a scalar value of 0) at grazing angles, as does the Beckmann equation, because the digital model uses ray tracing. Despite shadowing effects, some contributions from high pixels with non-zero slope will always remain.

7. Model Results

The ACE system "advantage" over a baseline APG-63 system is examined using various tracking scenarios. Model parameters such as platform roll, platform altitude (relative to both ground height and sea level), target depression angle, ground clutter height distribution, and clutter reflectivity, are varied to generate model results for each tracking scenario. Scenario output results are analyzed to determine parametric sensitivity and overall impact on ACE performance.

7.1 Returned Ground Clutter Power Comparison

Recalling from Chapter 2, the Signal-to-Clutter Ratio (SCR) may be expressed as:

$$SCR = \frac{E\left\{ \left| \sum_{m=1}^{M} \sigma_m G(\theta_m) \cos\left[k\frac{d}{2}\sin(\theta_m) \right] \right|^2 \right\}}{E\left\{ \left| \sum_{n=1}^{N} \sigma_n G(\theta_n) \cos\left[k\frac{d}{2}\sin(\theta_n) \right] \right|^2 \right\}} \qquad (48)$$

The ACE system "advantage" is defined as the improvement (increase) in SCR that an ACE configured system provides relative to the baseline APG-63 system, assuming both systems are operating in the same environment. Expressed in dB, the ACE system advantage is obtained per the following:

$$ACE\ Advantage = 20 \log_{10}\left\{ \frac{SCR_{ACE}}{SCR_{Baseline}} \right\} \ (dB) \qquad (49)$$

Since the numerator of Eq (48) is directly related to the percentage of active aperture and element weighting taper for a specific configuration, i.e., the nine ACE configurations and

111

the baseline system, the most statistically variant aspect of the equation rests in the ratio of clutter powers and not signal powers. For a specific ACE configuration, there exists a fixed relationship between ACE configuration signal power and baseline signal power. Given a target located in the aperture's maximum gain direction, the signal power relationships of Eq (51) are obtained using Eq (50) and aperture configuration information provided in Chapter 2. The positive decibel factors on the far right side of Eq (51) are ACE aperture usage penalties, so named because they result from less than optimum usage of available aperture surface area as compared to the baseline system.

$$SCR = \frac{E\{Signal\ Power\}}{E\{Clutter\ Power\}} \tag{50}$$

$$E\{Signal\ Power_{Baseline}\} = E\{Signal\ Power_{ACE-21}\} + 1.6\ dB$$

$$= E\{Signal\ Power_{ACE-20}\} + 2.1\ dB$$

$$= E\{Signal\ Power_{ACE-22}\} + 2.1\ dB$$

$$= E\{Signal\ Power_{ACE-19}\} + 2.8\ dB$$

$$= E\{Signal\ Power_{ACE-23}\} + 2.8\ dB \tag{51}$$

$$= E\{Signal\ Power_{ACE-18}\} + 3.4\ dB$$

$$= E\{Signal\ Power_{ACE-24}\} + 3.4\ dB$$

$$= E\{Signal\ Power_{ACE-17}\} + 4.1\ dB$$

$$= E\{Signal\ Power_{ACE-25}\} + 4.1\ dB$$

Given that signal powers are related by known factors, the main focus of ACE performance optimization becomes the amount of clutter power present. One way to increase the ACE advantage of Eq (49) is to reduce the denominator of Eq (50) for the ACE configuration, relative to the denominator of the baseline system, by an amount greater than the usage penalty indicated in Eq (51). The ACE aperture usage penalties are not as severe as they might initially seem. The baseline system using its tapered aperture weighting has a 5.6 dB boresight gain loss when compared to an equivalent uniformly illuminated system. However, as evident in Figs 80 through 82, sidelobe clutter power is reduced by more than 5.6 dB for all cases, thus providing a net increase in SCR for the baseline system over the uniformly illuminated system. The ACE usage penalties are overcome by similar trade-off effects, a reduction in the signal energy is offset if clutter energy is reduced by a higher margin. Note that the total percentage of aperture usage for the 20/22, 19/23, 18/25 and 17/25 ACE configuration pairs is identical, resulting in identical aperture usage penalties for these configuration pairings. The only difference between these configuration pairs is the distance between the phase centers. For the lower configuration number in each pairing, 17 through 20, the array active regions comprising the two phase centers are in contact with each other at the center of the aperture. For the higher configuration number in each pairing, the array active regions form a gap near the center of the aperture and extend to the edge of the aperture's surface area.

A plot comparing received clutter power for the baseline system, an ACE-21 configuration, and a uniformly weighted aperture is shown in Fig 80. All plotted data has been *normalized* by the mean clutter power value of the uniformly weighted aperture and

113
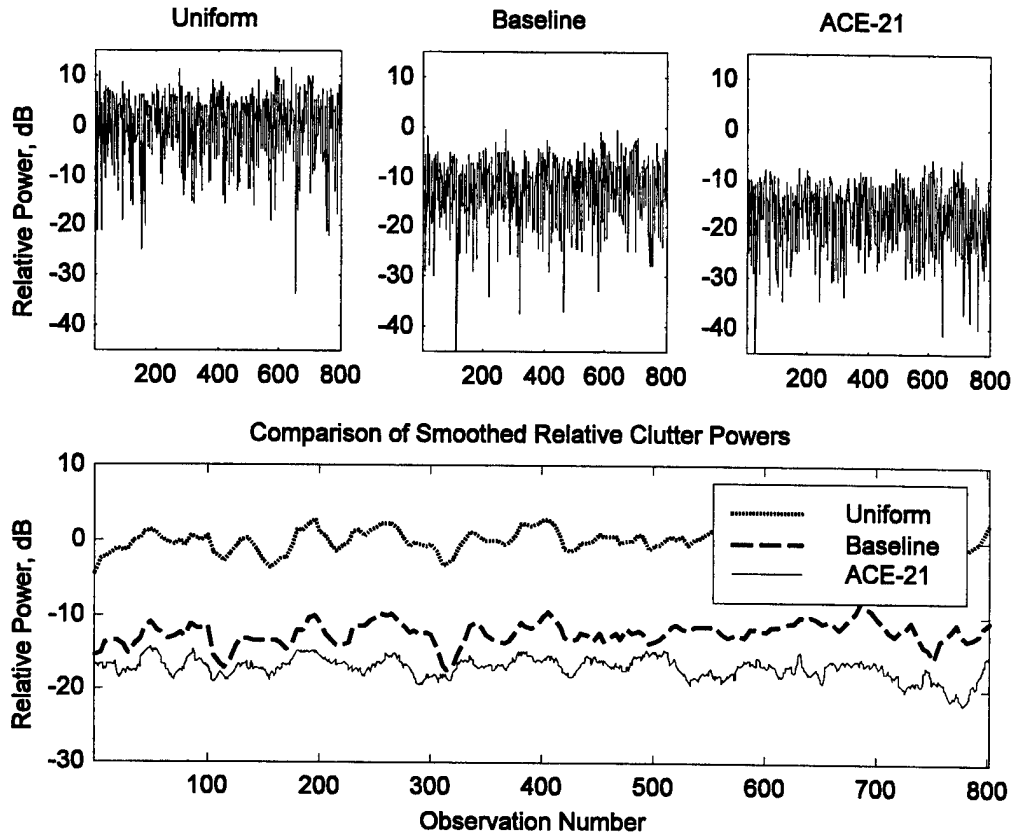
Figure 80: Clutter Power Comparisons for Different Systems in Straight and Level Flight

expressed as *relative power* in decibels. This power normalization process is used extensively for all clutter power data presented in this chapter. The observation index number is based on platform position changes of 100 meters. There are 800 observations in this figure, representing a simulated flight path of 80 km or approximately 49 miles. Throughout this chapter, the "ACE-21" notation specifically refers to an ACE system using only the 21 element separation configuration discussed in Chapter 2. It is *not necessarily the optimum configuration for the given scenario*. Plots formed using only the ACE-21 aperture are shown in Figs 80 through 82 where the variability introduced by allowing multiple ACE configurations could produce an incorrect interpretation of results. The plot in Fig 80 is for

114

straight and level platform flight, a mild target depression angle, and at a typical air-to-air engagement altitude. The top three plots in the figure show unsmoothed relative clutter power values for the three systems. The lower plot in the figure shows a "smoothed" version of the same results. A moving average window was used to smooth data to allow overlaying for easy comparison. As indicated, the dotted line is for a uniformly weighted aperture, the dashed line is for the baseline system, and the solid line is the ACE-21 configuration. Again, results have been normalized since absolute power levels are less important than relative improvement or degradation resulting from different system implementations.

Figure 80 highlights two interesting performance characteristics. First, it demonstrates a reduction in clutter power for the baseline system, with tapered aperture weighting, over a system with a uniformly weighted aperture. This is clear evidence of benefits gained by using a low-sidelobe aperture such as the APG-63's. The second characteristic emerges by comparing baseline system performance with ACE-21 results. The baseline system and ACE-21 configuration use the same basic element weighting profile. Even though the ACE-21 weighting is compressed and repeated twice vertically over the aperture, Fig 80 clearly indicates similar sidelobe clutter power improvements for the baseline and ACE-21 configurations, relative to the uniformly weighted case, with the ACE-21 configuration having the lowest indicated levels. For a specific ACE configuration, ACE-21 in this case, the returned clutter power for an ACE system may be either lower or higher than the baseline system, depending on the ground direction relative to the target location. ACE theory suggests that as the scenario progresses, the returned clutter power for the ACE-21 configuration may exceed that of the baseline system. At such times, it is likely

another ACE configuration exists whereby returned clutter power is lower than the baseline system. By using real-time intelligent selection of ACE configurations, within specific range cells during given scenarios, optimum ACE advantage may be obtained.

7.2 Performance as a Function of Platform Roll

Section 2.5 shows that for any amount of roll above a few degrees, an ACE system is unable to maintain coincidence between a generated null and given range cell over most of the azimuth range. As such, ACE experiences performance degradation with increasing platform roll. Roll degradation effects are illustrated in Fig 81 where the platform orientation is manipulated to maintain a constant 9.4 degree null depression angle on fairly mild and flat terrain. Since their radiation patterns are nearly symmetric about boresight, the uniformly weighted and baseline system show little dependence between clutter power and roll. This is not the case for the ACE-21 configuration. All ACE configurations have higher lateral sidelobe levels than the baseline system. As platform roll increases, the ACE null and range cell overlap region decreases and the higher sidelobes produce increased clutter power levels.

This effect can be reduced with a fully adaptive aperture which compensates for roll in the element weighting profiles. However, roll compensation on apertures with discretely located elements requires another dimension of aperture configurability, applicable at discrete roll angle intervals. Additionally, the ground clutter reflection changes as a result of a different polarization, requiring an improved backscatter model for proper analysis. Finally, the failure of the ACE model in scenarios *where is should fail*, as predicted in Chapter 2, adds credibility to the digital model.

116
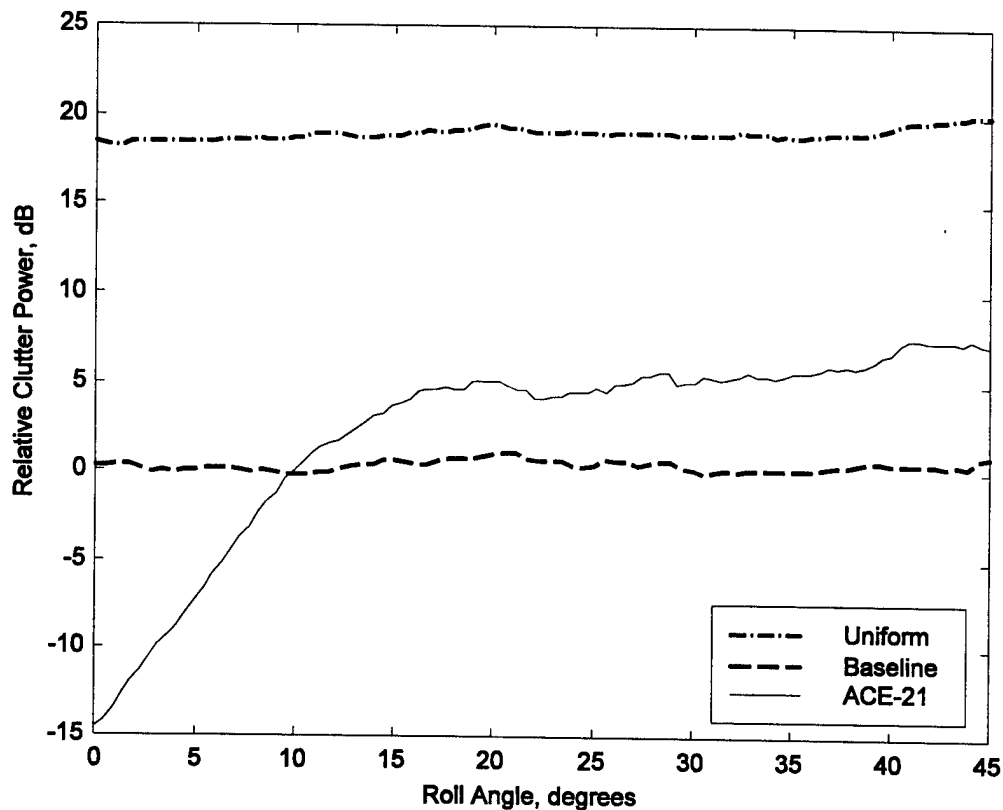
Figure 81: Clutter Power versus Platform Roll

7.3 Performance as a Function of Platform Altitude

As shown in Fig 82, returned clutter power is highly dependent on ACE platform altitude, varying in excess of 40 dB over the indicated range of altitude. The top three plots in the figure represent unsmoothed clutter power, normalized by the maximum value of the uniform system. The lower plot is an overlay of the same data that has been smoothed for ease of comparison. Data for this figure was generated using a constant target depression angle of 8.3 degrees relative to the ACE platform. Throughout the scenario, the target position remains close enough to the range gated region such that a specular clutter flash is

117

avoided over the entire range of altitudes. The platform and target "flew" a simulated course, simultaneously increasing their altitudes while maintaining a constant depression angle. As expected, returned clutter power is higher at lower altitudes and decreases with increasing altitude.
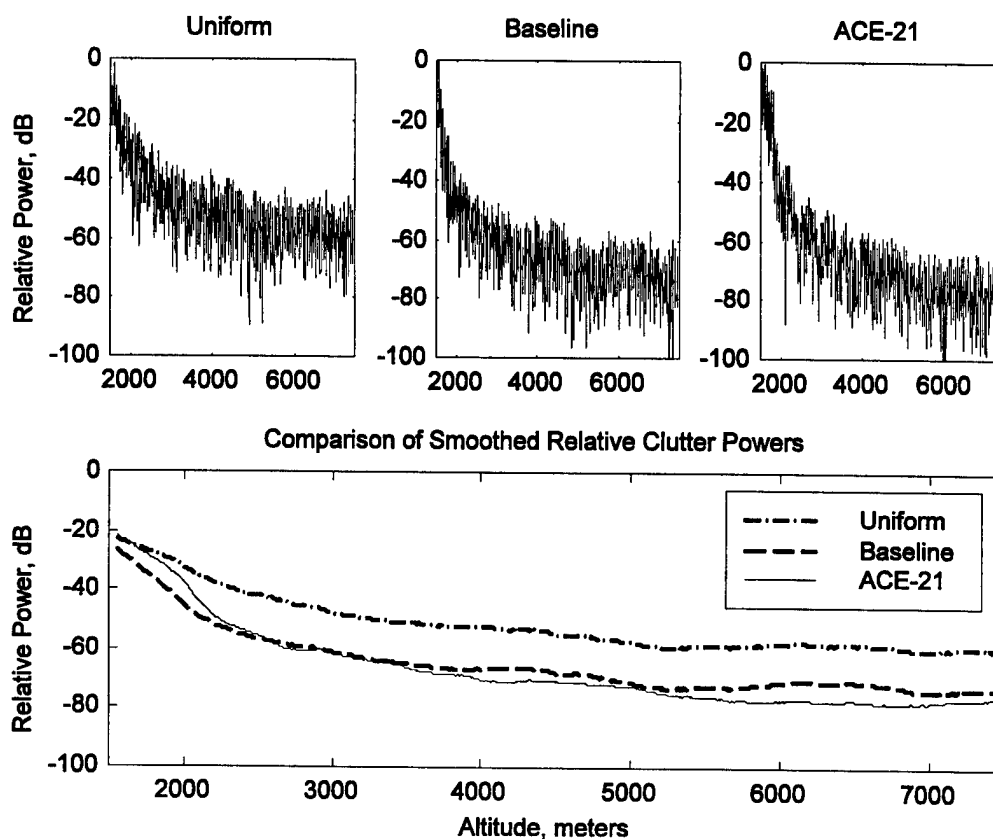
Figure 82: Clutter Power versus Altitude

The ACE advantage is plotted in Fig 83 as a function of platform altitude for two different scenarios. One scenario is for a target a with a 1.5 degree depression angle over relatively smooth terrain and the other is for a target with a 5.1 degree depression angle over considerably rougher terrain. The solid center line represents the smoothed ACE advantage and the upper/lower dotted lines show the extent of a 1.0 standard deviation range in the

118

moving average window. Although not apparent in these plots, the standard deviation is not entirely constant over the data sets. For both scenarios, the data is generated by allowing the ACE system to select the optimum element configuration to achieve maximum advantage. Since the ACE advantage is defined by a ratio of SCR values and the baseline system experiences the same clutter power roll-off rate as each of the nine ACE configurations, the ACE advantage performance is expected to be relatively independent of platform altitude. This is evident in the ACE advantage plots of Fig 83 where the advantage holds at about 10 dB for both scenarios using a relatively shallow, constant target depression angle while the platform maintains a straight flight path.
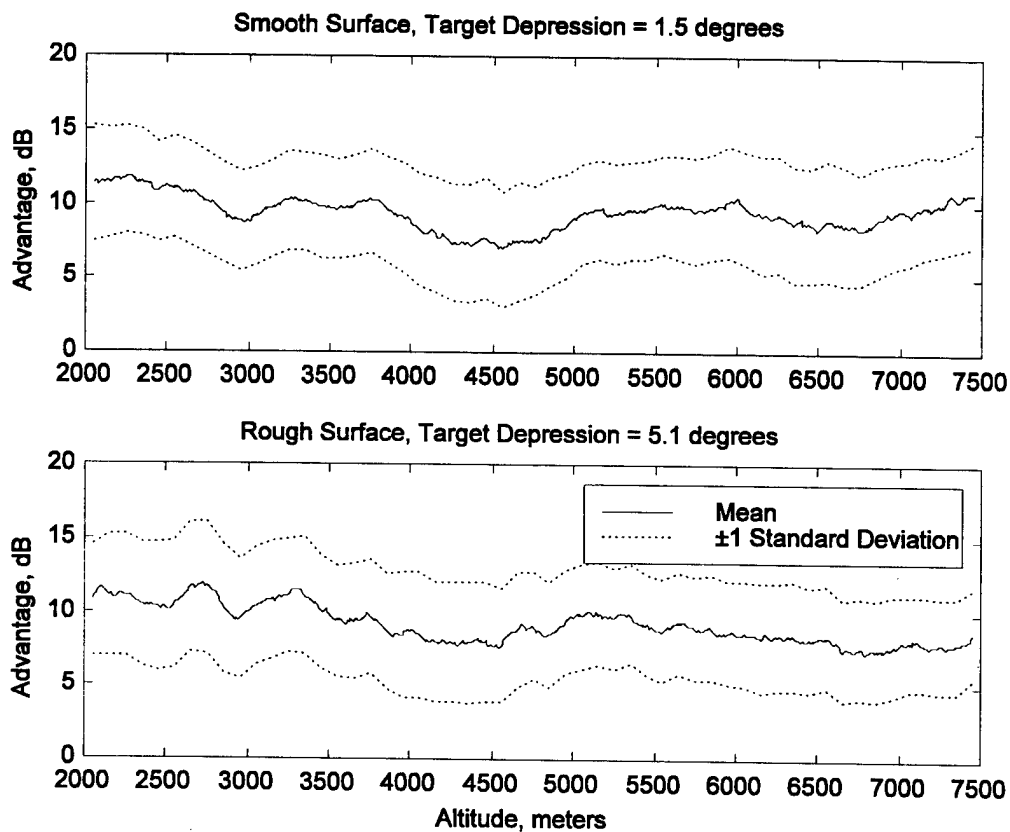
Figure 83: ACE System Advantage versus Altitude

7.4 Performance as a Function of Range Gate Length

Range gate length is another parameter which affects overall clutter power without significantly affecting the ACE advantage. Figure 84 shows returned clutter power variation for the ACE-21 configuration using three different range gates. All data was generated using shallow target depressions angles above terrain with medium roughness characteristics over a simulated flight distance of approximately 49 miles, yielding the 800 observations indicated in the figure. As in previous figures, the top three plots represent unsmoothed power measurement data, normalized by the mean clutter power received by the 750 meter range gate system. The lower plot shows smoothed normalized data used for performance
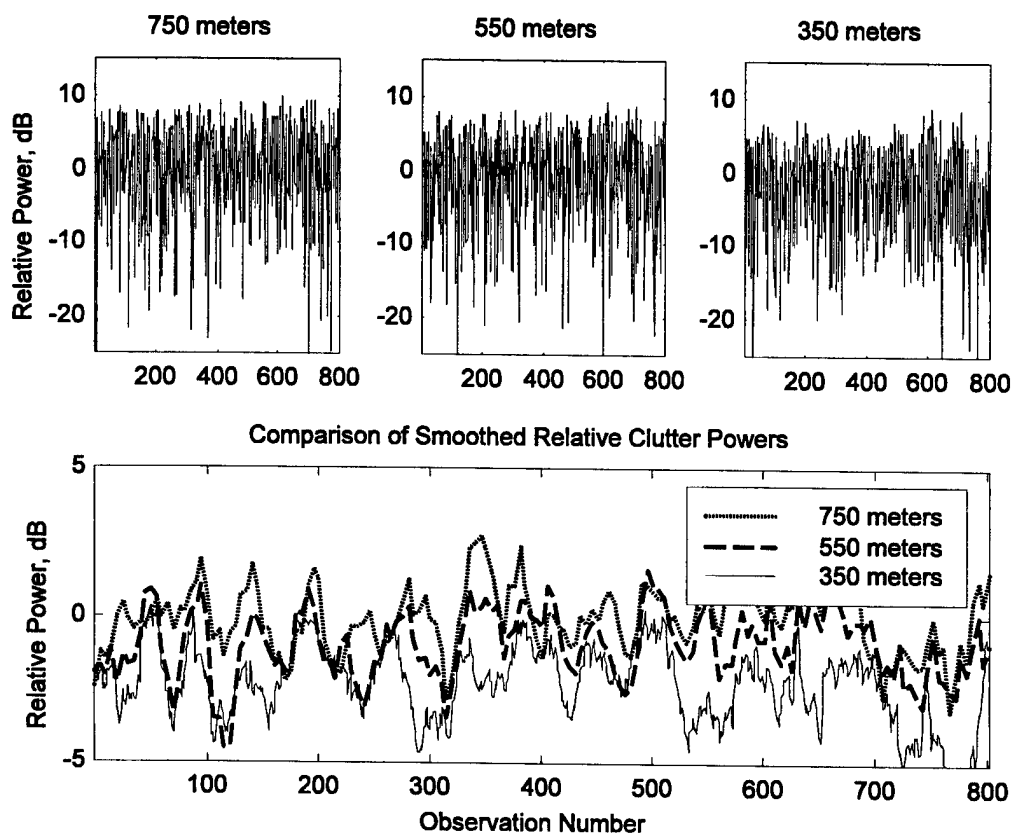
Figure 84: Clutter Power versus Range Gate Length

120

comparison. As indicated in Fig 84, longer range gates generally contribute more received clutter power. This behavior is expected since more terrain reflections are included in a single observation for longer range gates.

The ACE advantage is plotted in Fig 85 as a function of observation number for each range gate under consideration. Data in Fig 85 represents the ACE advantage when the relative positions between the platform, target, and ground are maintained such that the ACE-21 configuration is always chosen as the optimum configuration. However, other tests indicate that when flight scenario parameters, i.e., platform altitude/range and target altitude/range, are varied and the ACE system is allowed to select an alternate more optimum
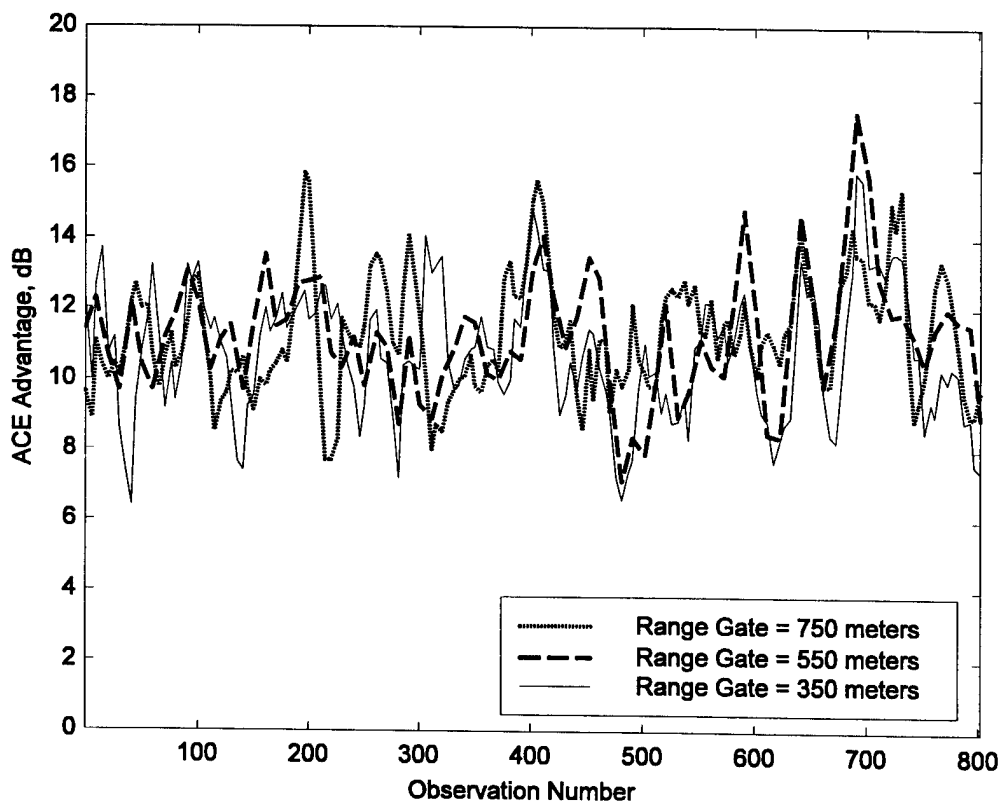
Figure 85: ACE System Advantage versus Range Gate Length

121

configuration, the results are consistent -- returned clutter power increases with longer range gates but overall ACE advantage remains fairly independent of range gate length.

One reason the ACE advantage is fairly independent of range gate lengths between 350 and 750 meters is that *projected path length differences* between points located in near and far regions of the range cell do not differ significantly and ACE system sidelobes on either side of a null exhibit odd phase symmetry. Figure 86 is a graphical representation of projected path length difference for points in near and far regions of three differently sized range cells. All points located in the angular region above the cell center, as viewed from the ACE platform, are farther from the platform than all points in the angular region below the cell center, again as viewed from the platform. For typical scenarios, the differences in projected path length for points above and below the cell center differ slightly, typically increasing with increased range gate width. Given an ACE null is placed on the ground at the center of a projected range gate, the near portion of the cell is "viewed" through elevation sidelobes located directly below the null while the far portion of the cell is "viewed" through elevation sidelobes located directly above the null. Since the ACE sidelobes located immediately on either side of a given null possess odd phase symmetry, i.e., have opposite phase characteristics, ground echos from points within the near and far regions of a cell which do not vary significantly effectively cancel each other. Longer range gates simply possess more pairs of "similar" echos which cancel each other upon arrival.
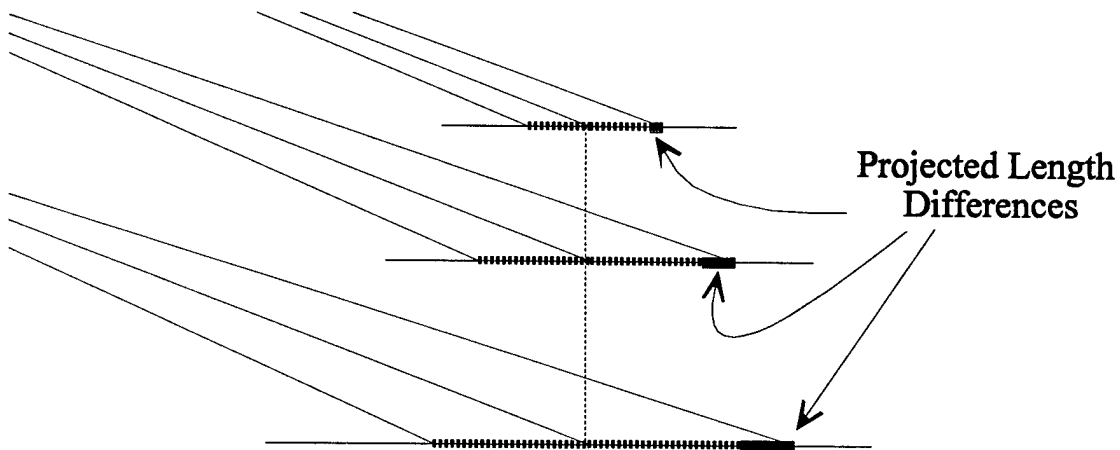
Figure 86: Near and Far Illuminated Zone Depth Difference

The 350, 550, and 750 meter range gates used in this analysis were chosen to be consistent with operational air-to-air radars. At typical fighter aircraft engagement altitudes and ranges, these three range gates result in a projected angular region of about one degree or less. As such, the ACE advantage differences illustrated in figure 85 for the range gate scenarios are not significant. For systems using ultra-wide range gates, it is expected that this situation would likely be different since larger angular projections will allow greater path length differences. Ultra-narrow range gated systems, e.g., ones employing pulse compression techniques, would likely not experience any real improvement by implementing the ACE technique exclusively, but would also require the use of angular resolution enhancement techniques such as DBS or SAR to gain significant advantage. The performance of such a system cannot be characterized by current ACE formulations and is perhaps best suited for analysis under ICE theory, a technique which remains to be fully explored and exploited.

7.5 Performance as a Function of Clutter Type

Ground clutter type is another parameter investigated to determine its impact on ACE advantage. Figures 87 and 88 show returned clutter power results for two different terrain types, trees and road surfaces, using the range gates described in Section 7.4.

Trees

Road Surfaces
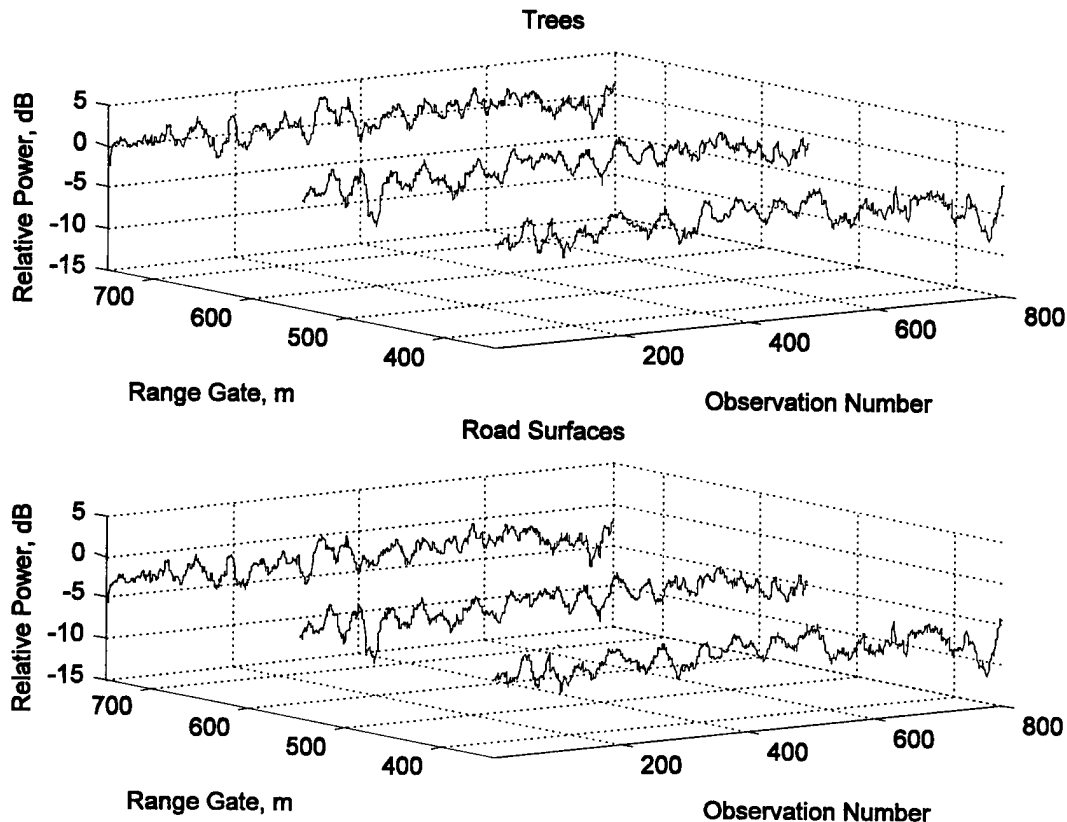
Figure 87: Clutter Power Comparisons for Different Terrain Types and Range Gates

In generating these data sets, the flexibility of the digital model came to be more fully appreciated. For all scenarios, the platform and target "flew" exactly the same profile and the height distribution of the terrain was identical. The only difference is that half of the data runs are for terrain "covered" with road surface material and half are for terrain "covered" by trees. For each terrain type and flight profile, identical range cell pixels were either

124
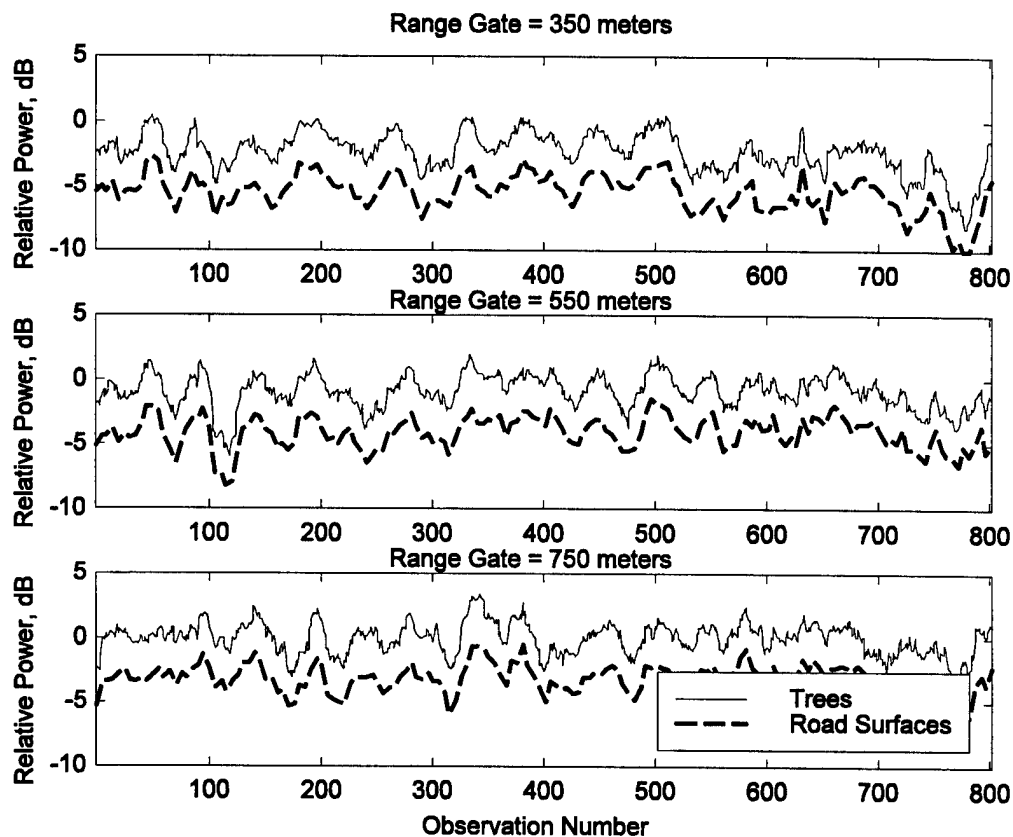
Figure 88: Clutter Power Comparisons for Different Terrain Types

illuminated or shadowed during corresponding observations for a given range gate. The Nth pixel backscatter interrogation event, i.e. a subroutine call to the backscatter coefficient generator, in both terrain classification data runs were sent identical incidence angles and "random" backscatter values, only the terrain type was different. As a result, the overlay of curves in Figs 87 and 88 do not include any effects due to "randomness" of the backscatter coefficient generator. Independently, the curves include random effects of the backscatter coefficient generator; collectively, there is nothing random between curves for a given observation number.

There is one final observation to make from Fig 88. For a given observation number, the difference between the relative power curves is fairly constant for the two terrain types. For these simulations, the angle of incidence with the ground ranged between 10 and 20 degrees within a given range cell. At such angles, the mean backscatter coefficients for trees and road surfaces differs between 2.6 and 5.0 dB [14], approximately the difference between the curves in the figures.

Figure 89 shows how the ACE advantage is virtually unaffected by terrain type for the range gates considered. Since the ACE advantage is a function of clutter power rejection capability, relative to the baseline system, the absolute value of returned clutter power is insignificant in determining performance. The baseline system's returned clutter power rises and falls as a function of terrain reflectivity, just as the ACE system's does. This is an entirely separate issue and does not effect ACE's ability to accurately place a null on the ground at the center of a range cell. A significant difference in performance can only arise if one of the terrain types, such as tall trees, contributes to the surface roughness factor such that the angular region viewed by the ACE system increases, thereby, increasing the number of clutter returns. For terrain type analysis in this section, surface roughness parameters were intentionally set equal for each terrain type considered, specifically isolating type effects from roughness effects. The backscatter coefficient magnitude then becomes the key player in determining overall ACE system performance. Surface roughness effects on ACE performance are addressed separately.
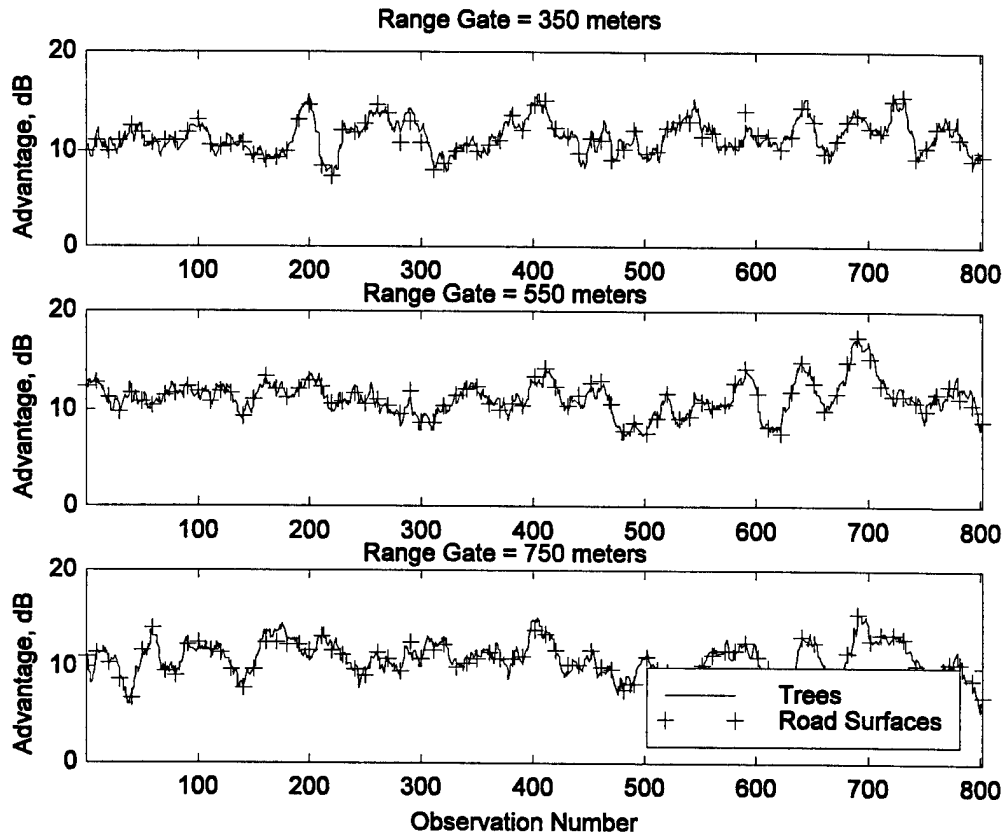
Figure 89: ACE System Advantage Comparisons for Different Terrain Types

7.6 Performance as a Function of Target Depression Angle

Whenever the angular difference between a target's location and the center of a range cell is between 10 and 85 degrees, the platform is level, and no specular ground flash exists, the ACE system provides an advantage over the baseline system. However, there is a performance limitation on target depression angle that results from ACE implementation. The nulls generated by ACE which are closer to mechanical boresight are not as deep as nulls located farther away. Also, the sidelobes located near boresight have higher gain than those more removed. Revisiting Figs 22 through 32, it is seen that nulls start at about three to four

degrees from boresight and, depending on the specific ACE configuration, repeat over slowly

increasing intervals. Although the interferometer equation predicts nulls at lower angles, the

"early" nulls, i.e., the ones closer to boresight, are not fully exploitable for an ACE system.

Figure 90 shows relative clutter power levels for the baseline and ACE systems where

each is tracking a target with increasing depression angle. For both systems, increasing target

depression angle increases clutter power levels. For the optimum ACE configuration, this

occurs because 1) the null placed on the ground is not as deep or wide as required, and

2) clutter returns are entering sidelobes near the boresight region, i.e., sidelobes physically

located closer to the aperture's boresight, a region where sidelobe levels are generally higher.
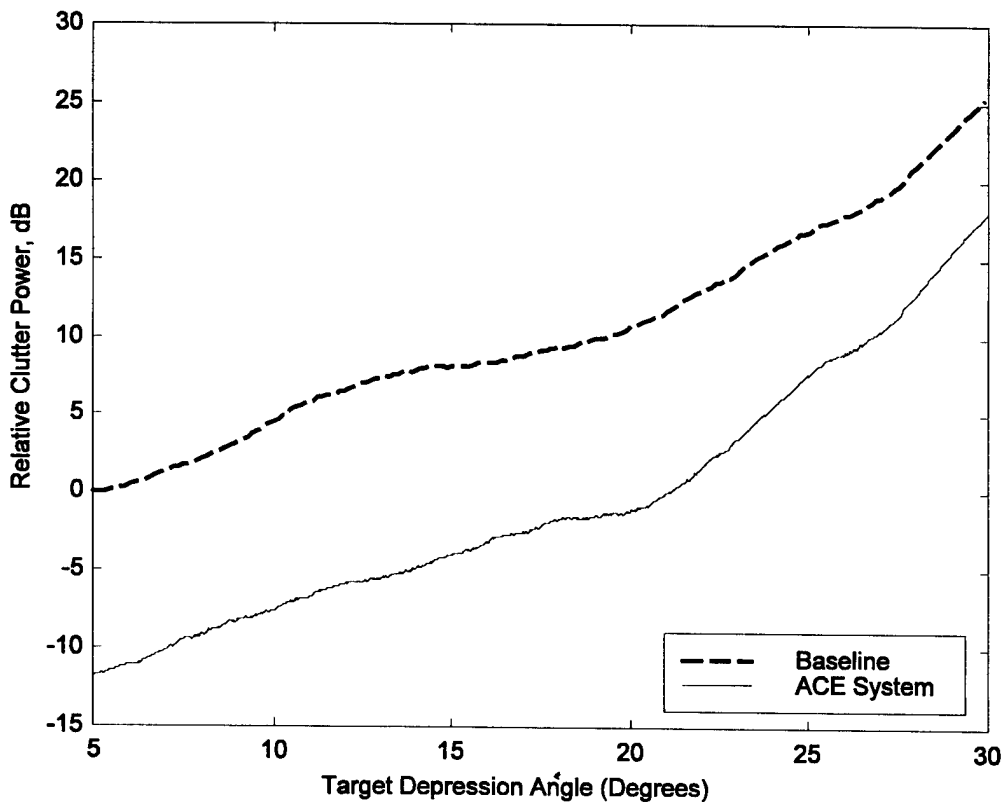
Figure 90: Clutter Power versus Target Depression Angle

Examination of Fig 90 reveals that the two curves appear to converge for increasing depression angle. This phenomena results from the ACE system having higher near boresight sidelobe levels than the baseline system, resulting in clutter power rising more rapidly with increasing depression angle. The effect of this behavior on ACE system advantage is highlighted in Fig 91 for both smooth and rough surface structures. As target depression angle increases, the ACE optimization process progressively selects an aperture configuration whereby the main null used for clutter suppression becomes closer and closer to boresight. As a result, returned clutter power increases according to Fig 90, producing the ACE advantage characteristics shown in Fig 91. These plots demonstrate a decreasing capability of near boresight nulls to improve ACE advantage.

Figure 91: ACE System Advantage versus Target Depression Angle

129

7.7 Performance as a Function of Clutter Height Distribution

Figure 91 represents data for two surface structures with different roughness indices. For this case, the RI_2 roughness index of the rough surface is about 15 meters in both North/South and East/West directions, i.e., the standard deviation of clutter height at one pixel subtr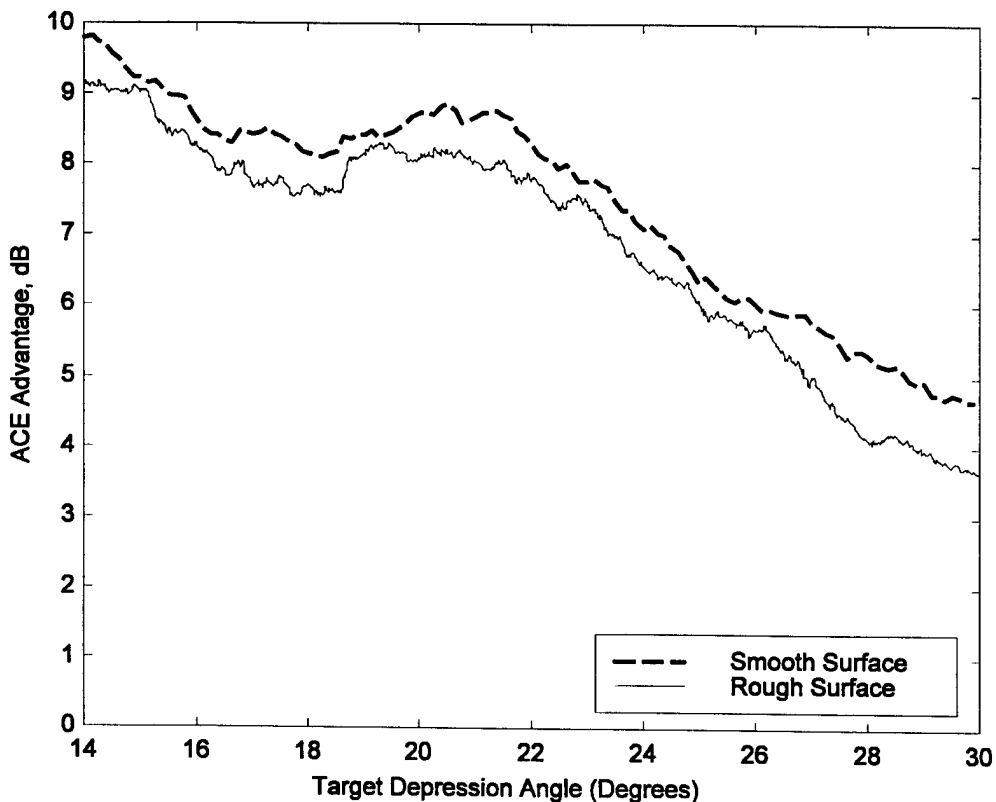acted from the height of an adjacent pixel is 15 meters. A standard deviation of 15 meters was chosen to represent "rough" terrain, because it approximates the median value of RI_2 for DTED qualitatively defined as "rough" during development and testing of the interpolation routine. The smooth surface roughness index is approximately 0.3 meters.

Although a difference exists between the two curves in Fig 91, ACE performance is not overwhelmingly affected, even for this case where one surface is approximately *50 times rougher* than the other. Negligible performance change occurs because the angular variation in clutter height distribution within a given range cell, as viewed from the platform, is relatively small compared to the total angular region occupied by clutter.

7.8 Detection Improvement and Limitation Issues

From the cases examined, it appears that although ACE provides a fairly stable 10 dB SCR improvement over the baseline system for a wide variety of tracking scenarios, it may not provide enough clutter rejection to eliminate the need for Doppler detection in all cases. To achieve the clutter rejection required for detection of targets without Doppler and at higher depression angles, smaller resolution cells may be required. Figure 92 shows absolute SCR for a target with a non-fluctuating Radar Cross Section (RCS) of 0 dB, a constant range of 6.7 miles, and an ACE platform altitude of 20,000 feet. For longer range targets, or lower

ACE platform altitudes, the curves are expected to drop rapidly. ACE can preserve an SCR above 0 dB for a few more degrees of depression angle, but the return signal strength eventually drops below the clutter return for a target at a lower altitude.
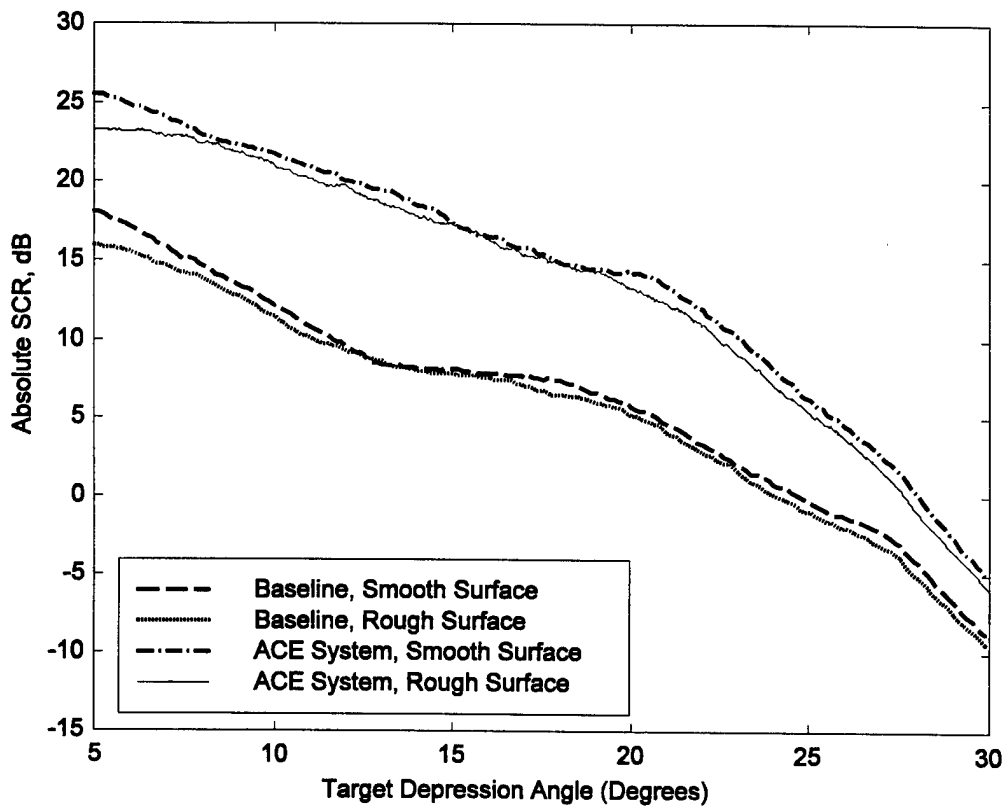
Figure 92: Absolute SCR versus Target Depression Angle

Target RCS is another issue affecting SCR. As target RCS varies significantly above or below 0 dB, the SCR curves shift up and down in a corresponding fashion. A histogram of RCS values for a typical fighter sized aircraft with non-stealthy features, i.e., open engine inlets and no radar absorbing material, is shown in Fig 93 [25]. The data set contains 60,000 values taken near the model frequency of 10 GHz and was collected over equal angular intervals in azimuth from nose to tail in elevation from 20 degree below the waterline th 20

131

degrees above. This represents typical observation angles for an aircraft in flight. The median RCS for this aircraft is about 2.5 dB which produces an absolute SCR value of at least 2.5 dB above the 0 dB test target for 50% of the observations. Since target RCS affects returned signal power for both baseline and ACE configurations, RCS variations are expected to have minimal impact on ACE advantage.
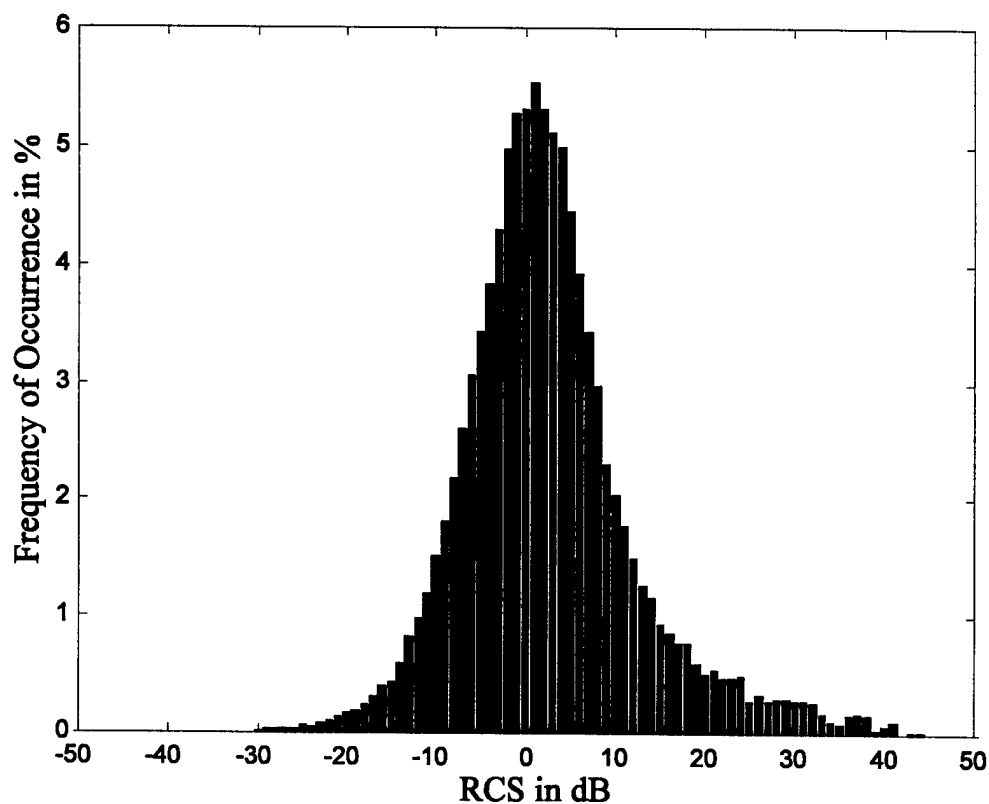
Figure 93: Histogram of RCS Values for Sample Aircraft

For Doppler aided detection of targets, a radar system may need to operate under range ambiguous conditions. This situation provides ground returns at multiple depression angles rather than the single ground path examined thus far. For this case, the ACE system could attempt to null out the "loudest" ground return, possibly, but not necessarily, the one

132

closest in range. Nothing in the proposed ACE technique prevents incorporation of either Doppler detection or range ambiguous PRF modes. Although the ACE advantage is expected to decrease, nulling out clutter power from the one "loudest" ground return will still provide an improvement in SCR.

8. Conclusions and Recommendations

8.1 Conclusions

The results of this research effort clearly demonstrate the viability of the Adaptive Clutter Erasure (ACE) system concept as a next generation clutter suppression technique, offering radar performance enhancement commensurate with currently implemented techniques. As developed, analyzed, and simulated under this effort, the basic ACE concept provides a solid basis for further research and analysis of real-time software/hardware clutter suppression techniques whose goal is to minimize unwanted clutter returns in airborne radar systems.

The ACE concept represents a novel technique whereby adaptive real-beam interferometric processing techniques are employed to enhance radar clutter suppression. Research and simulation results indicate the ACE concept, as implemented herein, provides a reliably consistent 10 dB Signal-to-Clutter Ratio (SCR) advantage, i.e., increased clutter suppression capability as compared to the baseline system, for nearly all simulated scenarios. Performance degradations for scenarios where the ACE system provided minimal or no advantage, i.e., scenarios including platform roll or large target depression angles, are "*as expected*" in the sense that simulation results are consistent with theoretically established principles. For other scenario parameters, results indicate clutter power reduction is fairly immune to changes when the ACE technique is applied to a real beam radar system.

For validation and simulation of the ACE concept, a new multi-layer 3-D clutter modeling technique was developed by incorporating existing clutter reflectivity statistics and

134

measured terrain elevation data. By comparison with traditional 2-D clutter modeling techniques, the six-layer 3-D model offers tremendous flexibility by accurately characterizing the relative altitude, slope, type, surface thickness, probabilistic reflectivity, and shadowing of terrain on a *pixel-by-pixel* basis. This new 3-D clutter characterization technique is more robust and accurate than traditional 2-D clutter modeling techniques which are typically based on constant terrain characteristic assumptions within gated range cell regions. Because of the flexibility, robustness, and accuracy provided by the new 3-D clutter modeling technique, this research represents the first work to examine and reliably estimate the effects of finite ground clutter *thickness* on interferometric-based radar discriminants. The 3-D clutter modeling technique has been transitioned to the Model Based Vision Laboratory of the Air Force Research Laboratory (AFRL) for application to development programs with goals of providing improved terrain data estimation and enhanced radar calibration techniques.

In direct support of the aforementioned 3-D clutter modeling technique, a unique interpolation scheme was developed to interpolate poorly behaved under-sampled 3-D data, such as is commonly observed in measured terrain elevation data. The interpolation scheme is based on a modified cubic spline formulation and, as indicated by results in Chapter 5, the interpolation technique/algorithm is reliable and performs exceptionally well. For nearly all terrain conditions, the technique accurately creates closely spaced interpolated results from sparse input data, i.e., closely spaced interpolated values compare extremely well with measured data taken at the same interval spacing. The interpolation scheme has been adopted by both the National Imagery and Mapping Agency (NIMA) and the Model Based

135

Vision Lab of the AFRL as a standard terrain interpolation technique for high resolution ground scene modeling. The interpolation technique has also been successfully applied in image reconstruction filter design for processing images corrupted by noise.

Although the ACE system concept differs significantly from the Interferometric Clutter Erasure (ICE) concept, i.e., ACE is applicable to real-beam radar systems and ICE is based on Synthetic Aperture Radar (SAR) processing, the principle theory behind the two concepts is very similar, namely, clutter suppression via interferometric cancellation. ACE research results suggest the ICE system concept can perform as envisioned and provide a basis for comparing the two concepts. These results provide a modest estimate of the potential clutter suppression capability that the two concepts can achieve. It is anticipated the ICE concept will benefit from using sharper, more restrictive range resolution cells while dealing with the possibility that targets transgress resolution cell boundaries.

8.2 Recommendations for Future Work

Future research efforts should concentrate on three areas, improved backscatter coefficient generation, improvement or additional applications of the terrain interpolator, and examination of topics to bridge the gap between ACE and ICE concepts. Backscatter reflectivity modeling can be expanded to include: 1) other polarization cases, 2) additional frequency bands, and 3) more terrain types.

For this research effort, backscatter coefficient generation was limited to Vertical-Vertical (VV) polarization cases at X-band frequencies for nine different terrain types (plus a 10th composite). These initial limitations were imposed to be consistent with the baseline

APG-63 system being modeled, a VV polarized X-band radar. The nine terrain types provided an acceptable range of backscatter coefficient variation for examining and characterizing ACE performance as a function of terrain type. The limitation to nine terrain types resulted from initial data availability. As developed, the backscatter generator has potential application beyond this effort. During transition of the initial backscatter model to AFRL, the applicability of the method to other radar system modeling efforts, including fully polarimetric and multi-band radars, became quite evident. Further enhancement of the backscatter model to include additional terrain types will provide additional flexibility for clutter scene modeling and radar calibration over virtually any type of terrain.

Combined with proper target cross-sectional and polarization response data, an improved backscatter generator could assist in digital modeling and testing of radars employing polarimetric techniques to detect targets in clutter. The probabilistic nature of this new generator could more accurately model scattering from real terrain, providing a wider range of returns from a single terrain type. Testing with this improved generator would tax detection algorithms at much higher levels than currently achieved with simplistic backscatter models that return a single, deterministic number as a function terrain type and incidence angle of incidence.

The K-Spline interpolation algorithm, initially developed to convert measured elevation data from equal arc second spacing to uniformly spaced data, has been adapted for synthesizing high resolution data sets from lower resolution data sets and has been successfully applied to enhance image filtering. Because the interpolation technique balances predictive behavior with a data filtering effect, it is applicable for interpolation of

137

many 2-D data sets where conventional methods fail due to the poor behavior of the data. As with all data "filtering" techniques, the algorithm requires optimization for specific applications in terms of adapting filter characteristics for different levels of required damping and smoothing. Presently, the K-Spline interpolation technique works well for interpolating mildly rugged terrain and accurately synthesizes high resolution terrain data over geographical regions where only lower resolution data exists. Measurement of terrain altitude at high resolutions typically requires expensive, dedicated equipment. Therefore, a reliable interpolation technique such as the K-Splines provides the opportunity to significantly reduce measurement costs, i.e., make fewer measurements at lower resolution and use interpolation to fill in the data set.

Analysis and implementation issues associated with merging existing target detection enhancement techniques, i.e., Doppler detection, Doppler Beam Sharpening (DBS), and Synthetic Aperture Radar (SAR) processing, with ACE and ICE concepts need to be explored. This new work would serve as a stepping stone into a deeper investigation and understanding of the ICE concept itself and provide valuable insight into the potential transitionability of each interferometric concept (ACE and ICE) into existing radar systems.

References

1. Skolnik, Merril I., *Radar Handbook*, McGraw Hill, 1990.

2. McDonald, Adam, US Air Force F-15C pilot and radar operations instructor, Personal interview, 2 Aug 1996.

3. O'Brien, J. et al., "Interferometric Radar Imaging Using the AN/APG-76 Radar", *SPIE AeroSense Symposium*, Apr 1996.

4. Li, Fuk K. and R. M. Goldstein, "Studies of Multibaseline Spaceborne Interferometric Synthetic Aperture Radars", *IEEE Transactions on Geoscience and Remote Sensing*, vol 28. No. 1, Jan 1990.

5. Holt, Hugh, APG-76 Systems Manager, Research Development and Advanced Systems Department, Northrop Grumman Norden Systems, Electronic Mail, 18 Sep 1996.

6. U.S. Patent application, "Interferometric Clutter Erase", Owner: Environmental Research Institute of Michigan.

7. Ibsen, Paul M., "Acquisition and Dissemination of Interferometric Synthetic Aperture Radar (SAR) Data for Tactical Use", *Proceedings of the Eleventh Night Operations Symposium*, February 1994.

8. Ward, J. *Space-Time Adaptive Processing for Airborne Radar*, Contract F19628-95-C-0002, Lexington, Massachusetts: Lincoln Laboratory, Massachusetts Institute of Technology, Dec 1994 (AD-A293032).

9. Hale, Todd B., *Secondary Data Support and Non-Homogeneities in Space-Time Adaptive Processing*, MS thesis, AFIT/GE/ENG/97D-06, School of Engineering, Air Force Institute of Technology (AU), Wright-Patterson AFB OH, Dec 97.

10. Temple, Michael A., *Radome Depolarization Effects On Monopulse Receiver Tracking Performance*, Ph.D. dissertation, AFIT/DS/ENG/93-03, Air Force Institute of Technology (AU), Wright-Patterson AFB OH, Jun 1993.

11. Raemer, Harold R., *Radar Systems Principles*, CRC Press, 1997.

12. Beckmann, Petr and Andre Spizzichino, *The Scattering of Electromagnetic Waves from Rough Surfaces*, Artech House, 1963.

13. Ulaby, Fawwaz T. and M. Craig Dobson, *Handbook of Radar Scattering Statistics for Terrain*, Artech House, 1989, p. 26.

14. Ulaby, Fawwaz T. and M. Craig Dobson, *Handbook of Radar Scattering Statistics for Terrain*, Artech House, 1989.

15. Defense Mapping Agency, *Digitizing the Future*, 1994

16. Ulaby, p. 136, 266, 304, 26.

17. Devore, Jay L., *Probability and Statistics for Engineers*, Fourth Edition, Duxbury Press, 1995.

18. Press, William H. et al., *Numerical Recipes in C*, Cambridge University Press, 1988.

19. Hermes, Doug J. *Optimized Design Methodology of Cavity Backed Microstrip Antennas with Dielectric Overlay*, MS thesis, AFIT/GE/ENG/97D-04, School of Engineering, Air Force Institute of Technology (AU), Wright-Patterson AFB OH, Dec 1997.

20. Isaacson, Eugene and Herbert Keller, *Analysis of Numeric Methods*, Wiley, 1966.

21. Chambless, Susan, Eric Schwarz, and Bernard J. Kolo, "Automated Static Radar Prediction", *Proceedings, Defense Mapping Agency Systems Center Symposium '89*, May 1989.

22. Magnus, Amy, *The Inquisitive Nature of Data Fusion in the Human Visual System*, Ph.D. prospectus, Air Force Institute of Technology (AU), Wright-Patterson AFB OH, Mar 1998.

23. Beckmann, p.11.

24. Jocoy, E. et al., *Results and Analysis of the Bistatic Terrain Measurements Program*, Vol I (of 2), Contract F33615-84-C-1517, Calspan Corp, CRN 7277-2, EW File s/3/7159, Feb 1991.

25. Unclassified data set provided courtesy of AFRL/SNA at Wright-Patterson AFB in Ohio for a fighter sized aircraft.

REPORT DOCUMENTATION PAGE

1. AGENCY USE ONLY (Leave blank)	2. REPORT DATE	3. REPORT TYPE AND DATES COVERED
	June 1998	Dissertation

4. TITLE AND SUBTITLE

EFFECTS OF CLUTTER HEIGHT DISTRIBUTION ON ADAPTIVE CLUTTER ERASURE PERFORMANCE

5. FUNDING NUMBERS

6. AUTHOR(S)

Kelce S. Wilson, Captain, USAF

7. PERFORMING ORGANIZATION NAME(S) AND ADDRESS(ES)

Air Force Institute of Technology,
WPAFB OH 45433-7765

8. PERFORMING ORGANIZATION REPORT NUMBER

AFIT/DS/ENG/98-05

9. SPONSORING/MONITORING AGENCY NAME(S) AND ADDRESS(ES)

AFRL/SNAS
Attn: Patti Ryan (937) 255-6329 x2617
2010 Fifth Street, Bldg 23
WPAFB OH 45433-7001

10. SPONSORING/MONITORING AGENCY REPORT NUMBER

11. SUPPLEMENTARY NOTES

12a. DISTRIBUTION/AVAILABILITY STATEMENT

Approved for public release; distribution unlimited

12b. DISTRIBUTION CODE

13. ABSTRACT (Maximum 200 words)

An interferometric processing technique, Adaptive Clutter Erasure (ACE), is investigated for applicability to ground clutter suppression in airborne radar systems. By analysis and simulation, the concept is demonstrated to achieve performance enhancements comparable to currently implemented techniques. Results indicate that ACE provides a reliably consistent 10 dB Signal-to-Clutter Ratio (SCR) advantage over the APG-63, an operational radar system used for baseline comparison. ACE system concept development and performance predictions are conducted in conformity with the physical and operational design parameters of the APG-63. In support of this effort, a novel multi-layer 3-D clutter model is developed by incorporating existing clutter reflectivity statistics and measured terrain elevation data. This new clutter model offers tremendous flexibility by accurately characterizing the relative altitude, slope, type, surface thickness, probabilistic reflectivity, and shadowing of terrain on a *pixel-by-pixel* basis. This is in sharp contrast to traditional 2-D clutter modeling techniques which typically include deterministic backscatter characteristics and assume constant terrain characteristics. External to ACE concept validation, this approach provides the opportunity to improve terrain classification methodology and enhance radar calibration techniques. A probabilistic backscatter coefficient generator is introduced which produces realistic backscatter values for various terrain types at all incidence angles over the full range of variability associated with real terrain.

14. SUBJECT TERMS

Radar, Clutter Suppression, Interferometric, Interferometry, Radar Backscatter, Ground Clutter

15. NUMBER OF PAGES

154

16. PRICE CODE

17. SECURITY CLASSIFICATION OF REPORT	18. SECURITY CLASSIFICATION OF THIS PAGE	19. SECURITY CLASSIFICATION OF ABSTRACT	20. LIMITATION OF ABSTRACT
Unclassified	Unclassified	Unclassified	UL